Analysis and Design of Class-E Switching Circuits for Inductively Coupled Wireless Power Transfer Systems

January 2015

Tomoharu Nagashima

Graduate School of Advanced Integration Science
CHIBA UNIVERSITY

(千葉大学審査学位論文)

Analysis and Design of Class-E Switching Circuits for Inductively Coupled Wireless Power Transfer Systems

January 2015

Tomoharu Nagashima

Graduate School of Advanced Integration Science
CHIBA UNIVERSITY

Contents

Figure Contents

Table Contents

Acknowledgment

I would first like to thank my research supervisor Associate Professor Hiroo Sekiya, for his guidance and encouragement throughout my study and research. I have benefited from his vast wealth of knowledge and his constructive comments during my research.

I owe a great deal of thanks to the members of my thesis committee, Professor Shingo Kuroiwa, Professor Yoshitsugu Manabe, Associate Professor Masato Kitakami, Associate Professor Hiroo Sekiya from Chiba University, Japan, and Professor Tadashi Suetsugu from Fukuoka University, Japan for their many helpful comments and suggestions.

I would like to appreciate to Professor Marian K. Kazimierczuk from Wright State University, USA, Dr. Xiuqin Wei from Fukuoka University, Japan, Associate Professor Takuji Kousaka from Oita University, Japan, Associate Professor Hisa-Aki Tanaka from the University of Electro-Communications, Japan, and Associate Professor Eduard Alarcón from UPC BarcelonaTech, Spain, for their support and encouragement. I am grateful to Professor Yoshifumi Nishio and Assistant Professor Yoko Uwate from Tokushima University, Japan, for their support and encouragement.

I also gratefully appreciate the financial support of Japan Society for the Promotion of Science (JSPS) that made it possible to complete my thesis.

I also would like to thank the members and staff who encouraged and helped me to complete my research at Sekiya-Komuro Laboratory.

Special thanks to my family, especially to my parents, for their constant encouragement, endless love and support.

Graduate School of Advanced Integration Science

Chiba University

Tomoharu Nagashima

Chapter 1

General Introduction

1.1 General Background

Recently, wireless power transfer (WPT) systems have attracted considerable attention. In systems having WPT system, electrical energy is transformed from a power source to a load without the connection of electrical cables. It can be stated that the concept of WPT system is not a new idea. The first person to introduce the concept of the WPT was Nikola Tesla. Tesla demonstrated the illumination of lamps without electrical connections by using a high frequency electrostatic field in 1893 [1]. The next major achievement was demonstrated by William Brown. His demonstration was that a small helicopter can fly 60 feet away by microwave beam [2]. The interest in WPT research field increased after his accomplishments. The breakthrough in WPT research field occurred in 2007 by an MIT research team. In their experiments, a 60 W light bulb was illuminated wirelessly from a power source 2 meter distance with an incredible high efficiency of 40 % based on strongly coupled magnetic resonance [3]. Of course, the recent growth in WPT field has also been contributed by low-loss and small-size electric components associated with information-communication technology innovations. For promoting more practical uses of WPT systems, it is necessary to enhance the overall efficiency of WPT systems.

WPT can be achieved by magnetic field coupling, electromagnetic field coupling, or microwave coupling [4]. WPT via magnetic induction is referred to as “inductively coupled WPT”. The inductively coupled WPT system has gained a lot momentum recently. This is because this system is suitable for near or middle-distance applications, such as wireless charging for electric vehicles, mobile devices, medical implants, and so on. Additionally, several standards for inductively coupled WPT systems, for example, “Qi” [5] and “Rezence” [6], have been developed for a better integration of various charging devices. The inductively coupled WPT system is basically composed of three parts, which are dc-ac inverter, inductive coupled coils, and ac-dc converter [4]. The dc-ac inverter and the ac-dc converter are referred to as “transmitter” and “receiver”, respectively. For transmitting electrical energy wirelessly, it is needed to generate a high frequency alternating current and feed it in the coupled coil at the transmitter side. In addition, the conversion of the alternating current to a dc voltage in the receiver side is also required for dc-load applications. Therefore, a dc-ac inverter for generating a high frequency alternating current and an ac-dc converter for converting the ac current to a dc current are necessary parts in WPT systems.

In practical inductively coupled WPT systems, high overall efficiency and compact system scale are strongly required. The system size is reduced and the transfer distance can be extended as the operating frequency increases. Therefore, it is effective and important to design high frequency WPT systems. There are, however, technical limitations for its achievement. From the circuit theory point of view, there are two major factors for overall efficiency degradation. One is power losses at coupled coils induced by high equivalent series resistances (ESRs) of themselves and the other is losses at power converters. Previous researches of WPT systems have only been focusing on enhancing the efficiency of the wireless coupled part, namely the coupled coils. New coil shapes, materials, and design methods have been developed, which leads to better performance. It is, however, also important to enhance the power-conversion efficiency of the power converters for achieving high overall efficiency.

In inductively coupled WPT systems, high-frequency resonant dc-ac inverters are mainly utilized as a dc-ac inverter. This is because inductive coupled WPT systems are operated at resonance or near resonance. Namely, the current flowing through the transmitting coil has to be a sinusoidal current. Basically, high-frequency resonant dc-ac inverters contain a resonant circuit and a transistor as a switching device. By using the transistor as a simple switch, the drain current and the drain-to-source voltage, which is called switch voltage, never appear simultaneously at the transistor. Therefore, the power losses at the transistor are drastically suppressed and high power-conversion efficiency can be achieved [7]. The class-D inverter is one of the resonant inverters. The class-D inverter has, however, the characteristic of the hard switching, where the hard switching means that the switch voltage is not zero at the turn-on instant. Due to a parasitic capacitance in actual switching devices, the stored energy in the capacitance is instantly dissipated as a heat at the turn-on instant, which is called "switching loss". Because switching losses occur at every switching, the amount of switching losses is proportional to the switching frequency. In the case that the switching number is low, namely the low frequency operation, the switching loss may be negligible. Conversely, the switching loss is dominant power-loss factor at high frequency class-D inverters. Although the dc-ac inverter should operate at a high frequency in the WPT system, the power-conversion efficiency of the class-D inverter decreases as the increase in the frequency.

The class-E inverter is also a resonant inverter. No switching loss occurs in the class-E inverter by satisfying the class-E zero-voltage switching and zero-derivative switching (ZVS/ZDS) conditions. The class-E ZVS/ZDS conditions mean that both the switch voltage and its derivative are zero at the turn-on instant. Therefore, the class-E inverter can achieve a high-power conversion efficiency at high frequencies, which is a big difference compared with the class-D hard-switching inverter. Since the introduction of the class-E inverter [8], many analytical descriptions of this circuit have been published. Additionally, many applications of the class-E inverter, such as dc-dc converter [9], inverter with impedance inverter [10], lamp ballast [11], high-power-factor inverter [12], and so on, were proposed. However, most of the previous researches have been focusing on the class-E inverter with the class-E ZVS/ZDS conditions, which is called “nominal operation” For achieving the class-E ZVS/ZDS conditions at the inverter, the component values should be determined uniquely. Namely, the class-E ZVS/ZDS conditions are achieved at a certain parameter set and non-nominal operations appear even when system parameters vary from the nominal conditions slightly. When a practical WPT system with the class-E inverter is considered, it is important to comprehend the characteristics of the WPT system against system parameter variations. For example, coupling-coefficient variation, which occurs due to the distance and location variations between the transmitter and the receiver, greatly affects the system performance, such as output power and overall efficiency. Therefore, it is necessary to analyze the class-E inverter outside the class-E ZVS/ZDS conditions, namely at any system parameter.

There are technical problems for the implementation of a high frequency class-E inverter. At high frequency operations, it is necessary to design the complex driver circuit for generating a high frequency driving signal. This problem can be solved by using a feedback power, which is a part of the output power, as a driving signal, which is related to an oscillation phenomenon. The class-E oscillator is the oscillator that has the class-E switching property. The oscillator is oscillated by the feedback voltage transformed from the output voltage [13], [14]. Therefore, there is no need to implement a driver circuit in the class-E oscillator. In addition, a high power conversion efficiency can be achieved in the oscillator because the oscillator operates without a driving signal and the feedback current is low compared with the output current. A limitation of the oscillator is that the free-running frequency, namely the oscillating frequency, usually has a small error from the specified frequency owing to component tolerances. In several applications of the class-E oscillator including the WPT system, accurately specified frequency operations are required for practical usage that considers the radio law and phase noise. The injection locking technique [15] is one the solutions for this problem.

In the injection-locked class-E oscillator [16], the injection circuit is added to the class-E free-running oscillator for oscillation frequency stabilization. When the feedback voltage of the free-running class-E oscillator is synchronized with the small injection signal, the frequency of the class-E oscillator can be fixed at the injection signal frequency. Analytical expressions of the locking ranges have been previously reported in [16] on the basis of Adler's equation [15]. Although the locking ranges of injection-locked class-E oscillator can be approximately estimated, this analysis is only valid for the case in which the injection signal is a sinusoidal waveform. For the implementation point of view, it is useful to predict the locking ranges on various injection-signal waveforms.

In recent researches about WPT systems, traditional rectifiers, which are the half-wave rectifier and the bridge rectifier, have been used as ac-dc converters. The main losses in the rectifier are the conduction loss and the switching loss of the rectifying element. The switching loss of the ac-dc rectifier can be also reduced by applying the class-E switching technique as well as the dc-ac inverter. Additionally, the half-wave rectifier and the bridge rectifier have a non-sinusoidal input current. This affects the performance of the transmitter, namely the dc-ac inverter, because the typical transmitter operates at resonance or near resonance and generates a sinusoidal current.

The class-E rectifier is one of the rectifiers, which converts a sinusoidal voltage into a dc voltage. This rectifier can have a sinusoidal input current, which is the difference from the traditional rectifiers [17]. Additionally, the class-E rectifier can achieve a high power-conversion efficiency at high frequencies because of the class-E ZVS/ZDS at the turn-off instant. From these specifications, it is suitable to apply the class-E rectifier to

WPT systems for enhancing the overall efficiency.

1.2 Research Works

This thesis presents analyses and designs of the class-E switching circuits for inductively coupled WPT systems.

First, analytical expressions for steady-state waveforms, output power, and power conversion efficiency of the class-E inverter outside the class-E ZVS/ZDS conditions at a high Q and any duty ratio are presented. By considering non-nominal operations, the applicable parameter range of the analytical expressions is much wider than that of the previous analytical expressions. By carrying out the PSpice simulations and the circuit experiments, it is shown that the analytical predictions agreed with the simulated and the experimental results quantitatively, which validates the accuracy of the obtained analytical expressions. These analytical expressions can be applied to WPT systems with the class-E inverter.

Second, a numerical locking-range prediction for the injection-locked class-E oscillator using the phase reduction theory (PRT) is presented. This high power-conversion efficiency oscillator can be utilized in WPT systems. By applying this PRT to the injection-locked class-E oscillator designs, the locking ranges of the oscillator on any injection-signal waveform can be efficiently obtained. The locking ranges obtained from the proposed method quantitatively agreed with those obtained from the simulations and circuit experiments, showing the validity and effectiveness of the locking-range derivation method based on PRT.

Third, an analytical design procedure and an efficiency-enhancement theory for the inductive coupled WPT system with class-E^2 dc-dc converter, which consists of the class-E inverter and the class-E rectifier, are presented. By using the analytical expressions, it is possible to obtain component values of the class-E^2 WPT system for achieving the class-E ZVS/ZDS conditions. Additionally, the analytical expressions suggest designers how to determine the component values for power-delivery efficiency enhancement. I propose that component values of the rectifier are used for the power-delivery efficiency enhancement and the output power is adjusted by the inverter component values. The analytical predictions agree with the PSpice-simulation and experimental results quantitatively, which showed the validities of the analytical expressions and the design procedure. In the laboratory experiment, the WPT system for 10 cm coil distance achieved 77.1 % power-delivery efficiency with 10 W (50 Ω/22.4 V) output power at 1 MHz operating frequency.

Fourth, analytical expressions of the class-E^2 WPT system at any system parameter are presented. By considering non-nominal operations of the class-E inverter, system behavior at any system-parameter set can be expressed accurately. For example, the output power and the power-delivery efficiency as functions of coupling coefficient and load resistance are given. It is clarified from the analytical expressions that the ZVS condition is always satisfied when the coupling coefficient decreases or the load resistance increases from the nominal value. Additionally, the switching-pattern distribution map of the class-E^2 WPT system in a parameter space is illustrated from the analytical expressions. By using the distribution map, the WPT system achieving the ZVS at any load resistance conditions can be designed, which is one of the applications of the analytical expressions. The analytical predictions agreed with the PSpice-simulation and experimental results quantitatively, which showed the validities of the analytical expressions.

These results enhance the power-delivery efficiency of the WPT systems and give designers the comprehension of system performances. It is expected that the results in this thesis contribute to efficient-energy usage and comprehensive understanding in WPT systems.

1.3 Outline of Thesis

Figure 1.1 shows an outline of this thesis and relationship among chapters and sections.

Chapter 2 is dedicated to the basics of the inductive coupling WPT system. It starts off with a summary of magnetic induction theory and then delves into coupling states of coils, which are the loosely inductive coupling and the resonant inductive coupling. The resonant class-D and -E inverters and the class-E oscillator along with the injection-lock technique are introduced as dc-ac inverters. Additionally, the class-D and -E rectifiers are shown as ac-dc converters.

Chapter 3 shows waveform equations, output power, and power conversion efficiency for the class-E inverter outside the class-E zero-voltage switching and zero-derivative switching (ZVS/ZDS) conditions. By considering non-nominal operations, the applicable parameter range of the analytical expressions is much wider than that of the previous analytical expressions.

Chapter 4 proposes a numerical locking-range prediction for the injection-locked class-E oscillator using the phase reduction theory (PRT) is presented. By applying this method to the injection-locked class-E oscillator designs, the locking ranges of the oscillator on any injection-signal waveform can be efficiently obtained.

Chapter 5 shows an analytical design procedure and an efficiency-enhancement theory for the WPT system with class-E^2 dc-dc converter are presented. By using the analytical expressions, it is possible to obtain component values of the class-E^2 WPT system for achieving the class-E ZVS/ZDS conditions. The presented analytical procedure and the efficiency enhancement theory can be adopted for other WPT systems.

Chapter 6 shows analytical expressions of the class-E^2 WPT system for any set of parameters are presented by considering non-nominal operations of the class-E inverter. Effects of coupling-coefficient and load variations to the system can be expressed by obtained analytical expressions. Additionally, a design of the system for achieving the ZVS at any load resistance is presented by using the analytical expressions.

Chapter 7 makes overall conclusions and gives future problems.

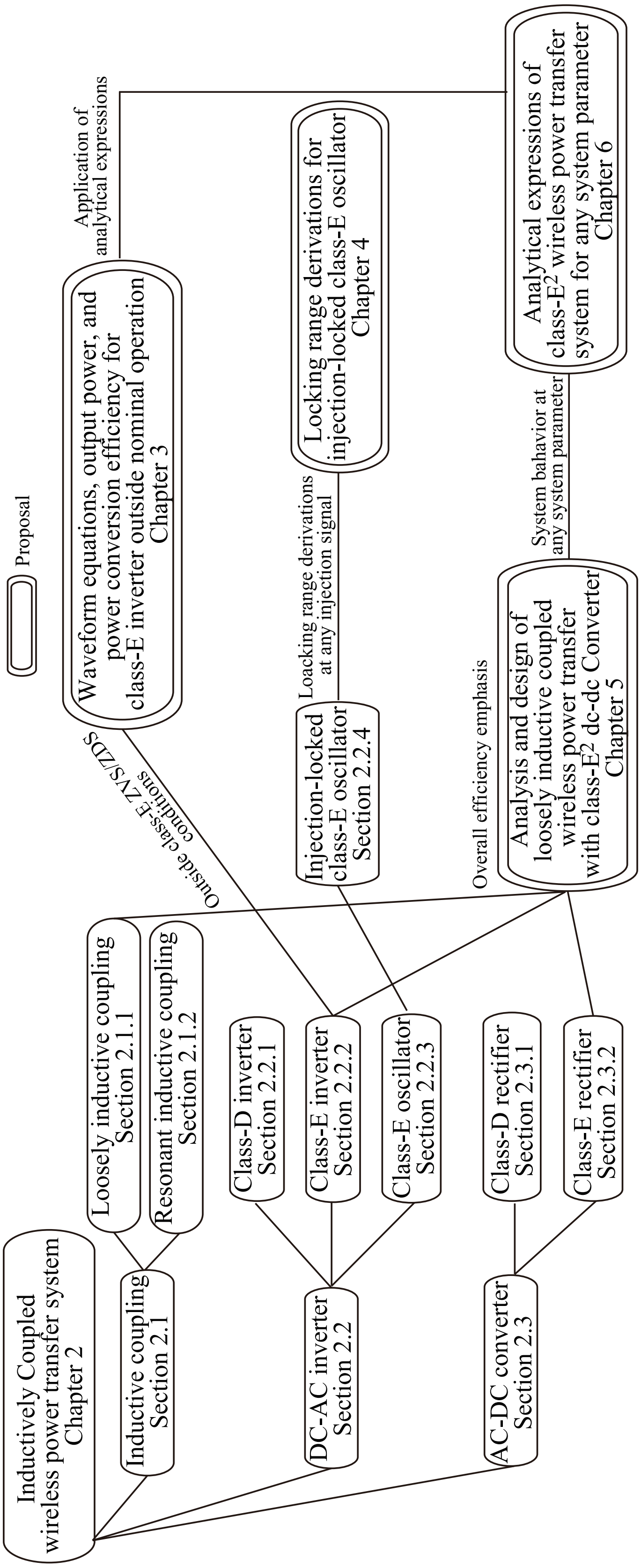

Figure 1.1: Outline of this thesis.

Reference

[1] N. Tesla, *The Wireless Tesla,* Wilder Publications, 2007.

[2] W. C. Brown, “A survey of the elements of power transmission by microwave beam”, *In IRE International Conference,* pp. 93–105, Sept. 1961.

[3] A. Kurs, A. Karalis, R. Moffatt, J. D. Joannopoulos, P. Fisher, and M. Soljačić, “Wireless power transfer via strongly coupled magnetic resonances,” *Sci. Express,* vol. 317, no. 5834, pp. 83–86, Jul. 2007.

[4] K. V. Schuylenbergh and R. Puers, *Inductive Powering: Basic Theory and Application to Biomedical Systems.* New York: Springer-Verlag, Jul. 2009.

[5] [Online] Qi: Wireless power consortium, http://www.wirelesspowerconsortium.com, Accessed Jan. 2014.

[6] [Online] Rezence: Alliance for wireless power, http://www.rezence.com, Accessed Jan. 2014.

[7] M. K. Kazimierczuk, *RF Power Amplifiers.* New York, NY: John Wiley & Sons, 2008.

[8] N. O. Sokal and A. D. Sokal, “Class E - A new class of high-efficiency tuned single-ended switching power amplifiers,” *IEEE Jounal of Solid State Circuits*, vol. 10, no. 3, pp. 168–176, Jun. 1975.

[9] I. Boonyaroonate and S. Mori, “Analysis and design of class E isolated DC/DC converter using class E low *dv/dt* PWM synchronous rectifier,” *IEEE Trans. Power Electron.*, vol. 16, no. 4, pp. 514–521, Jul. 2001.

[10] M. K. Kazimierczuk and X. T. Bui, “Class-E amplifier with an inductive impedance inverter,” *IEEE Trans. Ind. Electron.*, vol. 37, no. 2, pp. 160–166, Apr. 1990.

[11] Y. C. Chuang, Y. L. Ke, H. S. Chuang, and M. L. Chou, “Electronic ballasts driven by hybrid source using microprocessor-controlled digital switching technique,” *IEEE Trans. Ind. Appl.*, vol. 47, no. 3, pp. 1452–1460, May/Jun. 2011.

[12] H. L. Cheng, C. A. Cheng, C. C. Fang, and H. C. Yen, “Single-switch high-power-factor inverter driving piezoelectric ceramic transducer for ultrasonic cleaner,” *IEEE Trans. Ind. Electron.*, vol. 58, no. 7, pp. 2898–2905, Jul. 2011.

[13] J. Ebert and M. Kazimierczuk, “Class E high-efficiency tuned power oscillator,” *IEEE J. Solid-State Circuits*, vol. SC-16, no. 2, pp. 62–66, Apr. 1981.

[14] M. K. Kazimierczuk, V. G. Krizhanovski, J. V. Rassokhina, and D. V. Chernov, “Class-E MOSFET tuned power oscillator design procedure,” *IEEE Trans. Circuits Syst. I,* vol. 52, no. 6, pp. 1138–1147, Jun. 2005.

[15] R. A. Adler, “Study of locking phenomena in oscillators, ” in *Proc. IRE,* Jun. 1946, vol. 34, no. 6, pp. 351–357.

[16] M. K. Kazimierczuk, V. G. Krizhanovski, J. V. Rassokhina, and D. V. Chernov,“Injection-locked class-E oscillator,” *IEEE Trans. Circuits Syst. I,* vol. 53, no. 6, pp. 1214–1222, Jun. 2006.

[17] M. K. Kazimierczuk, “Analysis of class E zero-voltage switching rectifier,” *IEEE Trans Circuit Syst.,* vol. 37, no. 6, pp. 747–755, Jun. 1990.

Chapter 2

Inductively Coupled Wireless Power Transfer System

●● ABSTRACT ●●

In this chapter, each part of the inductively coupled WPT system is explained. The WPT system basically consists of three parts, which are dc-ac inverter, inductive coupled coils, and ac-dc rectifier. The inductive and resonant coupling are mainly applied as the wireless coupling part in WPT systems. The inductive coupling is used for the applications that the distance and/or position between the transmitter and the receiver are relatively closed, namely strongly coupling. On the other hand, a high efficiency power transfer can be achieved by the resonant coupling even if the system has a loosely coupling. For achieving a high power-delivery efficiency in WPT systems, it is also important to enhance the power-conversion efficiencies both of the dc-ac inverter and the ac-dc rectifier. As high efficiency power converters, class-E inverter, class-E oscillator, and class-E rectifier are introduced in this chapter.

2.1 Introduction

Figure 2.1 shows a basic configuration of an inductively coupled WPT system. The WPT system consists of dc-ac inverter, inductive coupling part, and ac-dc rectifier [1]. The dc-input voltage is converted into a high frequency alternating current by the dc-ac inverter. The current flows through the transmitting coil of the coupling part, which transforms the current into a high frequency magnetic field. The magnetic field is received at the receiving coil, which transforms the magnetic field into an ac voltage. The ac voltage is converted into a dc voltage by the ac-dc rectifier. These are the operating principles of the WPT system.

The inductive coupling can be regarded as an ac transformer with a high leakage inductance. Such a transformer is called "loosely coupled transformer" [2]. A small amount of the magnetic flux generated by the transmitting coil is received in the receiving coil. As a result, the induced voltage of the receiving coil is generally low and the efficiency is also low in the case that the system has a loosely coupling transformer. The resonant coupling is the efficient solution of the loosely coupling transformer. By resonating the coupling coils with capacitances, the power is efficiently transferred even if the system has a loosely coupling transformer. This is because the real part of the reflected impedance in the inverter, which includes the rectifier and the coupling coils, is increased by the resonance. By assuming that only the power loss in the transmitting coil occurs in the inverter, the efficiency of the inverter part can be simply obtained as $1/(1 + R_{L1}/R_{eq})$, where R_{L1} is the equivalent series resistance of the transmitting coil and R_{eq} is the real part of the reflected impedance. Therefore, a high real part of the reflected impedance leads to a high power transfer efficiency.

Although the efficiency of the coupling part is important, the power-conversion efficiencies of the dc-ac inverter and the ac-dc rectifier should be taken into account for enhancing the overall efficiency of the WPT system. Because WPT systems are generally operated at resonance or near-resonance, a sinusoidal current has to be generated at the dc-ac inverter. Ideal sinusoidal current can be generated by linear amplifiers, which are class-A, -B, or -C amplifiers. However, these amplifiers have a low power-conversion efficiency characteristics since the drain current and the drain-to-source voltage waveforms overlap at the transistor [3]. Therefore, resonant inverters, which generate a sinusoidal current by switching operation and a resonant network, are generally used in WPT systems because of their high efficiency operation. The resonant inverters have a theoretical power-conversion efficiency of 100 % although 100 % efficiency may not be achieved due to the conduction losses in parasitic resistances and the switching losses. The switching loss is the dominant power loss in resonant inverters when the inverters operate at high frequencies and hard switching. Hard switching means that the voltage across the parasitic drain-source capacitor of the transistor is not equal to zero at turn-on timing. In that case, the energy stored in the parasitic drain-source capacitor is instantaneously dissipated as a heat at turn-on timing, which is called switching loss. The switching loss is proportional to the switching frequency. Therefore, a high frequency operation leads to a low power conversion efficiency of the inverter. For reducing the switching losses, the class-E zero-voltage and zero-derivative switching (ZVS/ZDS) technique was introduced. The class-E ZVS/ZDS are the conditions that the drain-source voltage of the transistor, which is generally referred to as switch voltage, and its derivative equal zero at the turn-on instant. By satisfying the class-E ZVS/ZDS in a resonant converter, the switching loss can be theoretically minimized to zero, which leads to a higher power-conversion efficiency operation in the resonant inverter.

For delivering the received power to a dc load, it is necessary to utilize an ac-dc converter. It is also important to enhance the power-conversion efficiency of the ac-dc converter for a high efficiency operation in WPT systems. In recent researches about WPT systems, traditional rectifiers, such as the half-wave rectifier, the bridge rectifier, and so on, have been used. The main losses in the rectifier are the conduction loss and the switching loss of the rectifying element. The half-wave rectifier and the bridge rectifier have a non-sinusoidal input current. This affects the performance of the transmitter, namely the inverter, because the typical transmitter operates at resonance or near resonance and generates a sinusoidal current. This problem can be solved by using a current-driven rectifiers, which can have a sinusoidal input current. In addition, the switching loss of rectifiers can be also reduced by applying the class-E ZVS/ZDS technique.

2.2 Inductive Coupling

2.2.1 Operating Principle of Inductive Coupling

When two circuits affect each other through a magnetic field generated by either one of the two, they are in the state of magnetically coupling or inductively coupling. Namely, two circuits are inductively coupled when a magnetic flux generated by the coil of one circuit enters the coil of the other one.

Faraday's law states that a voltage v is induced in a single coil as shown in Fig. 2.2(a), which is proportional to its number of turns N and time rate of change of the magnetic flux ϕ crossing the coil, namely

$$v = N\frac{d\phi}{dt}. \tag{2.1}$$

According to Ampere's law, the magnetic flux ϕ is expressed as

$$\phi = \frac{\mu_0 N A i}{w}, \tag{2.2}$$

where μ_0, A, and N are the permeability in vacuum, particularly $\mu_0 = 4\pi \cdot 10^{-7}$ H/m, the area and the width of the coil, respectively, From (2.2), (2.1) rewritten as

$$v = \frac{\mu_0 N^2 A}{w} \cdot \frac{di}{dt} = L\frac{di}{dt}. \tag{2.3}$$

This effect is called "self-induction". L is the self-inductance of the coil and

$$L = \frac{\mu_0 N^2 A}{w}, \tag{2.4}$$

If two coils are in each other's vicinity, a current i_1 in one coil L_1 sets up a magnetic flux ϕ_1 through the other coil L_2 as shown in Fig. 2.2(b). When this flux is changed by changing i_1, an induced voltage v_2 appears in L_2. From (2.1), the induced voltage v_2 is given as

$$v_2 = N_2\frac{d\phi_1}{dt}, \tag{2.5}$$

where N_2 is the number of L_2 coil windings. ϕ_1 is proportional to i_1, namely

$$v_2 = M_{12}\frac{di_1}{dt}. \tag{2.6}$$

In the same way, a current of L_2, namely i_2, induces a voltage on L_1, which is

$$v_1 = M_{21}\frac{di_2}{dt}. \tag{2.7}$$

In (2.6) and (2.7), M_{12} and M_{21} are the mutual inductances of L_1 with respect to L_2 and vice versa. From the principle of reciprocity, we have

$$M_{12} = M_{21} = M. \tag{2.8}$$

M is defined as the mutual inductance between two coils. It is proportional to the product N_1N_2 and depends on the geometry of the coils, coils' position, and surrounding materials that influence the magnetic field.

Two induction properties, which are the self-induction and the mutually induced voltage, act simultaneously. Thus, v_1 and v_2 as shown in Fig. 2.2(b) are described by following set of equations:

$$v_1 = L_1 \frac{di_1}{dt} + M \frac{di_2}{dt}, \tag{2.9}$$

$$v_2 = L_2 \frac{di_2}{dt} + M \frac{di_1}{dt}. \tag{2.10}$$

The above equations are reformulated in terms of the complex signal amplitude as

$$V_1 = j\omega L_1 I_1 + j\omega M I_2, \tag{2.11}$$

$$V_2 = jL_2 I_2 + jM I_1. \tag{2.12}$$

where $\omega = 2\pi f t$ and f is the frequency of V_1.

In general, not all of the flux produced by L_1 is coupled to L_2. Namely, the magnetic flux leaks. Therefore, the mutual inductance can be expressed as

$$M = k\sqrt{L_1 L_2}, \tag{2.13}$$

where k is the coupling coefficient. When the two coils are tightly coupled so that all of the flux produced by L_1 enters L_2, $k = 1$. It is an ideal situation because it is impossible to wind two coils so that they share the same magnetic flux precisely.

2.2.2 Loosely Inductive Coupling

The strength of the coupling is expressed as the coupling coefficient k. For $k > 0.5$, the two coils are “tightly coupled” and for $k < 0.5$, they are “loosely coupled” [4]. An ac transformer with a magnetic core can be regarded as a tightly coupled transformer because it is generally wound around a common magnetic core. A magnetic core helps to share the magnetic flux each other. Therefore, the AC transformer has a high coupling coefficient at least 0.9. An ac transformer with an air gap can be regarded as a loosely coupled transformer. This is because a small amount of the magnetic flux is shared in the transformer due to an air gap, which leads to a low coupling coefficient. In inductively coupled WPT systems, coupled coils has inevitably an air gap. Therefore, the inductive coupling in the WPT system can be regarded as a loosely coupled transformer.

Figure 2.3(a) shows an example circuit to demonstrate the inductive coupling from the view point of circuit theory. The circuit consists of ac-voltage source v_1, coupled coils L_1 and L_2, ac-load resistance R_L, and equivalent series resistances (ESRs) of coils r_1 and r_2. The equivalent series resistance is also referred to as the parasitic resistance. From (2.11), (2.12), and Kirchhoff's voltage law (KVL), we have

$$V_1 = r_1 I_1 + j\omega L_1 I_1 - j\omega M I_2, \tag{2.14}$$

$$j\omega M I_1 = j\omega L_2 I_2 + r_2 I_2 + R_L I_2. \tag{2.15}$$

From the above equations, the impedance seen by the ac-voltage source Z_1, namely the reflected impedance, can be expressed as

$$Z_1 = \frac{V_1}{I_1} = r_1 + R_{eq} + j\omega L_{eq} = r_1 + \frac{\omega^2 M^2 (R_L + r_2)}{(R_L + r_2)^2 + \omega^2 L_2^2} + j\omega \left[L_1 - \frac{\omega^2 L_2 M^2}{(R_L + r_2)^2 + \omega^2 L_2^2} \right], \tag{2.16}$$

where R_{eq} and L_{eq} are the equivalent resistance and inductance in the transmitter side as shown in Fig. 2.3(b). Because only the conduction losses due to resistive components occur in this circuit, the overall efficiency of this circuit can be approximately obtained from (2.16) as

$$\eta_{LIC} = \frac{R_{eq}}{R_{eq} + r_1} \cdot \frac{R_L}{R_L + r_2} = \frac{1}{1 + \dfrac{r_1}{R_{eq}}} \cdot \frac{1}{1 + \dfrac{r_2}{R_L}}. \tag{2.17}$$

As given in (2.17), the overall efficiency η decreases as R_{eq} decreases. A loosely inductive coupling leads to the decreases in R_{eq} because of a low coupling coefficient k, namely a low M. Therefore, a loosely coupled WPT system suffers from a low efficiency property. Additionally, the power factor of v_1 may be low due to the imaginary part of Z_1. A high amplitude of i_1 is required for transferring a specified power. As a result, the conduction loss in r_1 increases as i_1 increases, which also leads to a low efficiency.

2.2.3 Resonant Inductive Coupling

The resonant inductive coupling is an effective solution for enhancing the efficiency of a loosely coupled transformer [5], [6]. There are four types of the resonant coupling [1], which are series-series, series-parallel, parallel-series, parallel-series types as shown in Fig. 2.4. Here, the series-series type is introduced because of its easily comprehensible expressions.

By applying the series capacitors C_1 and C_2, which are referred as the series resonant capacitor or the compensation capacitor, (2.16) can be rewritten as

$$\begin{aligned} Z_{1ss} &= r_1 + \frac{\omega^2 M^2 (R_L + r_2)}{(R_L + r_2)^2 + \left(\omega L_2 - \dfrac{1}{\omega C_2}\right)^2} \\ &\quad + j\left[\omega L_1 - \frac{1}{\omega C_1} - \frac{\omega^2 M^2 \left(\omega L_2 - \dfrac{1}{\omega C_2}\right)}{(R_L + r_2)^2 + \left(\omega L_2 - \dfrac{1}{\omega C_2}\right)^2}\right]. \end{aligned} \tag{2.18}$$

At resonance, namely $\omega L_1 = 1/\omega C_1$ and $\omega L_2 = 1/\omega C_2$, (2.18) is

$$Z_{1ssr} = r_1 + R_{eqr} = r_1 + \frac{\omega^2 M^2}{(R_L + r_2)^2}. \tag{2.19}$$

As given in (2.19), the equivalent resistance R_{eqr} is maximized by the resonance. In addition, the imaginary part is equal to zero, which leads to the unity power factor of v_1. As a result, a high efficiency can be achieved and more power can be delivered to the load resistance compared with the non-resonant coupling. On the other hand, R_{eqr} increases as the operating frequency increases. Therefore, it is effective to operate in high frequencies for enhancing efficiency of coupling part. However, when a system operates in higher frequencies, ESRs of coils r_1 and r_2 become higher because of the proximity effect and the skin effect [2]. From these facts, the design of inductively coupled WPT systems has lots of difficulties for maximizing the efficiency.

2.2.4 Standardization activities for Inductive Coupling WPT systems

In order to create universal standards for inductive coupling wireless power charging systems, some associations have been established, such as “Wireless Power Consortium (WPC)” and “Alluance for Wireless Power (A4WP)”. The WPC standard is referred as “Qi” [7]. The Qi standard was introduced for charging of portable devices. Systems under the Qi standard transfer around 5 W power to a load by near field magnetic induction between planar coils and operate at frequencies in the range of 100 to 205 kHz. The distance between coils is typically 5 mm. Figure 2.5 shows the basic system configuration of the Qi standard [7]. “Power Transmitter” consists of “Power Conversion Unit” and “Communication and Control Unit” as shown in Fig. 2.5. An alternative current is generated by the Power Conversion Unit and the current is fed into the primary coil for generating a magnetic field. The Communications and Control Unit regulates the transferred power to the level, which is requested by “Power Receiver”. “Power Receiver” consists of “Power Pick-up Unit” and “Communications and Control Unit” as shown in Fig. 2.5. A magnetic field generated by the Power Transmitter is captured by the secondary coil and it is converted into an alternative current. The current is rectified by the Power Pick-up Unit. The Communications and Control Unit regulates the transferred power to the level, which is appropriate for the subsystems connected to the output of the Power Receiver.

The A4WP standard is referred as “Rezence” [8]. Although the Rezence was also developed for charging of portable devices, its aim is for improving the power range and spatial freedom of devices. Systems under the Rezence standard transfer up to 50 W power to a load by resonant inductive coupling and operate at the frequency of 6.78 MHz. Up to eight devices can be powered from a single transmitter depending on transmitter and receiver geometry and power levels. Figure 2.6 shows the basic configuration of the Rezence standard [8]. “Power Transmitting Unit (PTU)” consists of three main units which are a resonantor and matching unit, a power conversion unit, and a signaling and control unit. “Power Receiving Unit (PRU)” also consists of three main unit like the PTU. The Bluetooth Smart Link is implemented for control of output power, identification of valid loads, and protection of non-compliant devices. The control and communication protocol is designed as bidirectional and is used to provide feedback to enable efficiency optimization, over-voltage protection, under-voltage avoidance, and rouge object detection.

2.3 DC-AC Inverter

2.3.1 Class-D Resonant Inverter

The class-D resonant inverter was invented in 1959 by Baxandall [10]. The circuit consists of two switches, namely transistors, and a series-resonant circuit. The switches are driven in a way that they are alternately switched ON and OFF. If the loaded quality factor of the resonant circuit is sufficiently high, the current through the resonant circuit is sinusoidal wave and the currents through the switches are half-wave sinusoidal. The voltages across the switches are square wave, whose amplitudes are dc-supply voltage.

Figure 2.7(a) shows the circuit topology of the class-D inverter [9]-[19]. The inverter consists of dc-supply voltage V_I, two switches S_1 and S_2, and resonant circuit $L - C - R$. The switches are driven by non-overlapping rectangular-wave voltages v_{g1} and v_{g2} at the operating frequency f. Namely, the switches are alternately ON and OFF.

The analysis of the class-D inverter is based on the following assumptions:

a) The series resonant circuit, which is tuned to the operating frequency f, namely $f = 1/2\pi\sqrt{LC}$, is ideal, resulting in a sinusoidal current.

b) The switches act as ideal switches, namely they have zero on-resistances, infinite off-resistances, zero switching times, and null output capacitance.

c) All components are ideal.

d) The circuit operations are considered in the interval $0 \leq \theta < 2\pi$, where $\theta = 2\pi f t$ is the angular time.

From the above assumptions, the equivalent circuit of the class-D inverter is illustrated in Fig. 2.7(b).

Assuming a 50 % duty ratio of the switches, the switch voltage $v_{s1}(\theta)$ is a periodical square wave as shown in Fig. 2.8.

$$v_{s1} = \begin{cases} V_I, & \text{for } 0 \leq \theta < \pi \\ 0, & \text{for } \pi \leq \theta < 2\pi \end{cases} \tag{2.20}$$

By applying Fourier analysis to (2.20), we have

$$v_{s1}(\theta) = V_I \left(\frac{1}{2} + \frac{2}{\pi} \sum_{n=1}^{\infty} \frac{\sin(2n-1)\theta}{2n-1} \right). \tag{2.21}$$

Because of the assumption a), the output current is sinusoidal, namely

$$i_o(\theta) = I_o \sin\theta = \frac{2V_I}{\pi R} \sin\theta, \tag{2.22}$$

which gives a sinusoidal output voltage

$$v_o(\theta) = V_o \sin\theta = \frac{2V_I}{\pi} \sin\theta. \tag{2.23}$$

The collector currents i_{s1} and i_{s2} are half sinusoidal with the amplitude I_o.

The output power, which is dissipated in the load resistance R_L, is given as

$$P_o = \frac{I_o^2 R}{2} = \frac{2V_I^2}{\pi^2 R} \approx 0.2026 \frac{V_I^2}{R}. \tag{2.24}$$

The dc-input power is

$$P_I = V_I I_I = \frac{2V_I^2}{\pi^2 R} = P_o. \tag{2.25}$$

Therefore, the collector efficiency is 100 %.

$$\eta = \frac{P_o}{P_I} = 1. \tag{2.26}$$

2.3.2 Class-E Resonant Inverter

The class-E resonant inverter was introduced in 1975 by the Sokals [20] By satisfying the class-E zero-voltage switching (ZVS) and zero-derivative switching (ZDS) conditions in this inverter, high efficiency operation can be achieved at high frequencies.

Figure 2.9(a) shows a circuit topology of the class-E inverter [3], [9], [20]-[28]. The inverter consists of dc-supply voltage V_I, dc-feed inductor L_C, switch S, shunt capacitor C_S, and series resonant circuit $L - C - R$. Example waveforms are shown in Fig. 2.10. The switch S is driven by v_g. When the switch voltage v_S satisfies the class-E ZVS/ZDS conditions at turn-on instant, which are expressed as

$$v_S(\pi) = 0 \ \ and \ \ \left.\frac{dv_S}{d\theta}\right|_{\theta=\pi} = 0, \tag{2.27}$$

the class-E inverter can achieve high power-conversion efficiency at high frequencies, where the switch-on duty ratio is assumed as 50 %. This is because the switching loss is minimized by the class-E ZVS/ZDS conditions.

The analysis below is based on the following assumptions:

a) The switch acts as an ideal switch, namely it has zero on-resistances, infinite off-resistances, zero switching times, and null output capacitance.

b) The dc-feed inductance L_C is high enough so that the current through the dc-feed inductance is dc-input current I_I.

c) The loaded Q-factor of the resonant network, which is defined as $Q = \omega L/R$, is high enough to generate a pure sinusoidal resonant current i_o with operating frequency f.

d) All components are ideal.

e) The switch voltage satisfies the class-E ZVS/ZDS conditions.

f) The circuit operations are considered in the interval $0 \leq \theta < 2\pi$. The switch-on duty ratio is 50 %.

From the above assumptions, the equivalent circuit of the class-E inverter is illustrated in Fig. 2.9(b).

Because of the assumption c), the current through the series-resonant circuit is sinusoidal and given by

$$i_o = I_o \sin(\theta + \phi), \tag{2.28}$$

where I_o is the amplitude of i_o and ϕ is the phase shift between the driving signal v_g and i_o as shown in Fig. 2.10.

For $0 \leq \theta < \pi$, the switch is in on state. Therefore, the switch current i_S is expressed as

$$i_S(\theta) = 0. \tag{2.29}$$

On the other hand, the current through the shunt capacitor is

$$i_{C_S} = I_I - I_o \sin(\theta + \phi). \tag{2.30}$$

From (2.30), the switch voltage can be obtained as

$$v_S(\theta) = \frac{1}{\omega C_S} \int_{\pi}^{\theta} [I_I - I_o \sin(\theta' + \phi)] d\theta' = \frac{I_I(\theta - \pi) + I_o[\cos(\theta + \phi) - \cos(\pi + \phi)]}{\omega C_S}. \tag{2.31}$$

By applying the class-E ZVS/ZDS conditions, the dc-input current I_I is

$$I_I = -\frac{2I_o}{\pi} \cos\phi, \tag{2.32}$$

and

$$I_I = -I_o - \sin\phi, \tag{2.33}$$

From (2.32) and (2.33), the phase shift for satisfying the class-E ZVS/ZDS conditions is

$$\phi = \pi - \tan^{-1}\left(\frac{2}{\pi}\right) = 2.574 \text{ rad} = 147.5^\circ. \tag{2.34}$$

From (2.31), the dc-voltage supply is expressed as

$$V_I = \frac{1}{2\pi}\int_{\pi}^{2\pi} v_S(\theta)d\theta = \frac{I_I}{\pi\omega C_S}. \tag{2.35}$$

The voltages across the load resistance and the is

$$v_R = i_o R = V_R \sin(\theta + \phi). \tag{2.36}$$

For satisfying the class-E ZVS/ZDS conditions, the resonant circuit should be inductive because it is required that the current through the resonant circuit has a phase delay. In this analysis L is divided into L_r and L_x, where L_0 are C realize resonant filter with ω as shown in Fig. 2.9(b). The fundamental component of the voltage across the inductance L_x is

$$v_{L_x} = V_{L_x}\cos(\theta + \phi), \tag{2.37}$$

where $V_{L_X} = \omega L_x I_o$.

By applying Fourier trigonometric series formula to (2.31), the amplitudes V_R and V_{L_x} are obtained as

$$V_R = \frac{1}{\pi}\int_{\pi}^{2\pi} v_s \sin(\theta + \phi)d\theta = \frac{4}{\sqrt{\pi^2+4}}V_I \approx 1.074V_I. \tag{2.38}$$

and

$$V_{L_x} = \frac{1}{\pi}\int_{\pi}^{2\pi} v_s \cos(\theta + \phi)d\theta = \frac{\pi(\pi^2-4)}{4\sqrt{\pi^2+4}}V_I \approx 1.2378V_I. \tag{2.39}$$

From (2.38), the output power is obtained as

$$P_o = \frac{V_R^2}{2R} = \frac{8}{\pi^2+4}\frac{V_I^2}{R} \approx 0.5768\frac{V_I^2}{R}. \tag{2.40}$$

2.3.3 Class-E Oscillator

The class-E oscillator is composed of a class-E inverter and a positive-feedback network. A part of the output power is transmitted to the switch gate through the feedback network. Thus, the class-E oscillator can generate an ac power without a switch driving voltage, which is related to v_g in Fig. 2.9(a). Because of the class-E ZVS/ZDS conditions, the oscillator can achieve high power-conversion efficiency at high frequencies

Figure 2.11(a) shows a circuit topology of the class-E oscillator [29]-[36]. In this circuit, the feedback network consists of voltage dividing capacitors C_1 and C_2, feedback inductor L_f, and resistors R_{d1} and R_{d2} for supplying a bias voltage across the gate-to-source of the switch. Because the switch turns on when the gate-to-source voltage is higher than the gate threshold voltage V_{th}, the resistors R_{d1} and R_{d2} are necessary in the oscillator. Figure 2.12 shows example waveforms of the class-E oscillator. The feedback voltage v_f controls the switch. During $v_f \geq V_{th}$, the switch is in the "on" state. On the contrary, in the case of $v_f < V_{th}$, the switch is in the "off" state. During the switch to the off state, the current through the shunt capacitance C_S produces a pulse-like shape of the voltage across the switch, . The switching losses are reduced to zero by satisfying the class-E ZVS/ZDS conditions. In addition, the switch is controlled by a low feedback power, which also leads to a high efficiency operation in the oscillator.

2.3.4 Injection-Locked Class-E Oscillator

A limitation of the class-E oscillator is that the free-running frequency, which is also referred as the oscillation frequency, usually has a small error from the specified frequency owing to component tolerances. Therefore, accurately specified frequency operations are required for practical usage that considers the radio law and phase noise. The injection locking technique [36]-[41] is one solution for this problem. The injection lock allows the oscillator to achieve a high overall efficiency and a high stability of oscillation frequency. Both the frequency and the amplitude of the output voltage of injection-locked oscillators are stable if an injection signal falls within the injection-locking range.

Figure 2.13 shows a circuit topology of the injection-locked class-E oscillator [36]. This circuit consists of the class-E oscillator and the injection circuit, which is composed of injection signal v_{inj}, dc-blocking capacitor C_{inj}, and current-limiting resistor R_{inj}. There are several type of injection circuits [37]-[41]. It is easy to achieve synchronization as the injection signal power increases. However, a high power injection affects the waveforms of the feedback voltage and switch-on duty ratio, which yields the design complexity. It is necessary to conduct the total design of the free-running oscillator and injection circuits for large perturbation. Additionally, a low injection-signal power is good from a power-added efficiency perspective.

2.4 AC-DC Converter

2.4.1 Class-D Rectifier

The class-D rectifier converts a sinusoidal voltage or current into a DC voltage or current. The input source may be either a sinusoidal current source or a sinusoidal voltage. Rectifiers that are driven by a current source are called “current-driven rectifiers” [9], [42]-[44]. The diode current and voltage waveforms of the class-D rectifier are similar to the corresponding switch waveforms of the class-D inverter. Therefore, this rectifier is referred as the class-D rectifier.

Figure 2.14(a) shows a circuit topology of the class-D current-driven rectifier [9], [42]-[44]. This rectifier is consists of sinusoidal current source i_s, two diodes D_1 and D_2, large filter capacitor C_f, and dc-load resistor R_L. Figure 2.15 shows example waveforms of the class-D rectifier. For $i_s > 0$, D_1 is in on state and D_2 is in off state. The current through the diode D_1 charges the filter capacitor D_f For $i_s < 0$, D_2 is in on state and D_1 is in off state. In this state, D_2 acts as a freewheeling diode and provides the path for current i_s. The on-duty ratio is 50 %.

The analysis below is based on the following assumptions:

a) The diodes act as ideal switches, namely they have zero on-resistances, infinite off-resistances, zero switching times, and null parallel-parasitic capacitance.

b) The filter capacitance C_f is large enough such that the output voltage is a dc voltage V_o.

c) The rectifiers are driven by an ideal sinusoidal current source.

d) All components are ideal.

e) The circuit operations are considered in the interval $0 \leq \theta < 2\pi$.

From the above assumptions, the equivalent circuit of the class-E inverter is illustrated in Fig. 2.14(b).

Because of the assumption c), the input current is

$$i_s = I_s \sin\theta, \tag{2.41}$$

where I_s is the amplitude of i_s. The current through the diode D_1 is expressed as

$$i_{D1} = \begin{cases} I_s \sin\theta, & \text{for } 0 \leq \theta < \pi \\ 0, & \text{for } \pi \leq \theta < 2\pi \end{cases} \tag{2.42}$$

From (2.42), the dc component of the output current is

$$I_o = \frac{1}{2\pi}\int_0^{2\pi} i_{D1} d\theta = \frac{I_s}{\pi}. \tag{2.43}$$

The dc output current I_o is proportional to I_s. The dc component of the output voltage is

$$V_o = I_o R_L = \frac{I_s R_L}{\pi}. \tag{2.44}$$

V_o is also proportional to I_s.

The output power is

$$P_o = I_o^2 R_L. \tag{2.45}$$

2.4.2 Class-E Rectifier

The class-E rectifier is the counterparts of the class-E inverter. This is because the waveforms of the class-E rectifier are reversed versions of those of the class-E inverter. The class-E rectifier autonomously achieves the class-E ZVS/ZDS conditions at turn off instant. Because of the class-E ZVS/ZDS conditions, the switching loss and noise can be reduced.

Figure 2.16(a) shows a circuit topology of the class-E rectifier [9], [45]-[49]. This circuit consists of sinusoidal current source i_s, diode D, shunt capacitor C_D, low pass filter circuit $L_f - C_f$, and dc-load resistor R_L. The diode D works as a half-wave voltage rectifier and the rectified voltage is converted into a dc voltage through the low-pass filter $L_f - C_f$. Figure 2.17 shows example waveforms of the class-E rectifier for the diode on-duty ratio is 50 %. The input current i_s is a sinusoidal wave and the output current I_o is a constant value. While the diode D is in off state, the current $I_o - i_s$ flows through the shunt capacitor C_D. The diode turns on when the diode voltage decreases to the threshold voltage. While the diode D is in on state, the current $I_o - i_s$ flows through the diode D. At the diode turn-off transition, the capacitance current i_{C_D} is zero, resulting the zero derivative of the capacitance voltage dv_D/dt, as shown in Fig. 2.17. Therefore, the class-E rectifier autonomously satisfies the class-E ZVS/ZDS conditions at turn off instant.

The analysis below is based on the following assumptions:

a) The diode acts as an ideal switch, namely it has zero on-resistances, infinite off-resistances, zero switching times, and null parallel-parasitic capacitance.

b) The inductance and capacitance of the low pass filter L_f and C_f are large enough such that the output current V_o is constant.

c) The rectifiers are driven by an ideal sinusoidal current source.

d) All components are ideal.

e) The circuit operations are considered in the interval $0 \leq \theta < 2\pi$.

From the above assumptions, the equivalent circuit of the class-E inverter is illustrated in Fig. 2.16(b).

Because of the assumption c), the input current is

$$i_s = I_s \sin(\theta + \phi), \tag{2.46}$$

where I_s and ϕ are the amplitude of i_s and the phase shift indicated in Fig. 2.17.

For $0 < \theta \leq 2\pi(1 - D_d)$, where D_d is the diode on-duty ratio, the diode is in off state. From (2.46), the current through the shunt capacitor is expressed as

$$i_{C_D} = I_o - i_s = I_o - I_s \sin(\theta + \phi). \tag{2.47}$$

According to Fig. 2.17, $i_D(0) = 0$ and $i_{C_D} = 0$. Therefore, from (2.47,

$$I_o = I_s \sin\phi. \tag{2.48}$$

Thus, i_{C_D} is

$$i_{C_D} = I_o \left[1 - \frac{\sin(\theta + \phi)}{\sin\phi}\right] = I_o \left(1 - \cos\theta - \frac{\sin\theta}{\tan\phi}\right). \tag{2.49}$$

The diode voltage, namely the voltage across the shunt capacitance, is obtained as

$$v_D = \frac{1}{\omega C_D}\int_0^{\theta} i_{C_D}\,d\theta = \frac{V_o}{\omega C_D R_L}\left(\theta - \sin\theta + \frac{\cos\theta - 1}{\tan\phi}\right). \tag{2.50}$$

According to Fig. 2.17, $v_D(2\pi(1 - D_d)) = 0$. Substituting this condition into (2.50), the relationship between the diode on-duty ratio D_d and the phase shift ϕ is expressed as

$$\tan\phi = \frac{1 - \cos 2\pi D_d}{2\pi(1 - D_d) + \sin 2\pi D_d}. \tag{2.51}$$

The average value of the diode voltage is V_o because the dc component of the voltage across L_f is zero. Therefore, from (2.50),

$$\begin{aligned} V_o &= \frac{1}{2\pi}\int_0^{2\pi(1-D_d)} v_D\,d\theta \\ &= \frac{V_o}{2\pi\omega C_D R_L}\left[2\pi^2(1 - D_d)^2 + \cos 2\pi D_d - 1\frac{2\pi(1 - D_d) + \sin 2\pi D_d}{\tan\phi}\right]. \end{aligned} \tag{2.52}$$

From (2.52), the relationship between the diode on-duty ratio D_d and $\omega C_D R_L$ is obtained as

$$\omega C_D R_L = \frac{1}{2\pi}\left\{1 - 2\pi^2(1 - D_d)^2 - \cos 2\pi D_d + \frac{[2\pi(1 - D_d) + \sin 2\pi D_d]^2}{1 - \cos 2\pi D_d}\right\} \tag{2.53}$$

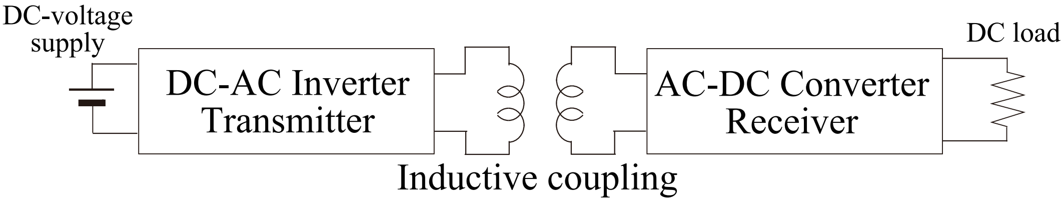

Figure 2.1: Basic configuration of inductive coupled WPT system.

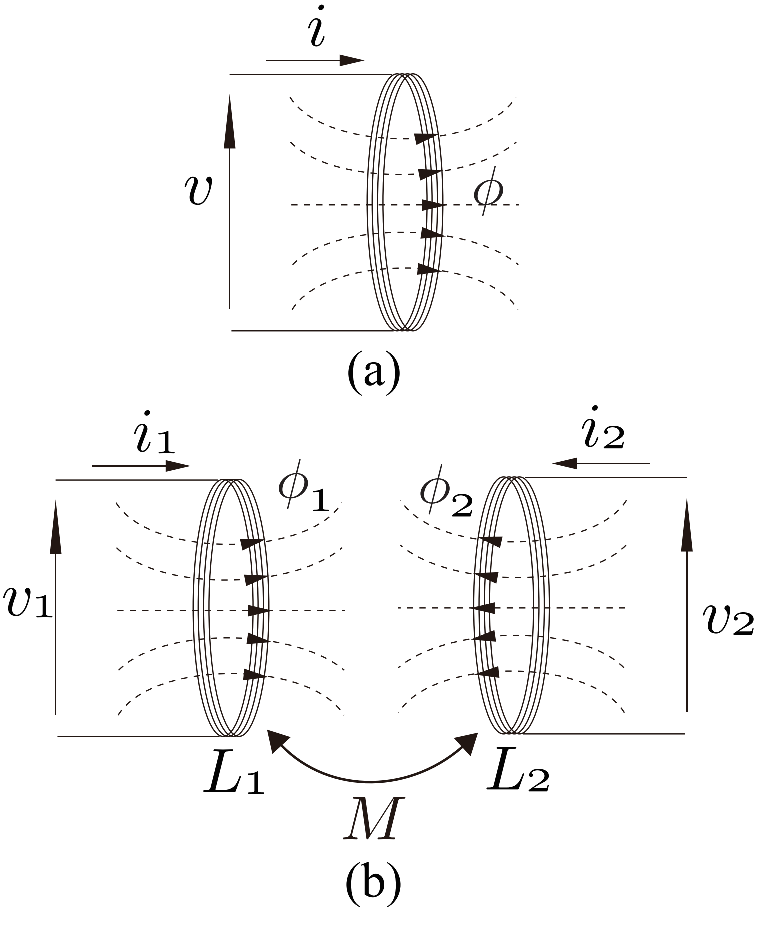

Figure 2.2: Principle operation of coils.

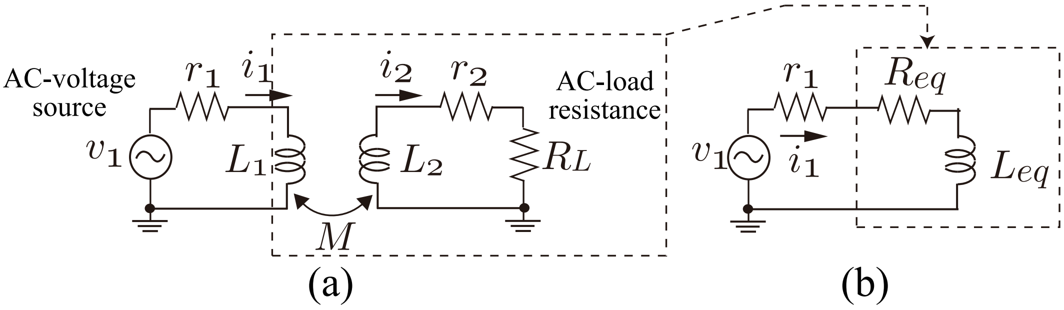

Figure 2.3: Example circuit of ac-ac WPT system.

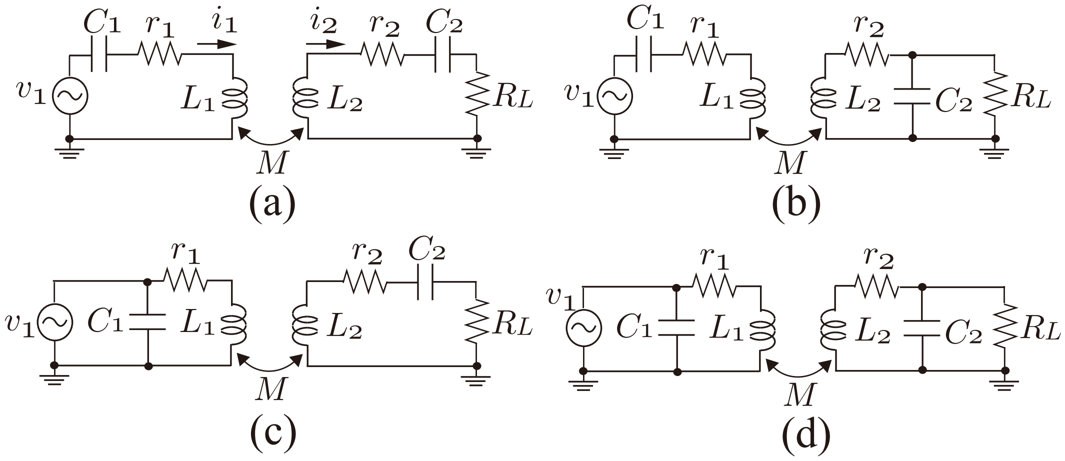

Figure 2.4: Types of resonant inductive coupling. (a) Series-series type. (b) Series-parallel type. (c) Parallel-series type. (d) Parallel-parallel type.

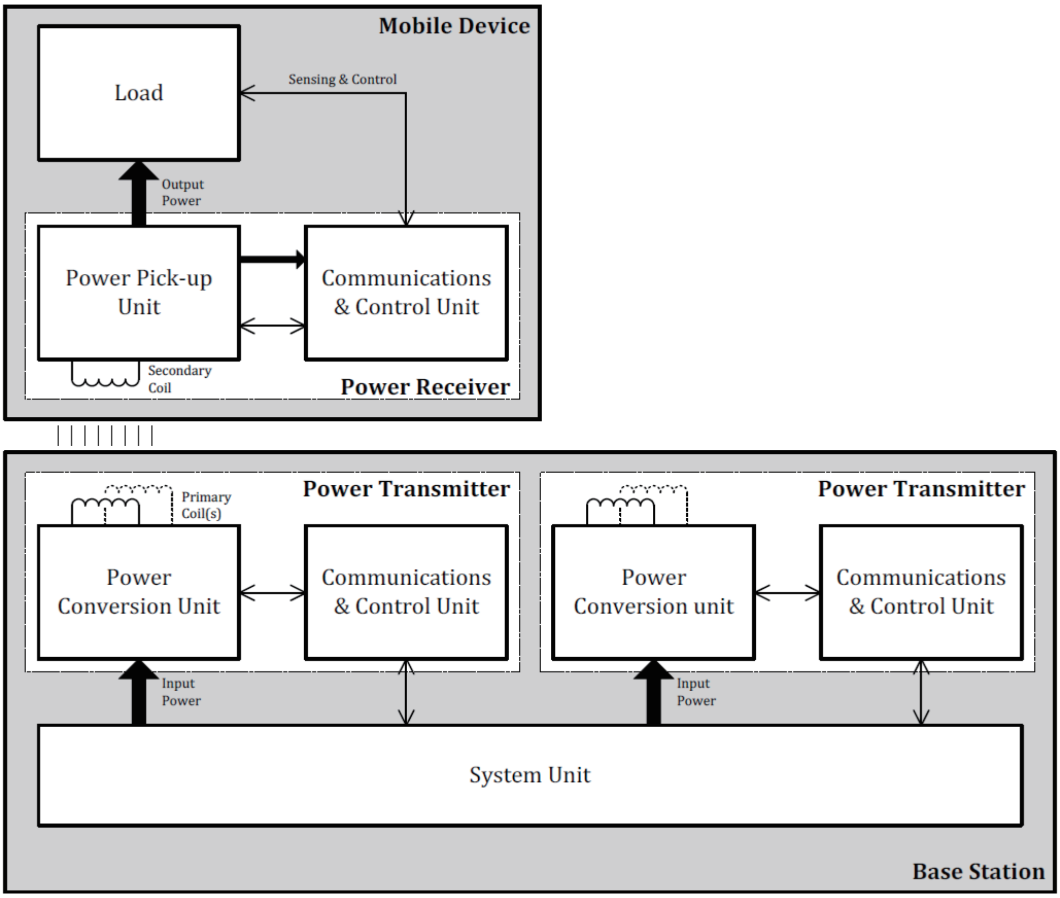

Figure 2.5: Basic system configuration of Qi standard.

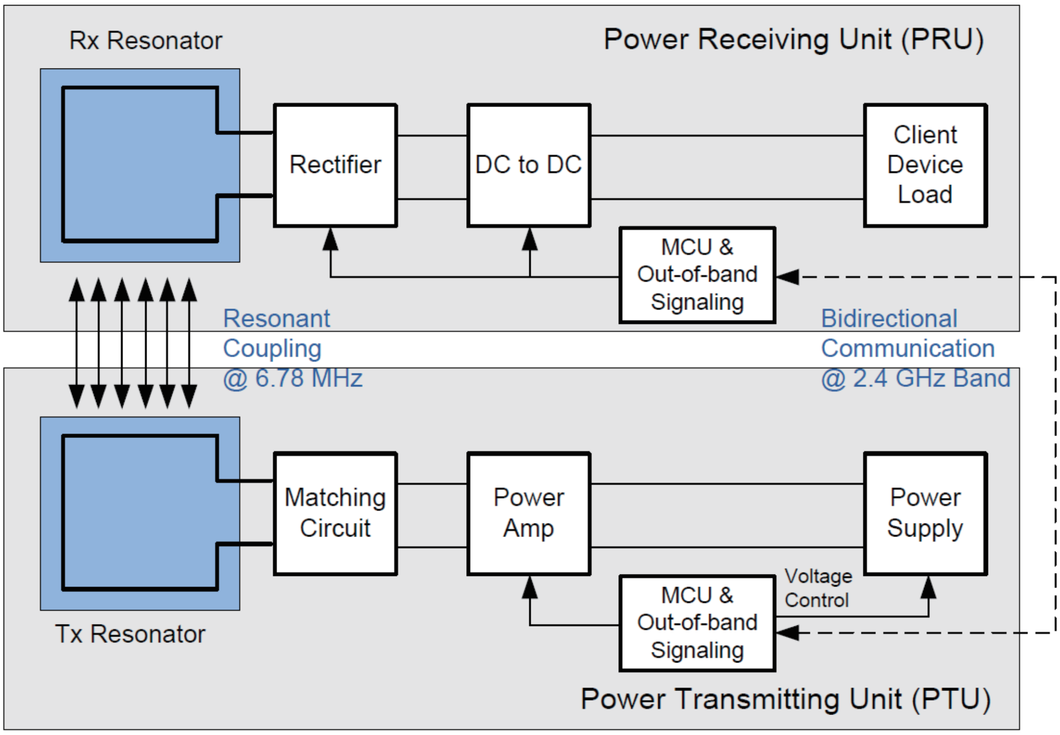

Figure 2.6: Basic system configuration of Rezence standard.

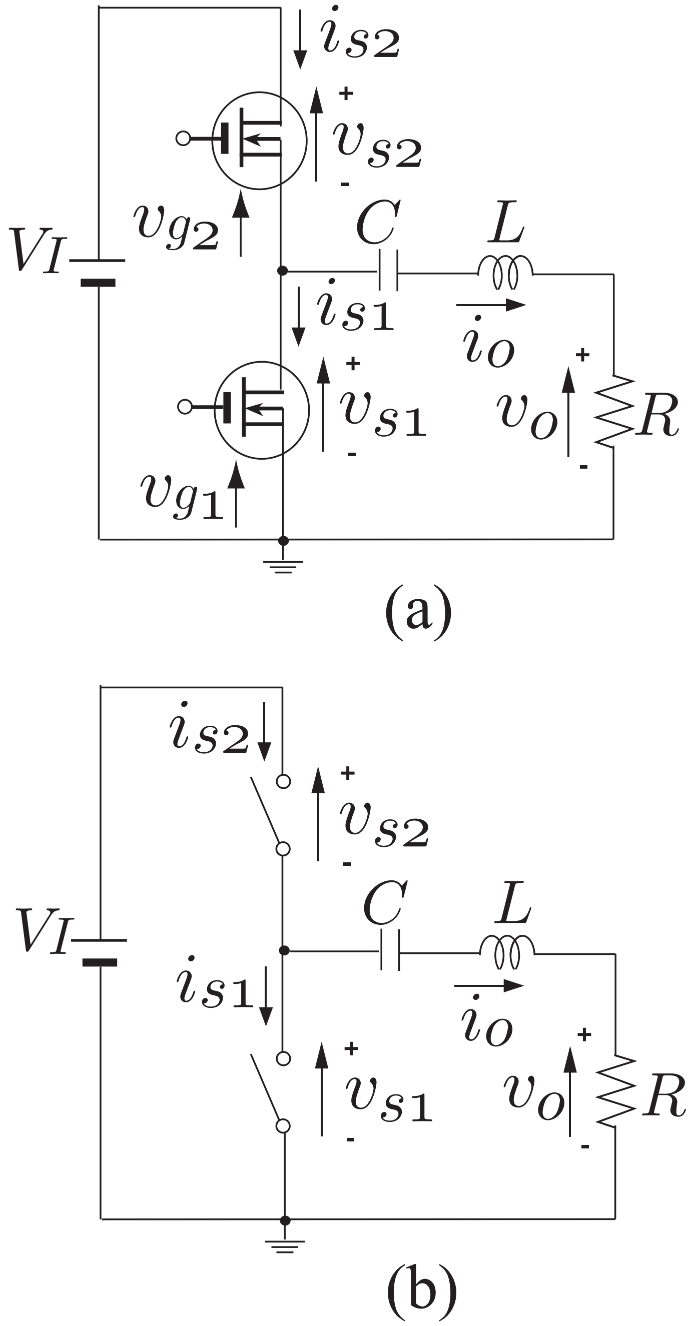

Figure 2.7: Class-D inverter. (a) Circuit topology. (b) Equivalent circuit.

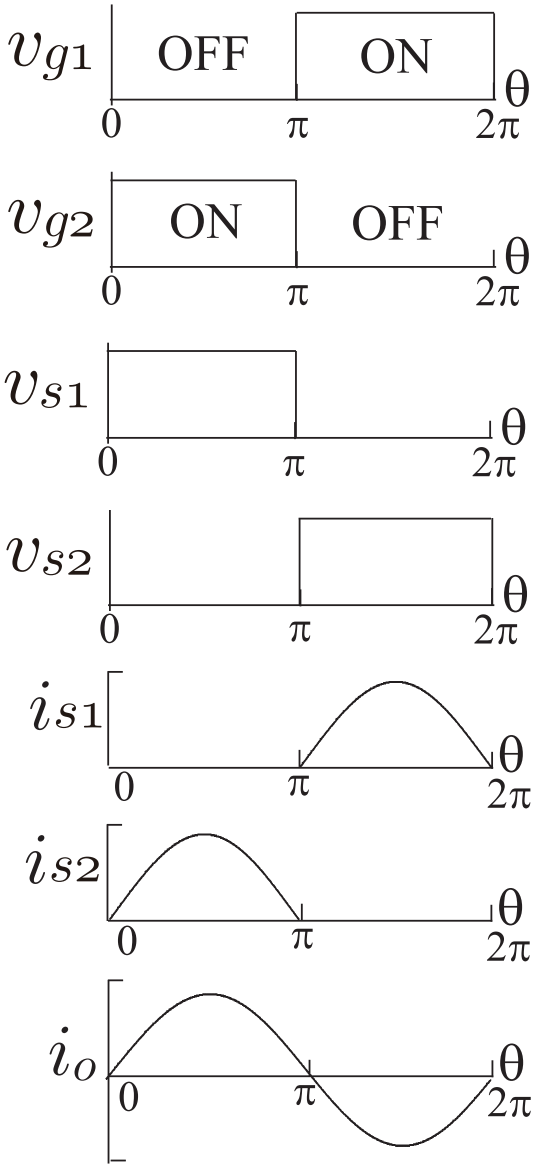

Figure 2.8: Waveforms of class-D inverter.

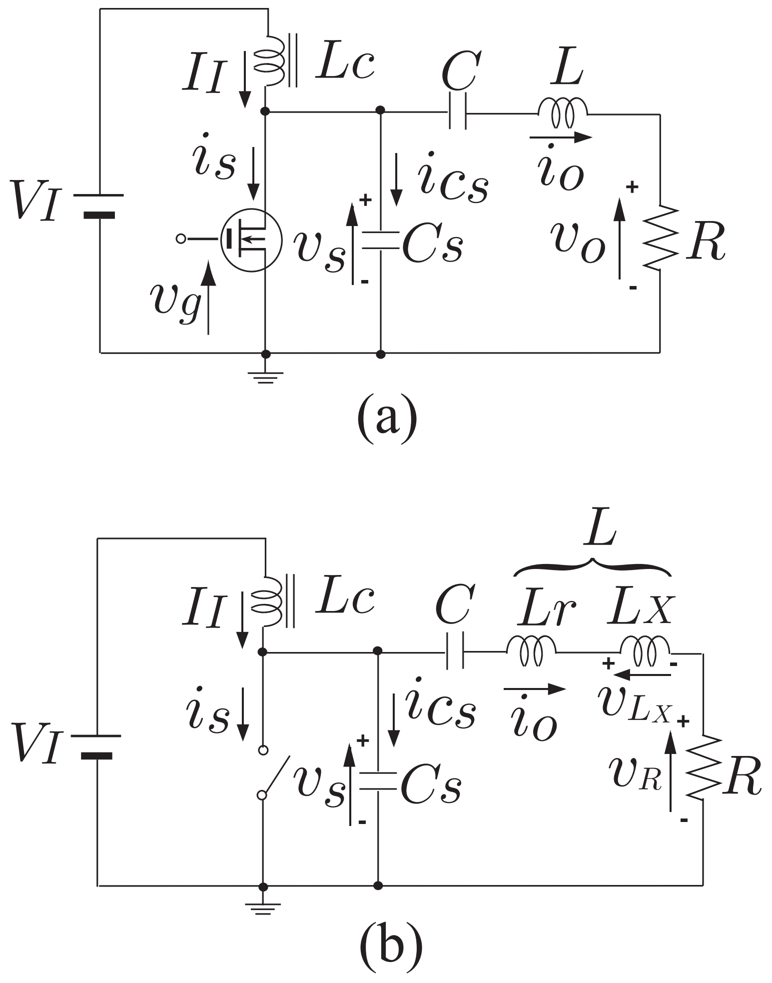

Figure 2.9: Class-E inverter. (a) Circuit topology. (b) Equivalent circuit.

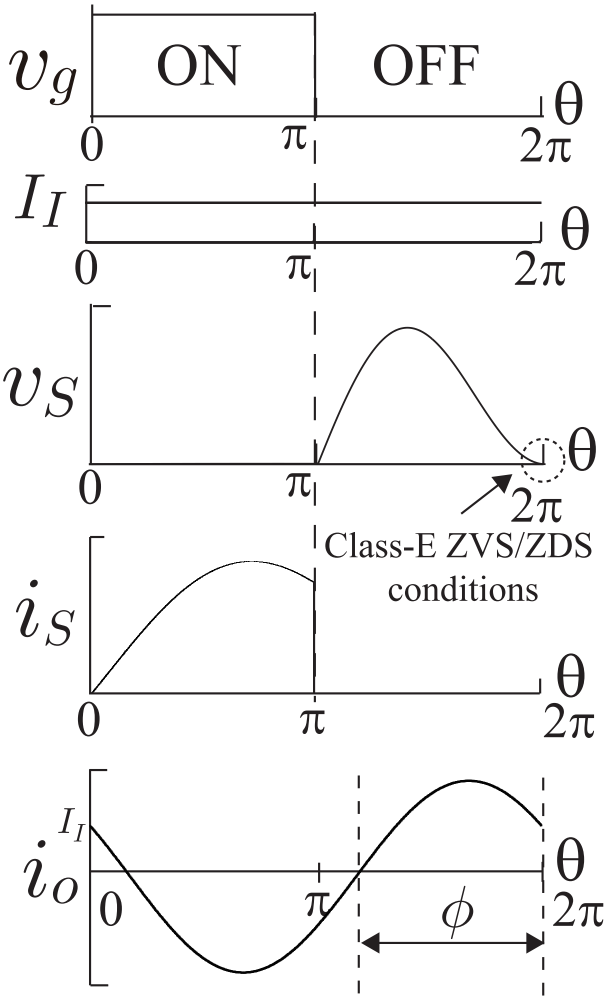

Figure 2.10: Waveforms of class-E inverter.

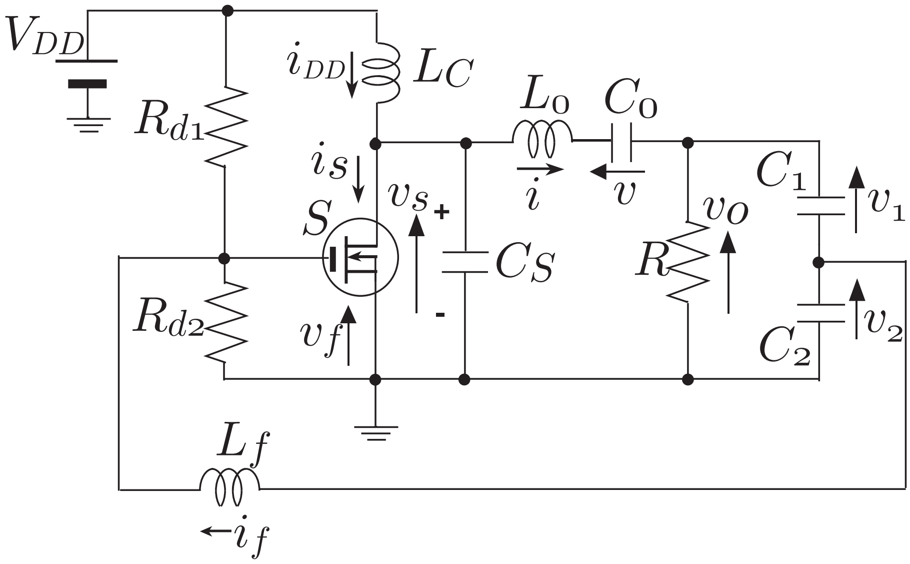

Figure 2.11: Circuit topology of class-E oscillator.

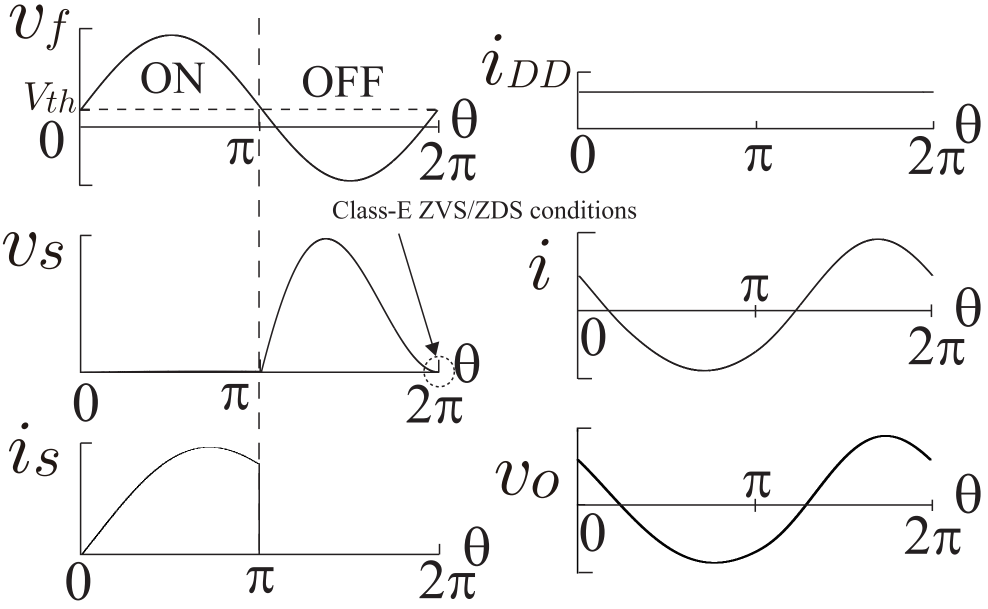

Figure 2.12: Waveforms of class-E oscillator.

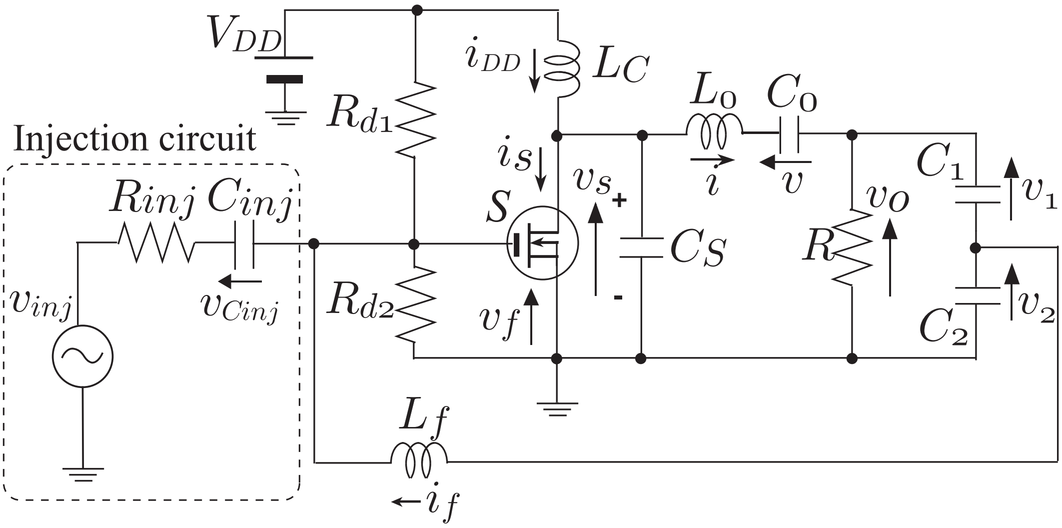

Figure 2.13: Circuit topology of injection-locked class-E oscillator.

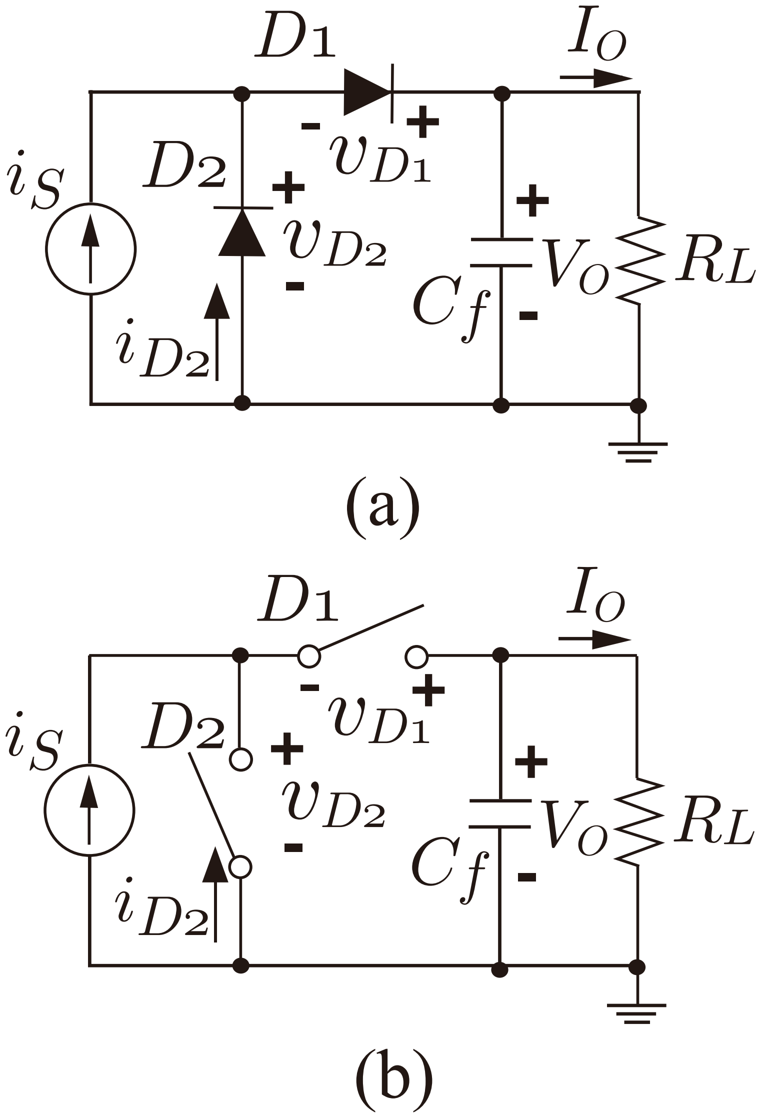

Figure 2.14: Class-D rectifier. (a) Circuit topology. (b) Equivalent circuit.

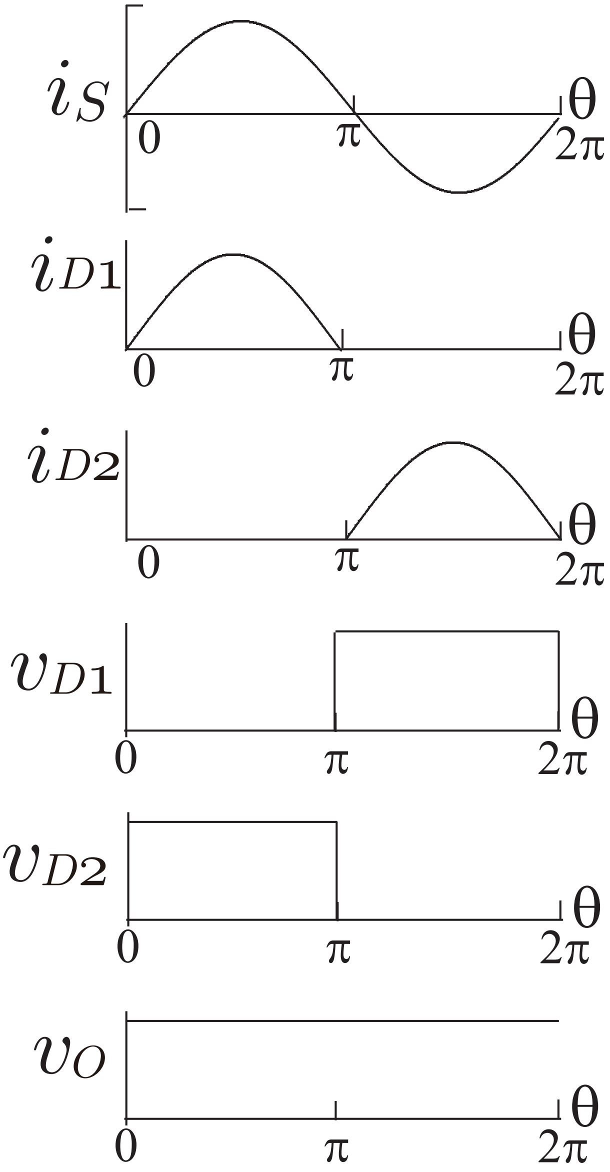

Figure 2.15: Waveforms of class-D rectifier.

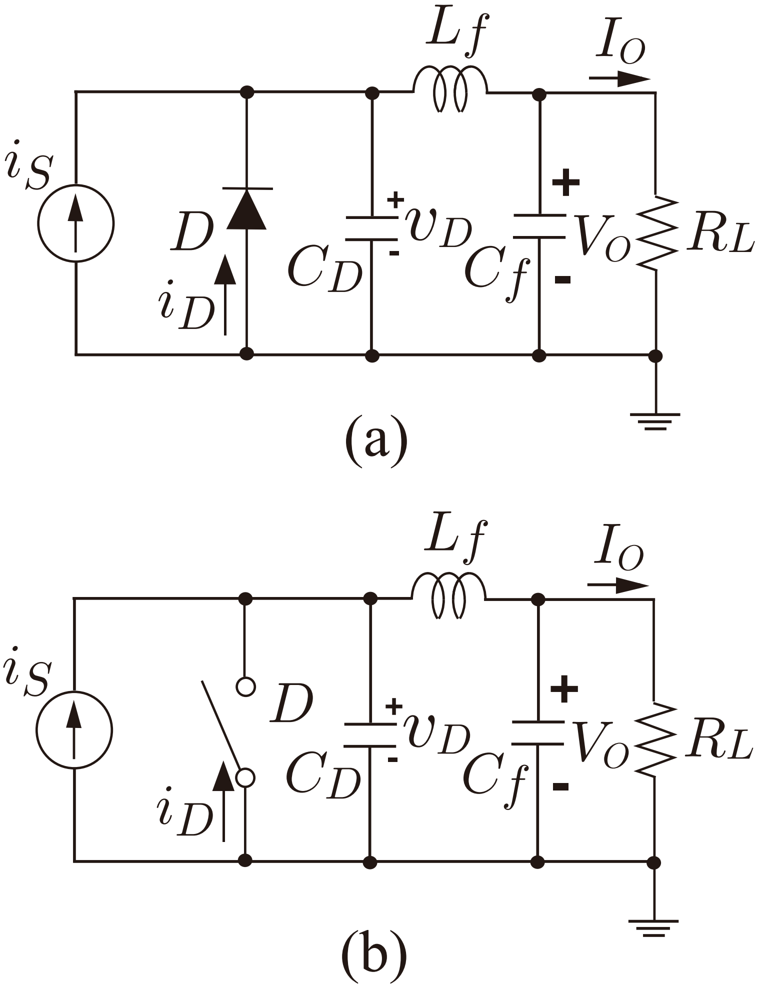

Figure 2.16: Class-E rectifier. (a) Circuit topology. (b) Equivalent circuit.

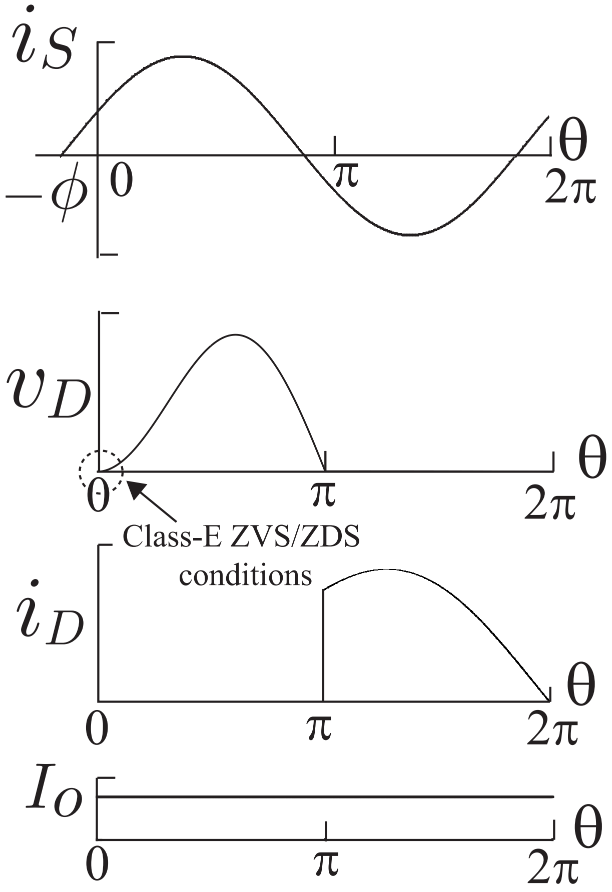

Figure 2.17: Waveforms of class-E rectifier.

Reference

[1] K. V. Schuylenbergh and R. Puers, *Inductive Powering: Basic Theory and Application to Biomedical Systems.* New York: Springer-Verlag, Jul. 2009.

[2] M. K. Kazimierczuk, *High-Frequency Magnetic Components.* New York, NY: John Wiley & Sons, 2009.

[3] M. K. Kazimierczuk, *RF Power Amplifiers.* New York, NY: John Wiley & Sons, 2008.

[4] C. Alexander and M. Sadiku, *Fundamentals of Electric Circuits.* McGraw-Hill, 2nd edition, 2003.

[5] A. Kurs, A. Karalis, R. Moffatt, J. D. Joannopoulos, P. Fisher, and M. Soljacic, "Wireless power transfer via strongly coupled magnetic resonances," *Sci. Express,* vol. 317, no. 5834, pp. 83–86, Jul. 2007.

[6] A. P. Sample, D. A. Meyer, and J. R. Smith, "Analysis, experimental results, and range adaptation of magnetically coupled resonators for wireless power transfer," *IEEE Trans. Ind. Electron.,* vol. 58, no. 2, pp. 544–554, Feb. 2011.

[7] [Online] Qi: Wireless power consortium, http://www.wirelesspowerconsortium.com, Accessed Jan. 2014.

[8] [Online] Rezence: Alliance for wireless power, http://www.rezence.com, Accessed Jan. 2014.

[9] M. K. Kazimierczuk and D. Czarkowski, *Resonant Power Converters 2nd Ed.*, New York, NY: John Wiley & Sons, 2011.

[10] P. J. Baxandall, “Transistor sine-wave LC oscillators, some general considerations and new developments,” *Proc. IEE,* vol. 106, Pt. B, suppl. 16, pp. 748-758, May 1959.

[11] M. R. Osborne, “Design of tuned transistor power inverters,” *Electron. Eng.,* vol. 40, no. 486, pp. 436-443, 1968.

[12] W. J. Chudobiak and D. F. Page, “Frequency and power limitations of Class-D transistor inverter,” *JEEEJ. Solid-State Circuits,* vol. SC-4, pp. 25-37, Feb. 1969.

[13] M. Kazimierczuk and J. S. Modzelewski, “Drive-transformerless Class-D voltage switching tuned power inverter,” *Proc. IEEE,* vol. 68, pp. 740-741, June 1980.

[14] H. L. Krauss, C. W. Bostian, and F. H. Raab, *Solid State Radio Engineering,* New York, John Wiley & Sons, 1980.

[15] M. K. Kazimierczuk and W. Szaraniec, “Class D voltage-switching inverter with only one shunt capacitor,” *IEE Proc, Pt. B, Electric Power Appl.,* vol. 139, pp. 449–456, Sept. 1992.

[16] L. R. Neorne, “Design of a 2.5-MHz, soft-switching, Class-D power amplifier,” *IEEE Trans. Power Electronics,* vol. 12, no. 3, pp. 507–516, May 1997.

[17] B.-K. Lee, B.-S. Suh, and D.-S. Hyun, “Design consideration for the improved Class-D inverter topology,” *IEEE Trans. Ind. Electron.,* vol. 45, no. 2, pp. 217–227, Apr. 1998.

[18] H. Koizumi, K. Kurokawa, and S. Mori, “Analysis of class D inverter with irregular driving patterns,” *IEEE Trans. Circuits Syst.-I,* vol. 53, no. 3, pp. 677–687, Mar. 2006.

[19] N.-J. Park, D.-Y. Lee, and D.-S. Hyun, “A power-control scheme with constant switching frequency in class-D inverter for induction-heating jar application,” *IEEE Trans. Ind. Electron.,* vol. 54, no. 3, pp. 1252–1260, Apr. 2007.

[20] N. O. Sokal and A. D. Sokal, “Class E - A new class of high-efficiency tuned single-ended switching power amplifiers,” *IEEE Jounal of Solid State Circuits*, vol. 10, no. 3, pp. 168–176, Jun. 1975.

[21] N. O. Sokal, “Class-E RF power amplifiers”, *QEX*, no. 204, pp. 9–20, Jan./Feb. 2001.

[22] F. H. Raab, “Idealized operation of the class E tuned amplifier, ” *IEEE Trans. Circuits Syst.*, vol. 24, no. 12, pp. 725–735, Dec. 1977.

[23] M. K. Kazimierczuk, “Collector amplitude modulation of the Class E tuned power amplifier,” *IEEE Trans. Circuits Syst.,* vol. CAS-31, no. 6, pp. 543–549, June 1984.

[24] G. Lüttke and H. C. Reats, “High voltage high frequency Class-E converter suitable for miniaturization,” *IEEE Trans. Power Electron.,* vol. PE-1, pp. 193–199, October 1986.

[25] F. H. Raab, P. Asbec, S. Cripps, P. B. Keningtopn, Z. B. Popovic, N. Potheary, J. Savic, and N. O. Sokal, “Power amplifiers and transistors for RF and microwaves,” *IEEE Trans. on Microwave Theory and Technique,* vol. 50, no. 3, pp. 814–826, Mar. 2002.

[26] T. Suetsugu and M. Kazimierczuk, “Off-nominal operation of class-E amplifier at any duty ratio,” *IEEE Trans. Circuits Syst.-I*, vol. 54, no. 6, pp. 1389–1397, Jun. 2007.

[27] J. Liang and W. Liao, “Steady-state simulations and optimization of class-E power amplifiers with extended impedance method,” *IEEE Trans. Circuits Syst.-I*, vol. 58, no. 6, pp. 1433–1445, Jun. 2011.

[28] M. Hayati, A. Lotfi, M. K. Kazimierczuk, and H. Sekiya, “Analysis, design and implementation of class-E ZVS power amplifier with MOSFET nonlinear drain-to-source parasitic capacitance at any grading coefficient,” *IEEE Trans. Power Electron.,* vol.29, no.9, pp.4989–4999, Sept. 2014.

[29] J. Ebert and M. Kazimierczuk, “Class E high-efficiency tuned power oscillator,” *IEEE J. Solid-State Circuits*, vol. SC-16, no. 2, pp. 62–66, Apr. 1981.

[30] D. V. Chernov, M. K. Kazimierczuk, and V. G. Krizhanovski, “Class-E MOSFET low-voltage power oscillator,” *in Proc. IEEE ISCAS*, Phoenix, AZ, vol. 5, May 2002, pp. 509–512.

[31] M. K. Kazimierczuk, V. G. Krizhanovski, J. V. Rassokhina, and D. V. Chernov, “Class-E MOSFET tuned power oscillator design procedure,” *IEEE Trans. Circuits Syst. I,* vol. 52, no. 6, pp. 1138–1147, Jun. 2005.

[32] H. Hase, H. Sekiya, J. Lu, and T. Yahagi, “Novel design procedure for MOSFET class-E oscillator,” *IEICE Trans. Fund.,* vol. E87-A, no. 9, pp. 2241–2247, Sep. 2004.

[33] H. Hase, H. Sekiya, J. Lu, and T. Yahagi, “Resonant dc/dc converter with class E oscillator,” *IEEE Trans. Circuits Syst. I,* vol. 53, no. 9, pp. 2025–2035, Sept. 2006.

[34] S. Jeon, A. Suarez, and D. B. Rutledge, “Nonlinear design technique for high-power switching-mode oscillators,” *IEEE Trans. on Microwave Theory and Technique,* vol. 54 no. 10, pp. 3630–3640, Oct. 2006.

[35] T. Andersen, S. K. Christensen, A. Knott, and M. A. E. Andersen, "A VHF class E DC-DC converter with self-oscillating gate driver," *in Proc. IEEE APEC,* Fort Worth, TX, Mar. 2011, pp. 885–891.

[36] M. K. Kazimierczuk, V. G. Krizhanovski, J. V. Rassokhina, and D. V. Chernov,"Injection-locked class-E oscillator," *IEEE Trans. Circuits Syst. I,* vol. 53, no. 6, pp. 1214–1222, Jun. 2006.

[37] R. A. Adler, "Study of locking phenomena in oscillators, " in *Proc. IRE,* Jun. 1946, vol. 34, no. 6, pp. 351–357.

[38] A. Mirzaei, M. E. Heidari, R. Bagheri, S. Chehrazi, and A. A. Abidi, "The quadrature LC oscillator: a complete portrait based on injection locking," *IEEE J. Solid-State Circuits,* vol. 42, no. 9, pp. 1916–1932, Sept. 2007.

[39] P. Maffezzoni, "Analysis of oscillator injection locking through phase-domain impulse-response," *IEEE Trans. Circuits Syst. I*, vol. 55, no. 5, pp. 1297–1305, Jun. 2008.

[40] C. T. Chen, T. S. Horng, K. C. Peng, and C. J. Li, "High-gain and high-efficiency EER/Polar transmitters using injection-locked oscillators," *IEEE Trans. Microw. Theory Tech.,* vol. 60, no. 12, pp. 4117–4128, Dec. 2012.

[41] P. Bhansali and J. Roychowdhury, "Gen-Adler: The generalized Adler's equation for injection locking analysis in oscillators," *in Proc. ASP-DAC,* Yokohama, Japan, Jan. 2009, pp. 522–527.

[42] M. Mikotajewski, "Class D synchronous rectifiers," *IEEE Trans. Circuits Syst. I,*, no. 38, vol. 7, pp. 694–697, Jul. 1991.

[43] M.K. Kazimierczuk, "Class D current-driven rectifiers for resonant DC/DC converter applications," *IEEE Trans. Ind. Electron.,* no. 38, vol. 5, pp. 344–354, Oct. 1991.

[44] A. Reatti and M.K. Kazimierczuk, "Comparison of the efficiencies of Class D and Class E rectifiers," *In Proc, MWSCAS,* Aug. 1993, pp. 871–874 .

[45] M. K. Kazimierczuk, "Analysis of class E zero-voltage switching rectifier," *IEEE Trans Circuit Syst.,* vol. 37, no. 6, pp. 747–755, Jun. 1990.

[46] K. Fukui and H. Koizumi, "Class E rectifier with controlled shunt capacitor," *IEEE Trans. Power Electron.,* vol. 27, no. 8, pp. 3704–3713, Aug. 2012.

[47] Y. Kamito, K. Fukui, and H. Koizumi, "An analysis of the class-E zero-voltage-switching rectifier using the common-grounded multistep-controlled shunt capacitor," *IEEE Trans. Power Electron.,* vol. 29, no. 9, pp. 4807–4816, Sept. 2014.

[48] S. Aldhaher, P. Luk, K. Drissi, and J. Whidborne, "High input voltage high frequency class E rectifiers for resonant inductive links," *IEEE Trans. Power Electron.,* vol. 30, no. 3, pp. 1328–1335, Mar. 2015.

[49] P. Luk, S. Aldhaher, W. Fei, and J. Whidborne, "State-space modelling of a class E^2 converter for inductive links," *IEEE Trans. Power Electron.,* to be published.

Chapter 3

Waveform Equations, Output Power, and Power Conversion Efficiency for Class-E Inverter Outside Nominal Operation

●● ABSTRACT ●●

This chapter presents analytical expressions for steady-state waveforms, output power, and power conversion efficiency for the class-E inverter outside the class-E ZVS/ZDS conditions. The analytical expressions in this chapter include the MOSFET-body-diode effect. By carrying out PSpice simulations and circuit experiments, it is shown that the analytical predictions agreed with the simulated and the experimental results quantitatively, which indicates the validity of the analytical expressions. Additionally, the switching-pattern distribution maps are also given by using the analytical waveform equations.

3.1 Introduction

In recent years, the resonant class-D [1], -DE [2], and -E [3]-[22] inverters are widely used in various applications. The class-E inverter is a well-known resonant inverter that can operate with high power-conversion efficiency at high frequencies. Since the introduction of the class-E inverter [3], many analytical descriptions of this circuit have appeared. Additionally, many applications of the class-E inverter, such as dc-dc converter [4], inverter with impedance inverter [5], lamp ballast [6], high-power-factor inverter [7], wireless power transfer system [8], and so on, were proposed. These applications are transformed into the basic class-E inverter topology for their designs. Therefore, it can be stated that the analytical expressions in the class-E inverter are very useful and applicable for many applications of not only the class-E inverter but also other topologies of the class-E switching circuits. Most of these studies focused on the class-E switching circuits satisfying the class-E zero-voltage switching and zero-derivative switching (ZVS/ZDS) conditions, which are called "nominal conditions". When considering the class-E inverter applications, however, it is important to obtain the analytical expressions of waveforms, output power, and power conversion efficiency outside nominal operation. For example, the inductive component of coupled coil pair varies drastically by changing the distance between primary coil and secondary one in wireless power transfer applications [8]. The PWM-control class-E inverter [9] works at any duty ratio, which means the outside nominal conditions. Additionally, the off-nominal-operation class-E inverter [10], [11] also works outside the nominal conditions.

Actually, analyses of the class-E inverter outside nominal operations were carried out recently. These analyses are classified into two approaches. One is a frequency-domain analysis [12]-[14] and the other is a time-domain one [15]-[17]. In [12], the frequency-domain analysis of the class-E inverter outside nominal operations was presented. Because of the frequency-domain analysis, however, the switching pattern should be fixed prior to calculations. Therefore, effects of the MOSFET body diode cannot be considered because the MOSFET body diode turns on and off autonomously. In [15]-[17], the time-domain analyses of the class-E inverter outside nominal operations were presented. In [16] and [17], turn-on effect of the MOSFET body diode on the waveform equations is considered. However, the switch-voltage recovery during the on-state of the MOSFET body diode is not considered.

In [18], an adjusting method of the load network for achieving the class-E ZVS/ZDS conditions is introduced. This method is very useful for designs of the class-E inverters. In [18], the switch-voltage recovery during on-state of the MOSFET body diode is illustrated, which indicates the importance of the MOSFET body diode effect in the class-E inverter operation. In the previous studies, however, there is no analytical expression including the switch-voltage recovery. For comprehending the operation of the class-E inverter in a wide region of parameters, it is important to consider the MOSFET body diode effect completely, namely not only its turn-on but -off, in the analysis.

There is an idea that the behavior of class-E inverter outside nominal operation can be comprehended by using circuit simulators. In the class-E inverter, however, it takes a long time to converge the dc-supply current, which flows through the RF choke, in transient analysis because the time constant of the RF choke is high. Generally, inverters with high Q resonant filter also have a long transient-response time. Therefore, it leads to a high calculation cost for obtaining the steady-state waveforms of the class-E inverter by using the circuit simulators. In addition, circuit simulators give waveforms at a fixed set of parameters. It is hard to comprehend the circuit-behavior according to any parameter variations by using circuit simulators. For these reasons, it is useful for designers to obtain the analytical expressions of steady-state waveforms outside nominal operations. Additionally, an analysis has many advantages compared with the simulation. Analytical expressions cultivate designer's fundamental understanding and intuition. By using the analytical expressions, much additional information can be obtained easily.

This chapter presents analytical expressions for steady-state waveforms, output power, and power conversion efficiency of the class-E inverter outside the class-E ZVS/ZDS conditions at a high Q and any duty ratio, taking into account MOSFET-body-diode effect. By considering the switch-voltage recovery during the MOSFET body diode on-state, the applicable parameter range of the analytical expressions in this chapter is much wider than that of the previous analytical expressions. The analytical expressions in this chapter cover all the results of [15]-[17]. By carrying out the PSpice simulations and the circuit experiments, it is shown that the analytical predictions agreed with the simulated and the experimental results quantitatively, which validates accuracy of our analytical expressions. Additionally, the switching-pattern distribution maps are also shown, which can be obtained from the waveform equations.

3.2 Circuit Description and Principle Operation

Figure 3.1(a) shows a circuit topology of the class-E inverter. It is composed of dc-supply voltage source V_{DD}, dc-feed inductance L_C, MOSFET as a switching device S, shunt capacitance C_S, and series-resonant filter L_0-C_0-R. The class-E inverter achieves high-power conversion efficiency at high frequencies because it satisfies the zero-voltage switching and the zero-derivative switching (ZVS/ZDS) conditions simultaneously at the switch turn-on instant. Switching loss is minimized because of the ZVS and jump-less currents at turn-on instant. The class-E ZVS/ZDS conditions are expressed as

$$\begin{bmatrix} v_S(2\pi D) \\ \left.\dfrac{dv_S(\theta)}{d\theta}\right|_{\theta=2\pi D} \end{bmatrix} = \mathbf{0}, \tag{3.1}$$

where v_S is the voltage across the switching device S and D is the switch-off duty ratio at the switch. In real circuits, there are the equivalent series resistances (ESRs) of the passive elements and the MOSFET switch on-resistance. Because the power-loss factors in the class-E inverter include conduction losses in the ESRs and the switch on-resistance, the conditions for obtaining the maximum power conversion efficiency are not the same as those for the class-E ZVS/ZDS conditions. Therefore, the class-E ZVS/ZDS conditions are called "nominal conditions" and the conditions for obtaining the maximum power-conversion efficiency are called "optimal conditions" [18].

Figure 3.2 depicts example waveforms in the class-E inverter at nominal operation for $D = 0.5$. In the class-E inverter, the switch S is driven by a input signal v_g. During the switch-off interval, the difference of currents through the dc-feed inductance and the resonant filter flows through the shunt capacitance C_S. The current through the shunt capacitance produces the switch voltage v_S. Because the class-E inverter usually has a resonant filter with high quality factor Q, the output current i_o is regarded as a sinusoidal waveform. Additionally, the output filter produces a phase-shift ϕ between the input signal and the output current as shown in Fig. 3.2.

3.3 Waveform Equations Outside Nominal Conditions

The analytical steady-state waveform equations for the class-E inverter outside nominal conditions are given in this section. Note that all the equations in [17] are renewed as new ones.

3.3.1 Switching Patterns

Figure 3.3 shows the switch voltage and current waveforms of the class-E inverter outside nominal operation. We classify the switching patterns into three cases as shown in Fig. 3.3. Figure 3.3(a) shows that the switch voltage does not reach zero during switch-off interval. This switching pattern is called “Case 1” in this research. In this case, the turn-on switching loss occurs at turn-on instant. When the switch voltage reaches zero prior to turn-on switching instant, the MOSFET anti-parallel body diode turns on at $\theta = \theta_1$ as shown in Fig. 3.3(b), where $\theta = \omega t$ represents the angular time. This switching pattern is called “Case 2”, in which the ZVS is achieved at $\theta = 2\pi D$. The on-resistance of the MOSFET body diode is, however, much larger than that of the MOSFET. Therefore, the large conduction loss occurs in this case. There is also a case that the switch voltage returns to a positive at $\theta = \theta_2$ via MOSFET-body-diode on state as shown in Fig. 3.3(c), which is called “Case 3”. In this case, both the turn-on switching loss and the conduction loss in the MOSFET body diode occur. The switching patterns are closely related to the amplitude and the phase shift of the output current because the switch voltage is expressed as the integration of the difference of the dc-supply current and output current. Therefore, if the inverter parameters, such as load resistance, resonant capacitance and inductance, switch-off duty ratio, and so on, vary from the nominal conditions, the amplitude and the phase shift of the output current also vary and the change of the switching pattern occurs. The relationship between the switch waveform and output-filter parameters are shown in [18]. It can be stated from [18] that it is not easy to predict which switching pattern appears for a certain set of parameters.

In the previous studies, the steady-state waveform equations in [12] and [15] are valid for only Case 1. The steady-state waveform equations in Cases 1 and 2 are given in [16] and [17]. There is, however, no analytical steady-state waveform equations, which are valid for Cases 1, 2, and 3.

3.3.2 Assumptions and Parameters

First, the following parameters are defined:

(1) $A = f_0/f = \omega_0/\omega = 1/\omega\sqrt{L_0C_0}$: The ratio of the resonant frequency to the operating frequency.

(2) $B = C_0/C_S$: The ratio of the resonant capacitance to the shunt capacitance.

(3) D: The switch-off duty ratio of the switch S.

(4) $Q = \omega L_0/R$: The loaded Q-factor.

For obtaining the waveform equations, the analysis is based on the following assumptions for simplification:

(a) The MOSFET works as an ideal switch device, namely, it has zero on-resistance, infinite off-resistance and zero switching time.

(b) The MOSFET body diode also works as an ideal switch device. Therefore, it has zero forward voltage drop, infinite off-resistance, and zero switching time.

(c) The dc-feed inductance L_C is high enough so that the current through the dc-feed inductor is constant.

(d) The loaded Q-factor is high enough to generate a pure sinusoidal output current i_o for any parameters.

(e) All the passive elements are linear and have zero ESR.

(f) The circuit operations are considered in the interval $0 \leq \theta < 2\pi$. The switch is in the off-state for $0 \leq \theta < 2\pi D$ and in the on-state for $2\pi D \leq \theta < 2\pi$.

(g) The MOSFET body diode turns on at $\theta = \theta_1$ and turns off at $\theta = \theta_2$ for $0 < \theta_1 \leq \theta_2 < 2\pi D$. When θ_1 and/or θ_2 does not appear during switch-off interval, this analysis gives $\theta_1 = 2\pi D$ and/or $\theta_2 = 2\pi D$, respectively.

(h) The parasitic capacitances of the inductors are ignored.

By the above assumptions, the equivalent circuit is obtained as shown in Fig. 3.1(b).

3.3.3 Waveform Equations

This subsection introduces only the resulting equations and the detailed analysis procedure is shown in the Appendix. Additionally, the classifications of the switching patterns and the derivations of θ_1 and θ_2 are discussed in Section 3.4. From the assumption (d), the output current is

$$i_o = I_m \sin(\theta + \phi). \tag{3.2}$$

In (3.2), I_m is the amplitude of the output current

$$I_m = \frac{2\pi\beta V_{DD}}{A^2 BQR(\alpha\delta + \gamma\beta)}, \tag{3.3}$$

where

$$\alpha = k_1 \cos^2\phi + k_2 \sin\phi\cos\phi + k_3, \tag{3.4}$$

$$\beta = k_4 \cos\phi + k_5 \sin\phi, \tag{3.5}$$

$$\gamma = k_6 \cos\phi + k_7 \sin\phi, \tag{3.6}$$

and

$$\delta = \frac{1}{2}\theta_1^2 + \frac{1}{2}\theta_2^2 + 2\pi^2 D^2 - 2\pi D\theta_2. \tag{3.7}$$

In addition, the coefficients k in (3.4)–(3.7) are

$$\begin{aligned} k_1 = &\frac{1}{2}\cos(2\theta_1) - \cos\theta_1 + \frac{1}{2}\cos(4\pi D) + \frac{1}{2}\cos(2\theta_2) + \frac{1}{2} \\ &- \cos\theta_2\cos(2\pi D) + \sin\theta_2\sin(2\pi D), \end{aligned} \tag{3.8}$$

$$\begin{aligned} k_2 = &-\frac{1}{2}\sin(2\theta_1) + \sin\theta_1 - \frac{1}{2}\sin(4\pi D) - \frac{1}{2}\sin(2\theta_2) \\ &+ \sin\theta_2\cos(2\pi D) + \cos\theta_2\sin(2\pi D), \end{aligned} \tag{3.9}$$

$$\begin{aligned} k_3 = &-\frac{1}{4}\cos(2\theta_1) - \frac{1}{4}\cos(4\pi D) - \frac{1}{4}\cos(2\theta_2) + \frac{\pi}{A^2BQ} + \frac{3}{4} \\ &- \sin\theta_2\sin(2\pi D), \end{aligned} \tag{3.10}$$

$$\begin{aligned} k_4 = &-\theta_1\cos\theta_1 + \sin\theta_1 + (\theta_2 - 2\pi D)\cos(2\pi D) \\ &+ \sin(2\pi D) - \sin\theta_2, \end{aligned} \tag{3.11}$$

$$\begin{aligned} k_5 = &\,\theta_1\sin\theta_1 + \cos\theta_1 + (2\pi D - \theta_2)\sin(2\pi D) \\ &+ \cos(2\pi D) - \cos\theta_2 - 1, \end{aligned} \tag{3.12}$$

$$k_6 = \sin\theta_1 + \sin(2\pi D) - \sin\theta_2 + (\theta_2 - 2\pi D)\cos\theta_2 - \theta_1, \tag{3.13}$$

and

$$k_7 = \cos\theta_1 + \cos(2\pi D) + (2\pi D - \theta_2)\sin\theta_2 - \cos\theta_2 - 1. \tag{3.14}$$

Additionally, the phase shift ϕ is obtained by solving an algebraic equation for $\tan\phi$,

$$\begin{aligned} &(k_4k_3 + k_5k_{10})\tan^3\phi + (k_2k_4 + k_3k_9 - k_3k_5 + k_4k_{10})\tan^2\phi \\ &+(k_1k_4 - k_2k_5 + k_4k_9 + k_5k_8 + k_3k_4 + k_5k_{10})\tan\phi \\ &+(k_4k_8 - k_1k_5 - k_3k_5 + k_4k_{10}) = 0, \end{aligned} \tag{3.15}$$

where

$$k_8 = -\frac{1}{2}\sin(2\theta_1) + \sin\theta_1 - \frac{1}{2}\sin(4\pi D) - \sin(2\theta_2) \\ + \cos\theta_2\sin(2\pi D) + \sin\theta_2\cos(2\pi D), \tag{3.16}$$

$$k_9 = \frac{1}{2}\cos(2\theta_2) - \frac{1}{2}\cos(2\theta_1) + \cos\theta_1 - \frac{1}{2}\cos(4\pi D) - \frac{1}{2} \\ + \cos\theta_2\cos(2\pi D) - \sin\theta_2\sin(2\pi D) - \cos^2\theta_2 + \sin^2\theta_2, \tag{3.17}$$

and

$$k_{10} = -\frac{\theta_1}{2} + \frac{\theta_2}{2} + \frac{1}{4}\sin(2\theta_2) + \frac{1}{4}\sin(4\pi D) - \frac{1}{4}\sin(2\theta_2) - \pi D \\ - \sin\theta_2\cos(2\pi D) + \sin\theta_2\cos\theta_2 + \frac{(1-A^2)\pi}{A^2B}. \tag{3.18}$$

The switch voltage is expressed as

$$vs = \\ \begin{cases} v_{S1} = A^2BQR\{I_{DD}\theta + I_m[\cos(\theta+\phi) - \cos\phi]\}, \text{ for } 0 \le \theta < \theta_1 \\ v_{S2} = 0, \quad \text{for } \theta_1 \le \theta < \theta_2, \\ v_{S3} = A^2BQR\{I_{DD}(\theta-\theta_2) \\ \qquad + I_m[\cos(\theta+\phi) - \cos(\theta_2+\phi)]\}, \text{ for } \theta_2 \le \theta < 2\pi D, \\ v_{S4} = 0, \quad \text{for } 2\pi D \le \theta < 2\pi, \end{cases} \tag{3.19}$$

where I_{DD} is the dc component of the current through the dc-feed inductor, which is given by

$$I_{DD} = \frac{2\pi\alpha V_{DD}}{A^2BQR(\alpha\delta + \gamma\beta)}. \tag{3.20}$$

The current through the shunt capacitance is

$$i_{C_S} = \begin{cases} i_{C_{S1}} = I_{DD} - I_m \sin(\theta + \phi), & \text{for } 0 \leq \theta < \theta_1 \\ i_{C_{S2}} = 0, & \text{for } \theta_1 \leq \theta < \theta_2 \\ i_{C_{S3}} = I_{DD} - I_m \sin(\theta + \phi), & \text{for } \theta_2 \leq \theta < 2\pi D \\ i_{C_{S4}} = 0, & \text{for } 2\pi D \leq \theta < 2\pi. \end{cases} \tag{3.21}$$

The current through the switch is

$$i_S = \begin{cases} i_{S1} = 0, & \text{for } 0 \leq \theta < \theta_1 \\ i_{S2} = I_{DD} - I_m \sin(\theta + \phi), & \text{for } \theta_1 \leq \theta < \theta_2 \\ i_{S3} = 0, & \text{for } \theta_2 \leq \theta < 2\pi D \\ i_{S4} = I_{DD} - I_m \sin(\theta + \phi), & \text{for } 2\pi D \leq \theta < 2\pi, \end{cases} \tag{3.22}$$

where i_{S2} describes the current through the MOSFET body diode.

Note that the equations for $\theta_1 = \theta_2 = 2\pi D$ are the same as those given in [15]. Additionally, the equations for only $\theta_2 = 2\pi D$ is the same as those in [16] and [17]. The analytical steady-state waveform equations in this chapter cover with all the results of [15]-[17].

3.4 Derivations of θ_1 and θ_2

The waveform equations given in Section 3.3 are valid for all the switching patterns in Cases 1, 2, and 3. For obtaining the waveforms, however, θ_1 and θ_2 should be determined. This section introduces an algorithm for obtaining the values of θ_1 and θ_2. Figure 3.4 shows the flowchart for obtaining θ_1 and θ_2.

First, the waveforms for $\theta_1 = \theta_2 = 2\pi D$ are considered. After substituting $\theta_1 = \theta_2 = 2\pi D$ into (3.19), we calculate the phase shift from (3.15) and the switch voltage with zero derivative. θ_a is defined as the instant when the zero-derivative switch voltage appears. Therefore, we have

$$\left.\frac{dv_{S1}}{d\theta}\right|_{\theta=\theta_a} = \frac{1}{\omega C_S} i_{C_S}(\theta_a) = 0, \quad \text{for } 0 < \theta_a \leq 2\pi D. \tag{3.23}$$

The solution of (3.23) can be obtained analytically as

$$\theta_a = \sin^{-1}\left(\frac{I_{DD}}{I_m}\right) - \phi, \quad \text{for } 0 < \theta_a \leq 2\pi D. \tag{3.24}$$

When there is no solution of θ_a or

$$v_{S1}(\theta_a) > 0 \ \text{ for all } \theta_a, \tag{3.25}$$

the switching pattern is classified as Case 1 and $\theta_1 = \theta_2 = 2\pi D$ can be obtained.

When the switching pattern is not for Case 1, only $\theta_2 = 2\pi D$ is substituted into (3.19). Additionally, the angular time for the zero-switch-voltage appearance is calculated from

$$v_{S1}(\theta_b) = 0. \tag{3.26}$$

This equation is solved numerically. The Newton's method is applied to solve the algebraic equation numerically in this study. When the current through the MOSFET body-diode satisfies

$$i_{S2}(2\pi D) \leq 0, \tag{3.27}$$

the switching pattern is classified as Case 2 and $\theta_1 = \theta_b$ and $\theta_2 = 2\pi D$ are obtained.

When the switching pattern belongs to neither Case 1 nor 2, it is classified as Case 3. In Case 3, θ_1 and θ_2 are obtained by solving

$$\begin{bmatrix} v_{S1}(\theta_1) \\ i_S(\theta_2) \end{bmatrix} = \mathbf{0}. \tag{3.28}$$

This function is also solved by the Newton's method because this is a transcendental function. Following this algorithm, it is possible to obtain the values of θ_1 and θ_2 and to comprehend the switching pattern for given parameters, simultaneously.

3.5 Output Power and Power Conversion Efficiency

In this section, analytical expressions for the output power and the power-conversion efficiency are derived by using the waveform equations given in Section III. In real circuits, the power losses occur in ESRs of passive elements, MOSFET on-resistance, and MOSFET body diode. It is assumed that the parasitic resistances and MOSFET-body-diode forward voltage drop are small enough not to affect the waveforms [2], [16], [17]. Figure 3.5 shows the equivalent circuit model of the class-E inverter for the power-loss calculations. In this chapter, the power losses in MOSFET on-resistance r_S; ESRs of dc-feed inductance r_{L_C}, shunt capacitance r_{C_S}, and resonant network $r_{L_0C_0}$; and MOSFET-body-diode are considered.

The output power P_o is

$$P_o = \frac{R}{2\pi}\int_0^{2\pi} i_o^2 d\theta = \frac{RI_m^2}{2}. \tag{3.29}$$

The conduction loss in the MOSFET on-resistance r_S is

$$\begin{aligned}P_S &= \frac{r_S}{2\pi}\int_0^{2\pi} i_S^2 d\theta = \frac{r_S}{2\pi}\int_{2\pi D}^{2\pi} i_S^2 d\theta \\ &= \frac{r_S}{2\pi}\Bigg\{2\pi(1-D)I_{DD}^2 + 2I_{DD}I_m[\cos\phi - \cos(2\pi D+\phi)] \\ &\quad + \frac{I_m^2}{4}\left[4\pi(1-D) + \sin(4\pi D + 2\phi) - \sin 2\phi\right]\Bigg\}.\end{aligned} \tag{3.30}$$

The power loss in r_{L_C} is

$$P_{L_C} = r_{L_C} I_{DD}^2. \tag{3.31}$$

The power loss in r_{C_S} is

$$\begin{aligned}P_{C_S} &= \frac{r_{C_S}}{2\pi}\int_0^{2\pi} i_{C_S}^2 d\theta = \frac{r_{C_S}}{2\pi}\left[\int_0^{\theta_1} i_{C_S}^2 d\theta + \int_{\theta_2}^{2\pi D} i_{C_S}^2 d\theta\right]\\ &= \frac{r_{C_S}}{2\pi}\Bigg\{ I_{DD}^2(\theta_1-\theta_2+2\pi D) + 2I_{DD}I_m[\cos(\theta_1+\phi)\\ &\quad -\cos\phi+\cos(2\pi D+\phi)-\cos(\theta_2+\phi)]\\ &\quad +\frac{I_m^2}{4}\Bigg[2\theta_1-2\theta_2+4\pi D-\sin(2\theta_1+2\phi)\\ &\quad -\sin(4\pi D+2\phi)+\sin(2\theta_2+2\phi)\Bigg]\Bigg\}.\end{aligned} \tag{3.32}$$

The power loss in $r_{L_0C_0}$ is

$$P_{L_0C_0} = \frac{r_{L_0C_0}}{2\pi}\int_0^{2\pi} i_o^2 d\theta = \frac{r_{L_0C_0}I_m^2}{2}. \tag{3.33}$$

Additionally, power losses in the MOSFET should be considered. In Cases 1 and 3, the turn-on switching losses occur, which is expressed as

$$\begin{aligned}P_{sw} &= \frac{1}{2}C_S f v_S^2(2\pi D^-) = \frac{1}{2}C_S f[v_{S1}^2(\theta_1^-)+v_{S3}^2(2\pi D^-)]\\ &= \frac{A^2BQR}{4\pi}\Big\langle \theta_1^2 I_{DD}^2 + 2\theta_1 I_{DD}I_m[\cos(\theta_1+\phi)-\cos\phi]\\ &\quad +I_m^2[\cos(\theta_1+\phi)-\cos\phi]^2+(2\pi D-\theta_2)^2 I_{DD}^2\\ &\quad +2I_mI_{DD}\{(2\pi D-\theta_2)[\cos(2\pi D+\phi)-\cos(\theta_2+\phi)]\}\\ &\quad +I_m^2[\cos(2\pi D+\phi)-\cos(\theta_2+\phi)]^2\Big\rangle\end{aligned} \tag{3.34}$$

where $v_{S1}(\theta_1^-)$ and $v_{S3}(2\pi D^-)$ is the switch voltage just prior to turn-on. It can be confirmed that $P_{SW}=0$ for $\theta_1 \neq 2\pi D$ and $\theta_2 = 2\pi D$, which are Case-2 switching pattern conditions, because of $v_{S1}(\theta_1)=0$. Conversely, P_{SW} is not equal to zero for $\theta \neq 2\pi D$. Namely, (3.34) can expresses the switching loss of all the switching patterns. In the Case-2 and Case-3 switching patterns, the MOSFET body diode turns on and the conduction loss in the MOSFET body diode should be considered. The MOSFET-body-diode conduction loss is

$$\begin{aligned} P_D &= \frac{1}{2\pi}\int_0^{2\pi} V_d i_S d\theta = \frac{1}{2\pi}\int_{\theta_1}^{\theta_2} V_d i_S d\theta \\ &= \frac{V_d}{2\pi}\Big\{ I_{DD}(\theta_2-\theta_1) + I_m[\cos(\theta_2+\phi) - \cos(\theta_1+\phi)]\Big\}, \end{aligned} \tag{3.35}$$

where V_d is the forward voltage drop of the MOSFET body diode. It can be confirmed from (3.35) that $P_D = 0$ for $\theta_1 = \theta_2 = 2\pi D$. From the above considerations, the total power loss of the class-E inverter is

$$P_{total} = P_S + P_{C_S} + P_{L_C} + P_{L_0C_0} + P_D + P_{sw}. \tag{3.36}$$

From (3.3), (3.20), (3.29) and (3.36), the power-conversion efficiency can be obtained analytically as

$$\begin{aligned} \eta &= \frac{P_o}{P_o + P_{total}} \qquad\qquad (3.37) \\ &= 4\pi R \Big/ \Big\langle 2\left(\frac{\alpha}{\beta}\right)^2 \Big[4\pi r_S(1-D) + 4\pi r_{L_C} + 2r_{C_S}(\theta_1 - \theta_2 + 2\pi D) \\ &+ A^2BQR(2\pi D - \theta_2)^2 + \theta_1^2 \Big] + 4\left(\frac{\alpha}{\beta}\right)\Big\{ 2r_S[\cos\phi - \cos(2\pi D + \phi)] \\ &+ 2r_{C_S}[\cos(\theta_1+\phi) - \cos\phi + \cos(2\pi D + \phi) - \cos(\theta_2+\phi)] \\ &+ A^2BQR\theta_1\big[\cos(\theta_1+\phi) - \cos\phi\big] \\ &+ A^2BQR(2\pi D - \theta_2)\big[\cos(2\pi D+\phi) - \cos(\theta_2+\phi)\big]\Big\} \\ &+ 4\pi R + 4\pi r_{L_0C_0} + r_S[4\pi(1-D) + \sin(4\pi D + 2\phi) - \sin 2\phi] \\ &+ r_{C_S}[2\theta_1 - 2\theta_2 + 4\pi D - \sin(2\theta_1 + 2\phi) - \sin(4\pi D + 2\phi) \\ &+ \sin(2\theta_2 + 2\phi) - \sin 2\phi] + 2A^2BQR\{[\cos(\theta_1+\phi) - \cos\phi]^2 \\ &+ [\cos(2\pi D + \phi) - \cos(\theta_2+\phi)]^2\} \\ &+ \frac{A^2BQR(\alpha\delta + \gamma\beta)}{\pi\beta V_{DD}}\Big[\cos(\theta_2+\phi) - \cos(\theta_1+\phi) + \frac{\alpha}{\beta}(\theta_2-\theta_1)\Big]\Big\rangle. \end{aligned}$$

Note that this power-conversion-efficiency expression is valid for all the switching patterns.

3.6 Experimental Verification

3.6.1 Nominal State

For validating the analytical expressions, PSpice simulations and circuit experiments were carried out. The design specifications for nominal operation were given as follows: operating frequency $f_{nom} = 1$ MHz, dc-supply voltage $V_{DD} = 5$ V, output resistance R_{nom} $= 5\ \Omega$, switch-off duty ratio $D = 0.5$, and loaded quality factor $Q = 10$. First, the design of the class-E inverter with the nominal conditions in (3.1) for $\theta_1 = \theta_2 = 2\pi D$ is carried out. By using design equations in [19], $A = 0.94$, and $B = 0.62$ are obtained. From these values, the element values are obtained as $L_C = 34.67\ \mu$H, $L_0 = 7.96\ \mu$H, $C_S = 5.84$ nF, and C_0 $= 3.60$ nF. An IRF530 MOSFET device was used in the circuit experiment. Therefore, $r_S = 0.16\ \Omega$ and $V_d = 0.7$ V were obtained from the IRF530 MOSFET data sheet. All element values including ESR values were measured by HP4284A LCR impedance meter. In experimental circuits, the shunt capacitance was composed of the MOSFET drain-to-source capacitance and external capacitance connected in parallel. The IRF530 MOSFET drain-to-source capacitance was estimated as 500 pF, which is also obtained from the data sheet. The analytical predictions and experimental measurements for satisfying the class-E ZVS/ZDS conditions were given in Table 3.1. In the PSpice simulations, the element values and the ESR ones are same as the analytical predictions and the experimental measurements, respectively. In Table 3.1 in [17], the output power was obtained from

$$P_o = \frac{V_o^2}{R}, \tag{3.38}$$

where V_o is a root-mean-square value of the output voltage, which was measured by Agilent 3458A. In addition, the power conversion efficiency was measured by

$$\eta = \frac{P_o}{P_I} = \frac{V_o^2}{RV_{DD}I_{DD}}, \tag{3.39}$$

where P_I is the dc-supply power and V_{DD} and I_{DD} are measured by Iwatsu VOAC7523. The analytical and the experimental waveforms for nominal conditions were presented in Fig. 3.6. It is seen from Fig. 3.6 that the class-E ZVS/ZDS conditions had been achieved in this state. We define the state in Table 3.1 and Fig. 3.6 is the "nominal state". At following measurements, some parameters varied from the nominal state.

3.6.2 Output Power and Power Conversion Efficiency

The output power and the power conversion efficiency as a function of A were shown Fig. 3.7. It is seen from Fig. 3.7 that both the output power and the power conversion efficiency are sensitive to the operating frequency. Generally, the maximum output power can be obtained for $A < 1$. This is because the output resonant filter works as an inductive filter for the nominal conditions [20]. Conversely, the maximum power conversion efficiency was obtained for $A = 0.897$, which can be obtained by solving $\partial\eta/\partial A = 0$.

Figure 3.8 shows the output power and the power conversion efficiency as a function of C_S/C_{Snom}. Compared with Fig. 3.7, it is seen that the power conversion efficiency is almost constant for C_S variations. The output power is also not sensitive to the C_S variations compared with Fig. 3.7. For $C_S/C_{Snom} < 1$, the Case-3 switching pattern appears. It is seen from Fig. 3.8 that the analytical expressions of the output power and the power conversion efficiency are valid for the Case-3 switching pattern.

Figure 3.8(a) also shows the previous analytical result, which can be obtained by using the analytical expression of the output power in [17]. In [17], the Case-3 parameter region is recognized as the Case-1 parameter region. It is seen from Fig. 3.8(a) that the previous analytical results are far from the measured ones as decreasing C_S/C_{Snom} and the results from analytical expression obtained in this chapter agree with the measured ones well. This result indicates that the analytical expressions in this chapter provide more accurate predictions than the previous analytical ones, which is the usefulness of considering the Case-3 waveform in the class-E inverter analysis outside nominal operations.

Figure 3.9 shows the output power and the power-conversion efficiency as a function of D. It is seen from Fig. 3.9 that PSpice simulated and experimental results agreed with the analytical predictions well for $D > 0.3$. Additionally, both the output power and the power conversion efficiency are almost constant around the nominal state. However, differences of the output power between the analytical results and the PSpice simulated and the experimental ones appear for $D < 0.3$.

Figure 3.9(a) also shows the simulation result using the ideal switch model. The PSpice simulation using the ideal switch gives the switch waveform without voltage and current fall times and switching delay. On the other hand, using the MOSFET model includes the voltage and current fall times and switching delay. Namely, the difference between the ideal switch and the MOSFET model in PSpice simulations is the existence of the voltage and the current fall times and switching delay. It is seen from Fig. 3.9(a) that the analytical plots and experimental ones agreed with the plots from PSpice simulations using ideal switch and those with MOSFET model, respectively. From the above results, it is stated that the difference between analytical and experimental results for small D appears because the analytical model does not consider the voltage and current fall times and switching delay.

It is seen from Figs. 3.7, 3.8, and 3.9 that the analytical predictions agreed with the PSpice simulated results and the experimental measurements quantitatively, which validated the accuracy and effectiveness of the analytical expressions in this chapter.

Additionally, it is seen from Figs. 3.8 and 3.9 that the Case-3 regions appear in wide region near the nominal-condition point. These results also indicate the importance of including the Case-3 switching pattern in the analysis for class-E inverter outside nominal operations.

Table 3.2 gives the computation times for drawing Figs. 3.8 and 3.9 by using the analytical expressions and PSpice simulations. The computations were carried out on the computer whose specifications are as follows: CPU: Intel Core2 Extreme 3.00 GHz Processor, memory: 3.25 GB, and operating system: Windows XP professional version 2002 Service Pack 3. The C-language program was used for calculations by using analytical expressions. PSpice version 16.0 was used as a circuit simulator. The number of plotting points in Figs. 3.8 and 3.9 is 500. In the PSpice simulations, 200 μs was set as the run time with 10 ns maximum step size for the PSpice transient analysis and the parametric sweep mode was used. It is seen from Table 3.2 that the computation cost when the analytical expressions are used is much lower than that for PSpice-simulation usage.

3.7 Distribution of Switching Patterns

Because the switching pattern can be obtained as shown in Section 3.4, it is possible to obtain switching-pattern distribution maps, which is one of the applications of the analytical expressions. From the switching-pattern distribution maps, a lot of information can be obtained. Figure 3.10 shows the switching-pattern distributions on the $C_0/C_{0nom} - C_S/C_{Snom}$ and $f/f_{nom} - D$ plane. For obtaining these figures, C_S and D are calculated by solving the boundary condition between Cases 1 and 2 numerically for fixed C_0 and f, respectively, which is

$$v_{S1}(2\pi D) = 0, \qquad \text{for } \theta_1 = \theta_2 = 2\pi D. \tag{3.40}$$

We can follow the boundary curve by solving the boundary condition by varying the resonant capacitance C_0 and the frequency f, respectively. Similarly, the boundary conditions between Cases 2 and 3 and between Cases 1 and 3 are expressed as

$$i_{S2}(2\pi D) = 0, \qquad \text{for } \theta_2 = 2\pi D, \tag{3.41}$$

and

$$v_{S1}(\theta'_a) = 0, \quad \text{for } \theta_1 = \theta_2 = 2\pi D. \tag{3.42}$$

Note that θ'_a in (3.42) is the nearest value to $2\pi D$ in (3.24).

It is obviously seen from the boundary conditions in (3.40)–(3.42) that a point, at which three boundary curves cross, satisfies the nominal conditions. This can be confirmed from Fig. 3.10. Additionally, it is also seen from Fig. 3.10 that not only Case-2 but also Case-3 switching patterns occupies wide regions, which have never been described in the analytical expressions in the previous studies. The analytical expressions in this chapter cover much wider parameter region than those in the previous studies.

It is seen from Fig. 3.10(a) that the ZVS region, namely Case 2 region, appears only for $C_0/C_{0nom} > 1.0$ and there is no ZVS region for $C_S/C_{Snom} > 1.05$. In [18], the adjusting method of the load network for achieving the class-E ZVS/ZDS conditions is introduced. This method is very useful for design of the class-E inverter. In addition, the Case-3 switching pattern is considered in this method, which indicates the importance of including Case-3 switching pattern in the class-E inverter operations. In [18], however, the adjusting strategies are shown qualitatively, not quantitatively. Switching-pattern distribution maps like Fig. 3.10(a) give the quantitative adjustment criteria on any parameter plane, which enhance the adjusting method in [18].

It is seen from Fig. 3.10(b) that there are two sets of parameters, which satisfy the class-E ZVS/ZDS conditions on the $f/f_{nom} - D$ plane. Additionally, it is also seen from Fig. 3.10(b) that the ZVS region appears only for $1.00 < f/f_{nom} < 1.11$ and $0.48 < D < 0.72$. Because both f and D are controllable parameters, this figure gives important information for the inverter control. It is seen from Fig. 3.10(b) that the FM and PWM control [2], [9] is one of the good strategies to control the output power of the class-E inverter with achieving the ZVS.

From above examples and discussions, it can be stated that the analytical expressions obtained in this chapter are powerful tools for obtaining a lot of information on the class-E inverter.

Figure 3.11 shows the analytical, PSpice simulated and experimental waveforms for the Case-1, Case-2, and Case-3 switching patterns and another class-E switching conditions. Each parameter is marked on Fig. 3.10. It is seen from Figs. 3.11(b) and (c) that the analytical waveform equations in this chapter express the MOSFET-body-diode effect accurately. It can be confirmed from Fig. 3.11 that all the switching patterns of the analytical waveforms agreed with those of simulated and experimental ones. These results show the validity of the switching-pattern distribution map in Fig. 3.10 and the accuracy of the analytical waveform expressions.

3.8 Application of Analytical Expressions - Design of Class-E Inverter with Inductive Impedance Inverter

It is generally stated that the analytical expressions has a potential to be basement of many applications, such as control, new topology, and so on. The analytical expressions presented in this chapter are valid for wide parameter region, which includes not only the nominal-condition parameters but also outside nominal-conditions ones. Therefore, the application area of the analytical expressions presented in this chapter is very wide. Many class-E switching circuits [4]-[8] are transformed into the basic class-E inverter as shown in Fig. 3.1 for their designs. From this point of view, it can be also stated that the analytical expressions presented in this chapter are very useful and applicable for many applications of the class-E switching circuits.

In this section, the analytical expressions derived in this chapter are applied to the design of the class-E inverter with an inductive impedance inverter. Figure 3.12(a) shows the class-E inverter with an inductive impedance inverter [5]. The inductance L_p acts as an impedance inverter. In the basic class-E inverter as shown in Fig. 3.1, it is known that the ZVS is achieved when the load resistance varies in the region of $0 \leq R \leq R_{nom}$ [21]. The purpose of L_p addition is to achieve the ZVS for all load variations. By transforming the $L_p - R_o$ parallel circuit into its equivalent $L_S - R_{eq}$ series circuit, the equivalent circuit of Fig. 3.12(a) is the same as the basic topology of the class-E inverter as shown in Fig. 3.12(b). Therefore, the analytical expressions in this chapter can be easily applied to the operation comprehension of the class-E inverter with an inductive impedance inverter. In this section, the design specifications are the same as in Sect. 3.6. The design values for nominal operation were derived by using the design equations in [5] and [19], which are $C_{0nom} = 7.20$ nF, $C_{Snom} = 11.7$ nF, $L_{rsnom} = 3.58$ μH, and $L_{pnom} = 0.796$ μH.

From [5], the relationships among the component values of the parallel and series circuits at the operating frequency f are

$$R_{eq} = \frac{R_o}{1 + \left(\dfrac{R_o}{X_{L_p}}\right)^2} \quad \text{and} \quad X_{L_S} = \frac{X_{L_p}}{1 + \left(\dfrac{X_{L_p}}{R_o}\right)^2}, \tag{3.43}$$

where $X_{L_p} = \omega L_p$ and $X_{L_S} = \omega L_S$. In [5], the inverters were designed for satisfying $R_{eq} \leq R_{eqnom}$ for any R_o. Because $R_{eq} \leq R_{eqnom}$ is achieved for all load variations, it was stated that the class-E inverter with an inductive impedance inverter can keep ZVS for all load variations. The variations of X_{L_S} for R_o variations were, however, not considered in [5].

Figure 3.13(a) shows the switching-pattern distribution on the L_{eq}/L_{eqnom} and R_{eq}/R_{eqnom} plane, where $L_{eq} = L_{rs} + L_S$ as shown in Fig. 3.12(b). The line on Fig. 3.13(a) expresses L_{eq}/L_{eqnom} and R_{eq}/R_{eqnom} values for $0 \leq R_o \leq \infty$ variations. It is seen from Fig. 3.13(a) that the R_{eq} is always less than R_{eqnom} for R_o variation. However, the non-ZVS region appears for $0 \leq R_o < R_{onom}$ because the reactance X_{L_S} becomes smaller than that of the design value for $0 \leq R_o < R_{onom}$.

Figure 3.13(b) shows the parameter region on L_{rs}/L_{rsnom} and L_p/L_{pnom} plane where the inverter always achieves the ZVS for $0 \leq R_o \leq 1000 \cdot R_{onom}$. This figure is obtained by checking the switching-pattern distribution maps in increments of $0.01 \cdot R_{onom}$ for $0 \leq R_o < 10 \cdot R_{onom}$ and $2 \cdot R_{onom}$ for $10 \cdot R_{onom} \leq R_o \leq 1000 \cdot R_{onom}$, namely 1495 switching-pattern distribution maps were drawn and checked. By using the analytical expressions in this chapter, Fig. 3.13(b) can be obtained in a short time. We would like to emphasize that it is too hard to obtain the same result in actual time if we use the circuit simulator for checking the switching conditions. It is seen from Fig. 3.13(b) that if the inductance values L_{rs} and L_p are in the dotted region, namely slightly changed from the nominal value, the ZVS can be achieved regardless of R_o.

Figures 3.13(c) and (d) show the switching-pattern distributions on L_p/L_{pnom} and R_o/R_{onom} plane at $L_{rs}/L_{rsnom} = 1.07$ and L_{rs}/L_{rsnom} and R_o/R_{onom} plane at $L_p/L_{pnom} = 0.7$, respectively. It can be confirmed from these figures that the class-E inverter with an inductive impedance inverter achieves the ZVS condition regardless of load resistance. As a result, it is possible to design the ZVS inverters when L_{rs} and L_p are fixed in the dotted-region value in Fig. 3.13(b). For example, when $L_{rs} = 1.07 \times L_{rsnom} = 3.83\ \mu$H and $L_p = 0.9 \times L_{pnom} = 0.716\ \mu$H, the inverter always achieves the ZVS regardless of load resistance R_o. Figure 3.14 shows the analytical, PSpice simulation, and experimental waveforms for $R_o = R_{onom}/2 = 2.5\ \Omega$. Figure 3.14(a) shows waveforms for $L_{rs} = 3.58\ \mu$H, $L_p = 0.796\ \mu$H, $C_0 = 7.20$ nF, and $C_S = 11.7$ nF, which were obtained from the design equations in [5] and [19]. It is seen from this figure that the switch waveform did not satisfy ZVS condition though it was thought in [5] that the ZVS can be achieved at any load resistances. Figure 3.14(b) shows waveforms for $L_{rs} = 3.83\ \mu$H, $L_p = 0.716\ \mu$H, $C_0 = 7.20$ nF, and $C_S = 11.7$ nF, which were obtained from this-chapter design. It is seen from this figure that the inverter achieved ZVS. We confirmed that the inverter with this-chapter design values always achieved ZVS at any load resistances by both PSpice simulations and circuit experiments. In addition, all the analytical waveforms in Fig. 3.14 showed quantitative agreements with experimental and simulation waveforms, which showed the validity of Fig. 3.13 and the effectiveness of the presented analytical expressions.

3.9 Conclusion

This chapter has presented the analytical expressions for steady-state waveforms, output power, and power conversion efficiency for the class-E inverter outside the class-E ZVS/ZDS switching conditions at a high Q and any duty ratio. By considering the switch-voltage recovery during the MOSFET body diode on-state, the applicable parameter range of the analytical expressions is much wider than that of the previous analytical expressions. The analytical expressions in this chapter cover all the results in [15]-[17]. It is shown that the analytical predictions agreed with the simulated and the experimental results quantitatively, which indicates the validity of the analytical expressions. Additionally, the switching-pattern distribution maps are shown, which can be obtained from the waveform equations obtained in this chapter. From the distribution maps, we can obtain the strategies of the quantitative load-network-parameter adjustment for achieving the class-E ZVS/ZDS conditions and the control strategies with satisfying the ZVS condition. From the results in this chapter, it can be stated that the analytical expressions obtained in this chapter are powerful tools for obtaining a lot of information on the class-E inverter.

Appendix

Derivation of I_m, I_{DD} and ϕ

While the switch is in the off state, the current through the shunt capacitance is given by (3.21). While the switch is in the on state and off-state, the current through the switch is given by (3.22). The voltage across the switch is

$$v_S = \frac{1}{\omega C_S}\int_0^{\theta} i_{C_S} d\theta =$$
$$\begin{cases} v_{S1} = \dfrac{1}{\omega C_S}\displaystyle\int_0^{\theta}[I_{DD} - I_m \sin(\theta+\phi)]d\theta, & \text{for } 0 \le \theta < \theta_1 \\ v_{S2} = 0, & \text{for } 0 \le \theta < \theta_1 \\ v_{S3} = \dfrac{1}{\omega C_S}\displaystyle\int_{\theta_2}^{\theta}[I_{DD} - I_m \sin(\theta+\phi)]d\theta, & \text{for } \theta_2 \le \theta < 2\pi D \\ v_{S4} = 0, & \text{for } 2\pi D \le \theta < 2\pi. \end{cases} \tag{3.44}$$

From (3.44), (3.19) is obtained. There are three unknown parameters in (3.19), which are I_{DD}, I_m, and ϕ. These three unknown parameters can be obtained from the analytical process described in the below. Because of the assumption (b), the dc voltage drop across the choke inductor L_C is zero. Therefore, the dc-supply voltage is

$$\begin{aligned} V_{DD} &= \frac{1}{2\pi}\int_0^{2\pi} v_S d\theta \\ &= \frac{A^2BQR}{2\pi}\left\langle \frac{I_{DD}}{2}(\theta_1^2 + \theta_2^2 + 4\pi^2D^2 - 2\pi D\theta_2) + I_m[\sin(\theta_1+\phi) \right. \\ &\quad - \sin\phi - \theta_1\cos\phi + \sin(2\pi D + \phi) - \sin(\theta_2+\phi) \\ &\quad \left. +(\theta_2 - 2\pi D)\cos(\theta_2+\phi)] \right\rangle, \end{aligned} \tag{3.45}$$

Now, L_0 is divided into L_r and L_x, where $L_r = 1/\omega_0^2 C_0$ as shown in Fig 3.15. Therefore, the impedance of the resonant circuit C_0-L_r is zero at the operating frequency. By applying Fourier analyses, the voltage amplitudes on R and L_x are

$$\begin{aligned}
V_o = RI_m &= \frac{1}{\pi}\int_0^{2\pi} v_S \sin(\theta+\phi)d\theta \\
&= \frac{A^2BQR}{\pi}\Bigg\{ I_{DD}\big[\sin(\theta_1+\phi) - \theta_1\cos(\theta_1+\phi) - \sin\phi \\
&\quad +(\theta_2 - 2\pi D)\cos(2\pi D+\phi) + \sin(2\pi D+\phi) - \sin(\theta_2+\phi)\big] \\
&\quad +I_m\Bigg[\frac{1}{4}\cos(2\theta_2+2\phi) - \frac{1}{4}\cos(2\theta_1+2\phi) + \cos\phi\cos(\theta_1+\phi) \\
&\quad +\frac{1}{4}\cos 2\phi - \cos^2\phi - \frac{1}{4}\cos(4\pi D+2\phi) + \frac{1}{4}\cos(2\theta_2+2\phi) \\
&\quad +\cos(\theta_2+\phi)\cos(2\pi D+\phi) - \cos^2(\theta_2+\phi)\Bigg]\Bigg\},
\end{aligned} \tag{3.46}$$

and

$$\begin{aligned}
V_X = \omega L_X I_m &= \frac{1}{\pi}\int_0^{2\pi} v_S \cos(\theta+\phi)d\theta \\
&= \frac{A^2BQR}{\pi}\Bigg\{ I_{DD}\big[\theta_1\sin(\theta_1+\phi) + \cos(\theta_1+\phi) - \cos\phi \\
&\quad +(2\pi D - \theta_2)\sin(2\pi D+\phi) + \cos(2\pi D+\phi) - \cos(\theta_2+\phi)\big] \\
&\quad +I_m\Bigg[\frac{1}{4}\sin(2\theta_1+2\phi) - \frac{1}{4}\sin 2\phi - \cos\phi\sin(\theta_1+\phi) \\
&\quad +\cos\phi\sin\phi + \frac{1}{4}\sin(4\pi D+2\phi) - \frac{1}{4}\sin(2\theta_2+2\phi) \\
&\quad -\cos(\theta_2+\phi)\sin(2\pi D+\phi) + \cos(\theta_2+\phi)\sin(\theta_2+\phi) \\
&\quad +\frac{1}{2}(\theta_1-\theta_2) + \pi D\Bigg]\Bigg\},
\end{aligned} \tag{3.47}$$

Respectively. From (3.45)–(3.47), we have

$$\frac{2\pi V_{DD}}{A^2BQR} = \delta I_{DD} + \gamma I_m, \tag{3.48}$$

$$\frac{I_{DD}}{I_m} = \frac{\alpha}{\beta}, \tag{3.49}$$

and

$$\frac{I_{DD}}{I_m} = \frac{k_8 \cos^2\phi + k_9 \cos\phi \sin\phi + k_{10}}{k_5 \cos\phi - k_4 \sin\phi}. \tag{3.50}$$

From (3.48) and (3.49), (3.3) and (3.20) can be obtained. Additionally, from (3.49) and (3.50), I_{DD}/I_m can be eliminated and we obtain

$$\begin{aligned}
&(k_1k_5 - k_4k_8)\cos^3\phi + (k_2k_5 - k_1k_4 - k_4k_9 - k_5k_8)\cos^2\phi\sin\phi \\
&+(-k_2k_4 - k_5k_9)\sin^2\phi\cos\phi + (k_5k_3 - k_4k_{10})\cos\phi \\
&+(-k_3k_4 - k_5k_{10})\sin\phi = 0.
\end{aligned} \tag{3.51}$$

Because of $\cos\phi = \cos^3\phi + \cos\phi\sin^2\phi$ and $\sin\phi = \sin\phi\cos^2\phi + \sin^3\phi$, (3.51) can be renewed as

$$\begin{aligned}
&(k_1k_5 - k_4k_8 + k_5k_3 - k_4k_{10})\cos^3\phi + (-k_3k_4 - k_5k_{10})\sin^3\phi \\
&+(k_2k_5 - k_1k_4 - k_4k_9 - k_5k_8 - k_3k_4 - k_5k_{10})\cos^2\phi\sin\phi \\
&+(k_3k_5 - k_2k_4 - k_5k_9 - k_4k_{10})\sin^2\phi\cos\phi = 0.
\end{aligned} \tag{3.52}$$

By dividing (3.52) by $\cos^3\phi$, (3.15) can be derived.

Table 3.1: Analytical predictions and experimental measurements for nominal condition

	Analytical	Measured	Difference
V_{DD}	5.0 V	5.0 V	0.00 %
D	0.5	0.5	0.00 %
f	1 MHz	1 MHz	0.00 %
R	5.00 Ω	4.99 Ω	-0.20 %
L_C	34.7 μH	43.0 μH	24.1 %
L_0	7.96 μH	8.01 μH	0.68 %
C_S	5.84 nF	5.81 nF	-0.65 %
C_0	3.60 nF	3.53 nF	-1.88 %
r_S	-	0.16 Ω	-
r_{C_S}	-	0.0 Ω	-
$r_{L_0C_0}$	-	0.20 Ω	-
r_{L_C}	-	0.01 Ω	-
P_o	2.88 W	2.87 W	-0.35 %
η	92.2 %	91.8 %	-0.46 %

Table 3.2: Computation times by using analytical expressions and PSpice simulation

Figure 3.8		Figure 3.9	
Analytical	Simulated	Analytical	Simulated
0.406 s	432 s	0.390 s	642 s

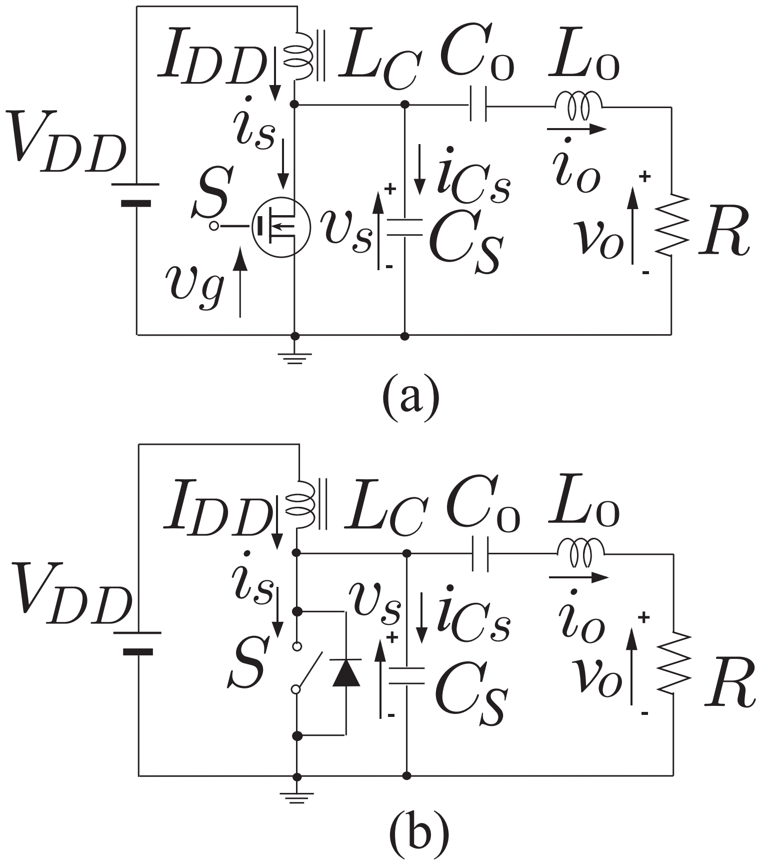

Figure 3.1: (a) Circuit topology of class-E inverter. (b) Equivalent circuit of class-E inverter.

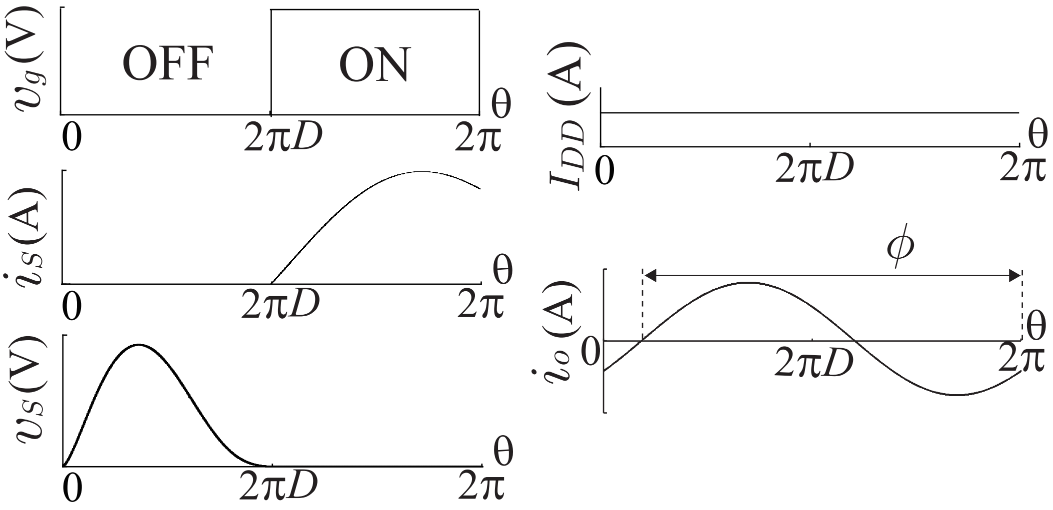

Figure 3.2: Example waveforms in the class-E inverter satisfying nominal conditions for $D = 0.5$.

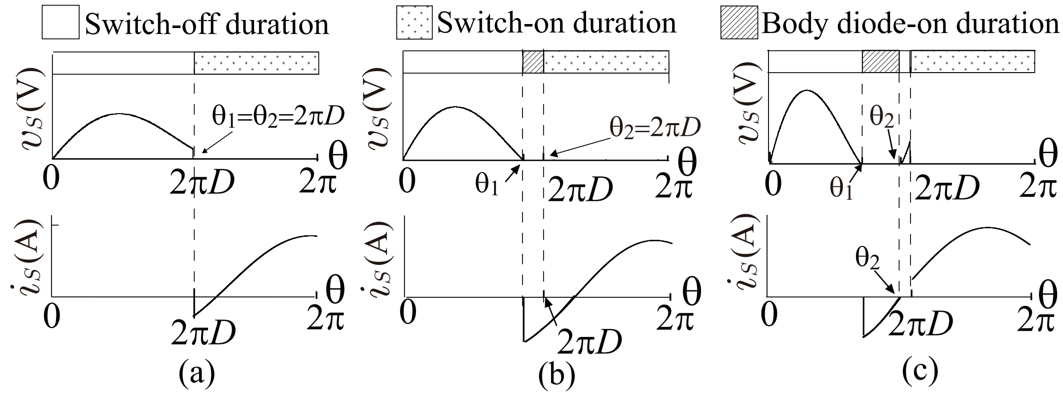

Figure 3.3: Switch voltage and current waveforms of the class-E inverter. (a) Case 1. (b) Case 2. (c) Case 3.

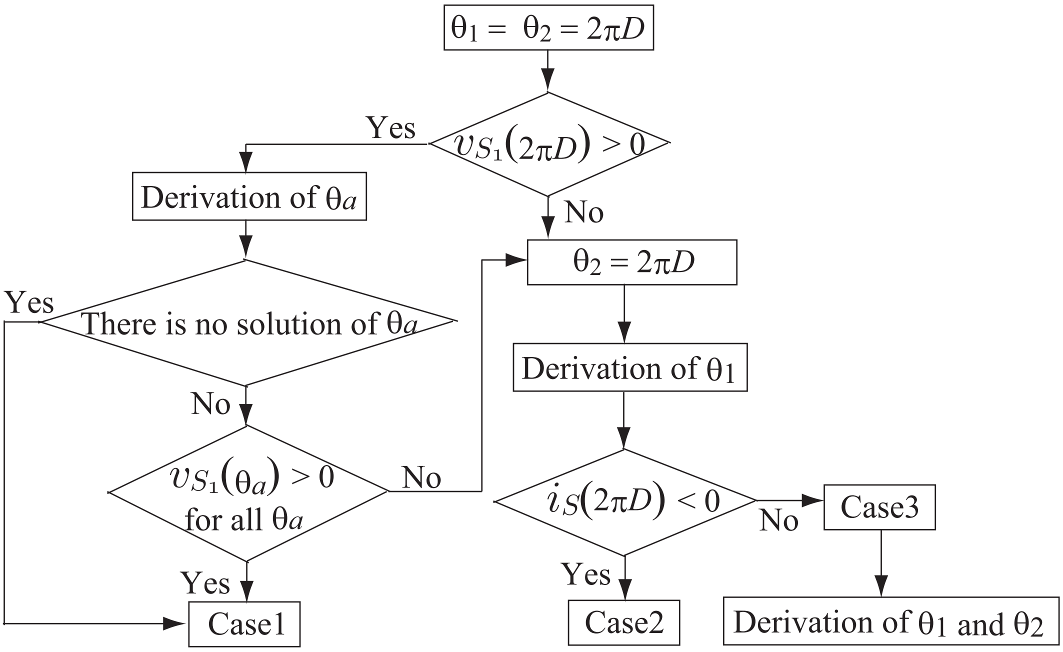

Figure 3.4: Flowchart for obtaining θ_1 and θ_2.

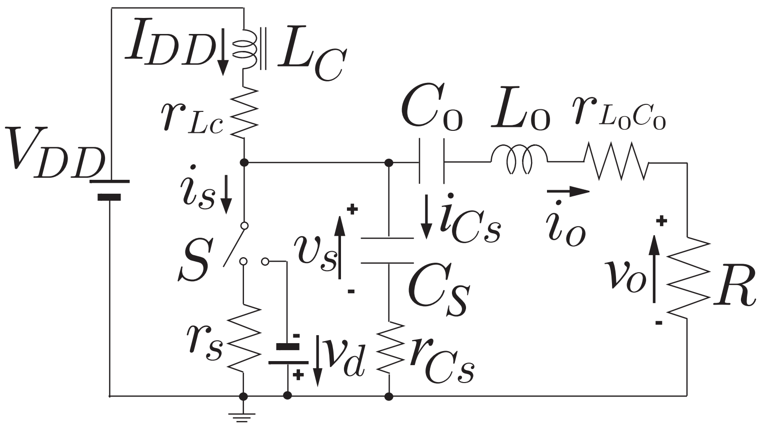

Figure 3.5: Equivalent circuit of class-E inverter for power-loss calculations.

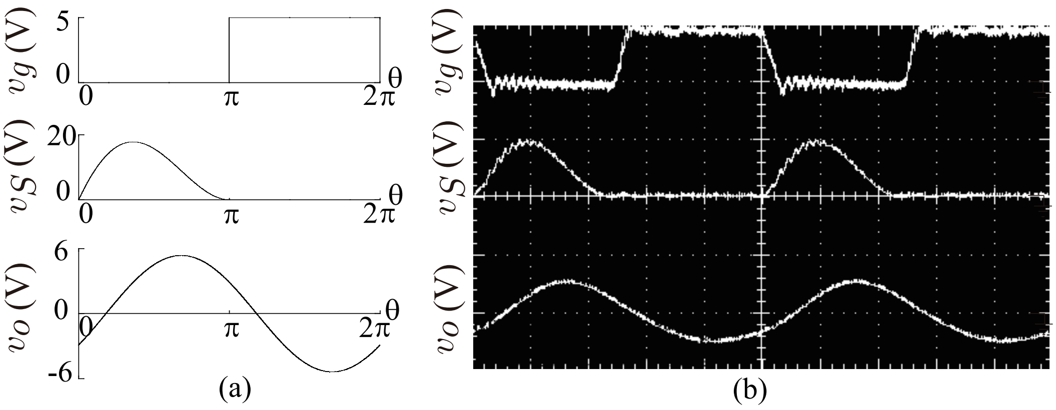

Figure 3.6: Waveforms for the nominal operation. (a) Analytical waveforms. (b) Experimental waveforms, vertical of v_g: 5 V/div, v_S: 20 V/div, v_o: 10 V/div. horizontal: 200 ns/div.

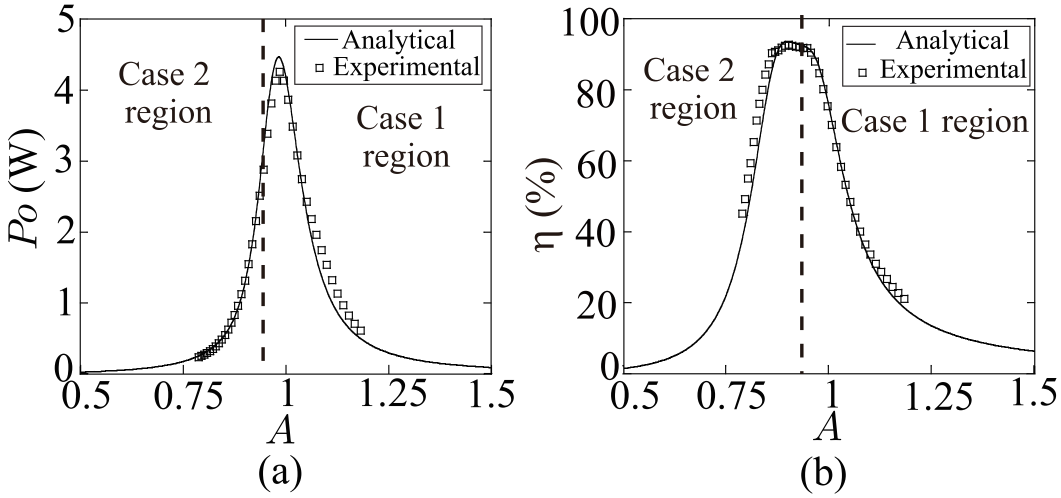

Figure 3.7: Output power and power conversion efficiency as functions of A. (a) Output power. (b) Power conversion efficiency.

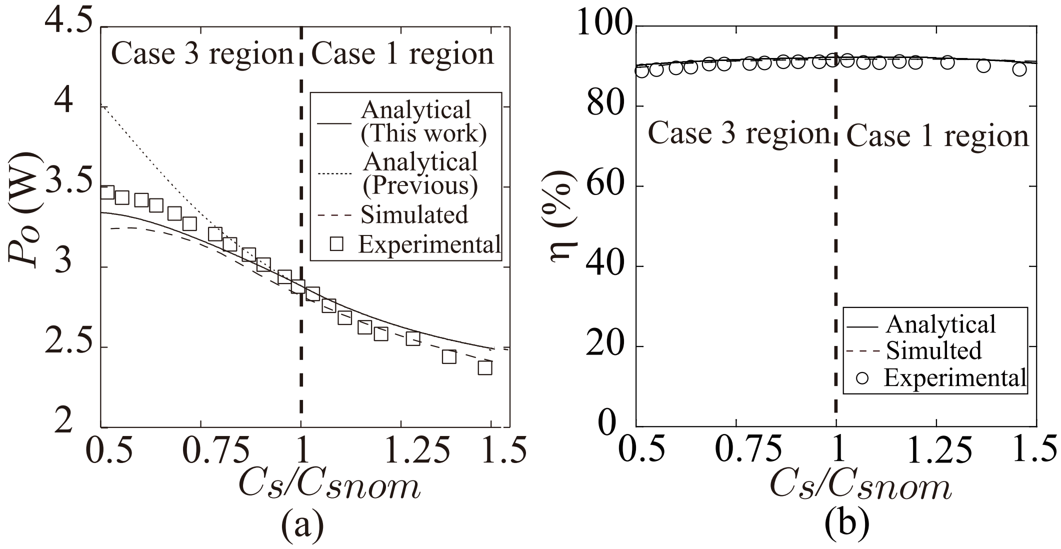

Figure 3.8: Output power and power conversion efficiency as functions of C_S/C_{Snom}. (a) Output power.(b) Power-conversion efficiency.

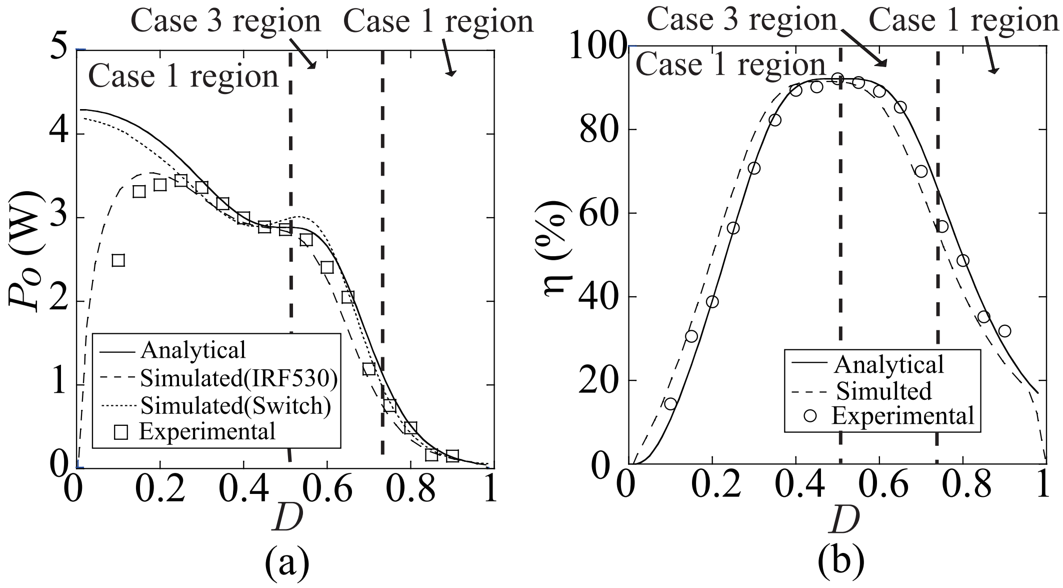

Figure 3.9: Output power and power conversion efficiency as functions of D. (a) Output power. (b) Power-conversion efficiency.

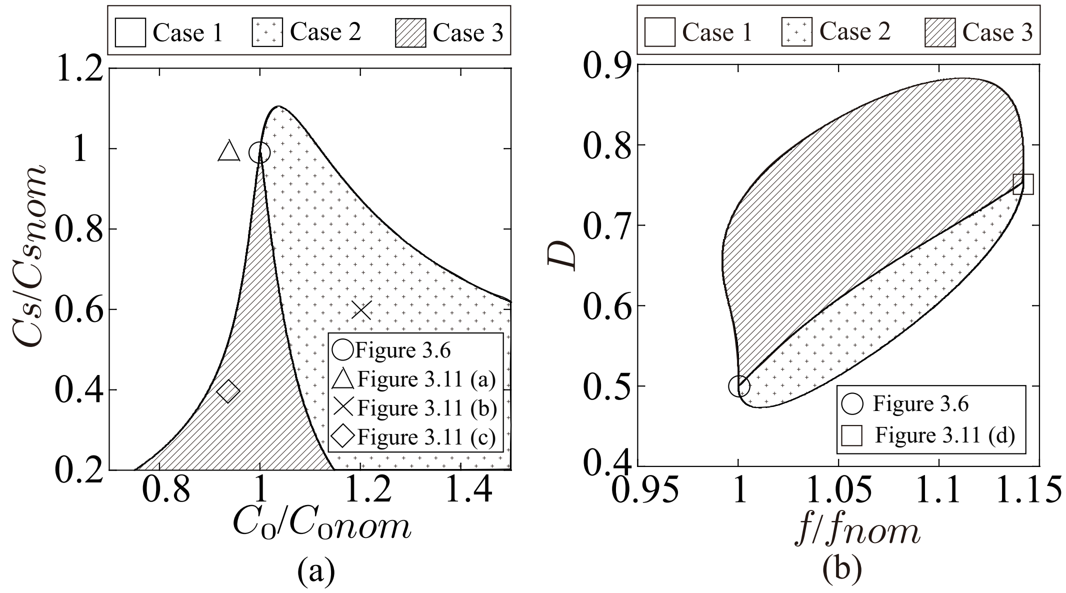

Figure 3.10: Distributions of switching patterns. (a) $C_0/C_{0nom} - C_S/C_{Snom}$ plane. (b) $f/f_{nom} - D$ plane.

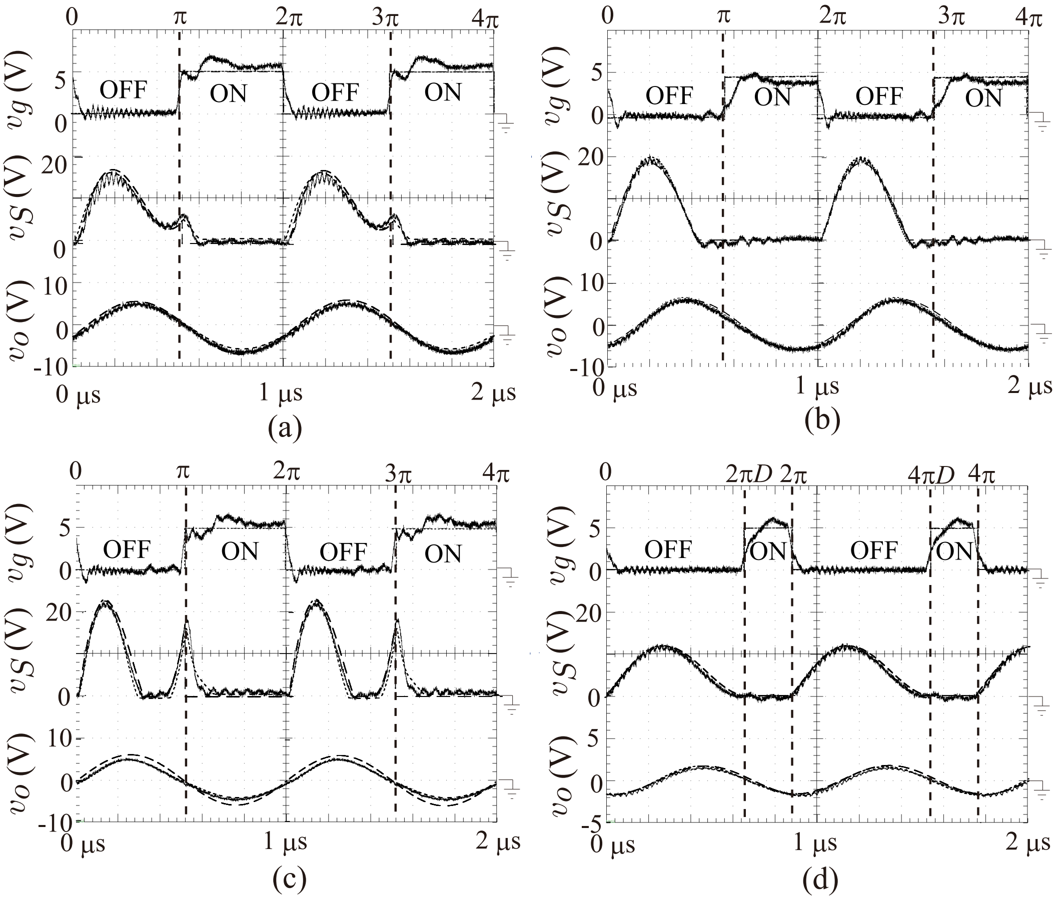

Figure 3.11: Waveforms obtained from analytical expressions (dashed line), PSpice simulations (dotted line), and circuit experiments (solid line). (a) Case 1 for $C_0/C_{0nom} = 0.95$ and $C_S/C_{Snom} = 1$. (b) Case 2 for $C_0/C_{0nom} = 1.2$ and $C_S/C_{Snom} = 0.6$. (c) Case 3 for $C_0/C_{0nom} = 0.95$ and $C_S/C_{Snom} = 0.4$. (d) another class-E switching condition for $f/f_{nom} = 1.14$ and $D = 0.75$.

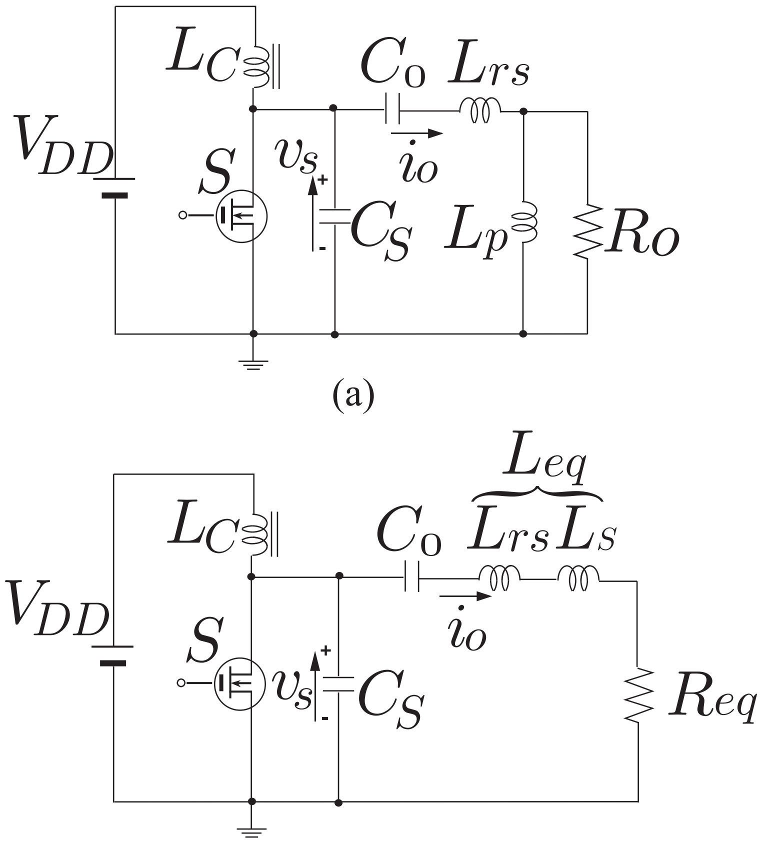

(a)

(b)

Figure 3.12: Class-E inverter with an inductive impedance inverter. (a) Circuit of the inverter. (b) equivalent circuit of the inverter.

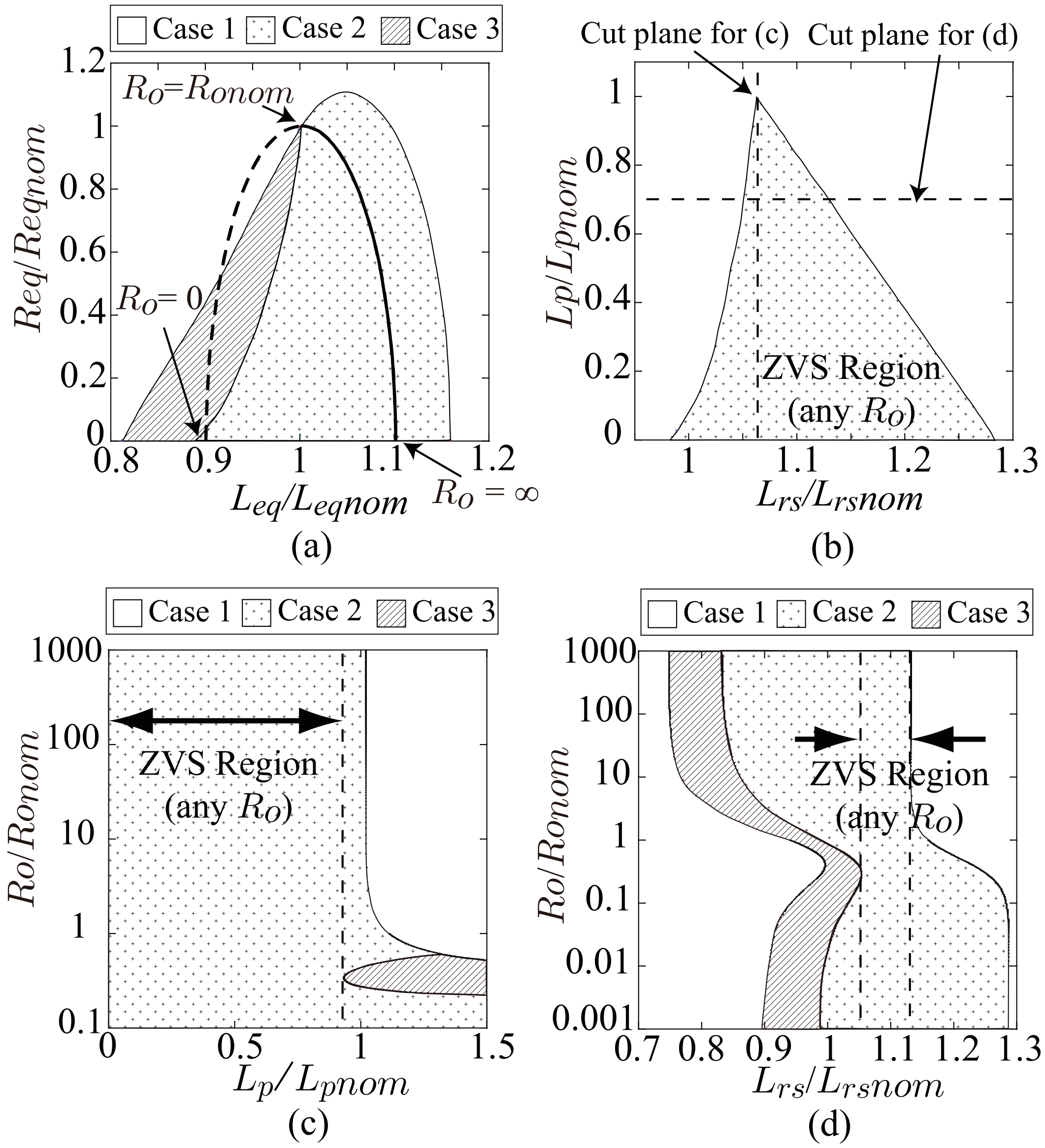

Figure 3.13: Switching-pattern distributions for the class-E inverter with inductive impedance inverter. (a) Switching-pattern distribution on L_{eq}/L_{eqnom} and R_{eq}/R_{eqnom} plane and the variation of L_{eq} and R_{eq} against R_o. (b) ZVS region at any R_o on L_{rs}/L_{rsnom} and L_p/L_{pnom} plane. (c) Switching-pattern distribution on L_p/L_{pnom} and R_o/R_{onom} plane at $L_{rs}/L_{rsnom} = 1.07$. (d) Switching-pattern distribution on L_{rs}/L_{rsnom} and R_o/R_{onom} plane at $L_p/L_{pnom} = 0.7$.

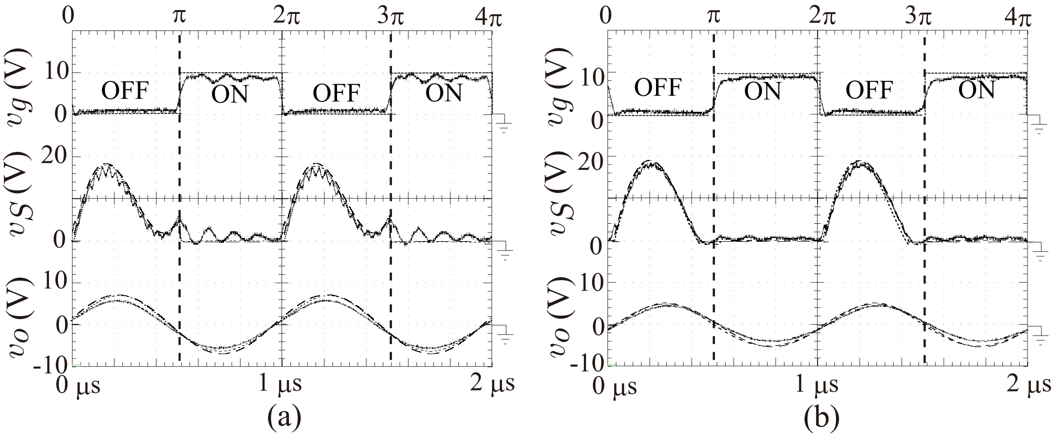

Figure 3.14: Analytical (dashed line), PSpice simulation (dotted line), and experimental (solid line) waveforms of the class-E inverter with an inductive impedance inverter for $R_o = R_{onom}/2 = 2.5\ \Omega$. (a) With design values from [5] and [19] for $L_{rs} = 3.58\ \mu$H and $L_p = 0.796\ \mu$H. (b) With design values obtained from this-chapter design for $L_{rs} = 3.83\ \mu$H and $L_p = 0.716\ \mu$H.

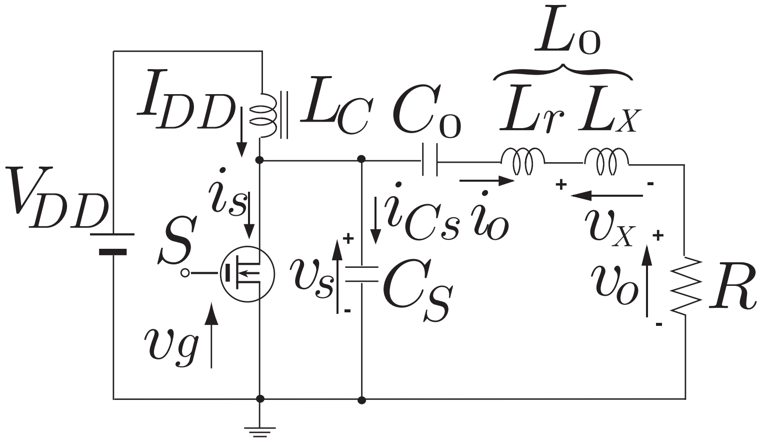

Figure 3.15: Circuit topology of class-E inverter for the analysis.

References

[1] C, Branas, F. J. Azcondo, and R. Zane, "Power-mode control of multiphase resonant electronic ballast," *IEEE Trans. Ind. Electron.*, vol. 59, no. 4, pp.1770–1778, Apr. 2012.

[2] H. Sekiya, H. Koizumi, S. Mori, I. Sasase, J. Lu, and T. Yahagi, "FM/PWM control scheme in class DE inverter," *IEEE Trans. Circuits Syst.,* vol. 51, no. 7, pp. 1250-1260, Jul. 2004.

[3] N. O. Sokal and A. D. Sokal, "Class E - A new class of high-efficiency tuned single-ended switching power amplifiers," *IEEE Jounal of Solid State Circuits*, vol. 10, no. 3, pp. 168–176, Jun. 1975.

[4] I. Boonyaroonate and S. Mori, "Analysis and design of class E isolated DC/DC converter using class E low *dv/dt* PWM synchronous rectifier," *IEEE Trans. Power Electron.*, vol. 16, no. 4, pp. 514–521, Jul. 2001.

[5] M. K. Kazimierczuk and X. T. Bui, "Class-E amplifier with an inductive impedance inverter," *IEEE Trans. Ind. Electron.*, vol. 37, no. 2, pp. 160–166, Apr. 1990.

[6] Y. C. Chuang, Y. L. Ke, H. S. Chuang, and M. L. Chou, "Electronic ballasts driven by hybrid source using microprocessor-controlled digital switching technique," *IEEE Trans. Ind. Appl.*, vol. 47, no. 3, pp. 1452–1460, May/Jun. 2011.

[7] H. L. Cheng, C. A. Cheng, C. C. Fang, and H. C. Yen, "Single-switch high-power-factor inverter driving piezoelectric ceramic transducer for ultrasonic cleaner," *IEEE Trans. Ind. Electron.*, vol. 58, no. 7, pp. 2898–2905, Jul. 2011.

[8] Z. N. Low, J. J. Casanova, P. H. Maier, J. A. Taylor, R. A. Chinga, and J. Lin, "Method of load/fault detection for loosely coupled planar wireless power transfer

system with power delivery tracking," *IEEE Trans. Ind. Electron.*, vol. 57, no. 4, pp.1478–1486, Apr. 2010.

[9] J. S. Walling and D. J. Allstot, "Pulse-width modulated CMOS power amplifiers," *IEEE Microwave Mag.*, vol. 12, pp. 52-60, Feb. 2011.

[10] T. Suetsugu and M. Kazimierczuk, "Design procedure of class-E amplifier for off-nominal operation at 50 % duty ratio," *IEEE Trans. Circuits Syst.-I*, vol. 53, no. 7, pp. 1468–1476, Jul. 2006.

[11] T. Suetsugu and M. Kazimierczuk, "Off-nominal operation of class-E amplifier at any duty ratio," *IEEE Trans. Circuits Syst.-I*, vol. 54, no. 6, pp. 1389–1397, Jun. 2007.

[12] J. Liang and W. Liao, "Steady-state simulations and optimization of class-E power amplifiers with extended impedance method," *IEEE Trans. Circuits Syst.-I*, vol. 58, no. 6, pp. 1433–1445, Jun. 2011.

[13] K. Kundert and A. Sangiovanni-Vincentelli, "Simulation of nonlinear circuits in the frequency domain," *IEEE Trans. Comput. Aided Design Integr. Circuits Syst.,* vol. 5, no. 4, pp. 521–535, Oct. 1986.

[14] G. Rhyne, M. Steer, and B. Bates, "Frequency-domain nonlinear circuit analysis using generalized power series," *IEEE Trans. Microw. Theory Tech.,* vol. 36, no. 2, pp. 379–387, Feb. 1988.

[15] T. Suetsugu and M. Kazimierczuk, "Steady-state behavior of class E amplifier outside designed conditions, " *in Proc. IEEE ISCAS,* Kobe, Japan, May, 2005, pp. 708–711.

[16] T. Suetsugu and M. Kazimierczuk, “Power efficiency calculation of class E amplifier with nonlinear shunt capacitance,” *in Proc. IEEE ISCAS,* Paris, France, May, 2010, pp. 2714–2717.

[17] T. Nagashima, X. Wei, H. Sekiya, and M. K. Kazimierczuk, “Power conversion efficiency of class-E power amplifier outside nominal operations,” *in Proc. IEEE ISCAS,* Rio de Janeiro, Brazil, May 2011, pp.749–752.

[18] N. O. Sokal, “Class-E RF power amplifiers”, *QEX*, no. 204, pp. 9-20, Jan./Feb. 2001.

[19] M. K. Kazimierczuk, *RF Power Amplifiers,* New York, NY: John Wiley & Sons, 2008.

[20] F. H. Raab, “Idealized operation of the class E tuned amplifier, ” *IEEE Trans. Circuits Syst.*, vol. 24, no. 12, pp. 725–735, Dec. 1977.

[21] M. K. Kazimierczuk and K. Puczko, “Class-E tuned power amplifier with antiparallel diode or series diode at switch, with any loaded Q and switch duty cycle,” *IEEE Trans. Circuits Syst.*, vol. 36, no. 9, pp. 1201–1209, Sept. 1989.

[22] C. Bernal, E. Oyarbide, P. M. Gaudo, and A. Mediano, “Dynamic model of class-E inverter with multifrequency averaged analysis,” *IEEE Trans. Ind. Electron.*, vol. 59, no. 10, pp. 3737–3744, Oct. 2012.

Chapter 4

Locking Range Derivations for Injection-Locked Class-E Oscillator Applying Phase Reduction Theory

●● ABSTRACT ●●

This chapter presents a numerical locking-range prediction for the injection-locked class-E oscillator using the phase reduction theory (PRT). By applying this method to the injection-locked class-E oscillator designs, which is in the field of electrical engineering, the locking ranges of the oscillator on any injection-signal waveform can be efficiently obtained. The locking ranges obtained from the proposed method quantitatively agreed with those obtained from the simulations and circuit experiments, showing the validity and effectiveness of the locking-range derivation method based on PRT.

4.1 Introduction

In recent years, resonant class-D [1], class-E [2]-[14], and class-DE [15] power oscillators have been widely used in various applications. These resonant power oscillators are oscillated by the feedback voltage transformed from the output voltage. Class-E and class-DE oscillators can achieve high power-conversion efficiencies at high frequencies because of the class-E zero-voltage switching and zero-derivative switching (ZVS/ZDS) operations. Because of their high operational efficiency, these oscillators have many applications such as electric ballasts [6], [7], DC-DC converters [8], [9], and transmitters for wireless power transfer [10], [11], and wireless communication [12]. In such applications, a limitation of the oscillator is that the free-running frequency usually has a small error from the specified frequency owing to component tolerances. Therefore, accurately specified frequency operations are required for practical usage that considers the radio law and phase noise. The injection locking technique [13], [14], [16]-[33] is one solution for this problem.

In the injection-locked class-E oscillator [13], [14], the injection circuit is added to the class-E free-running oscillator for oscillation frequency stabilization. When the feedback voltage of the free-running class-E oscillator is synchronized with the small injection signal, the frequency of the class-E oscillator can be fixed at the injection signal frequency. The locking range prediction for the injection-locked resonant power oscillator is very important and useful for oscillator design [18], [19]. This is because the required injection power for the synchronization can be estimated in the design process.

Analytical expressions of the locking ranges have been previously reported [13] on the basis of Adler's equation [16]-[22]. From these analytical expressions, the locking ranges of injection-locked class-E oscillator can be approximately estimated. This analysis is, however, only valid for the case in which the injection signal is a sinusoidal waveform. For the implementation point of view, it is useful to predict the locking ranges on various injection-signal waveforms. In previous research [14], the locking ranges for the injection-locked class-E oscillator with various injection signal waveforms were numerically obtained. It was also shown that the locking ranges depend on the injection-signal waveform [14]; however, the numerical derivations of locking ranges in this study require high computation cost.

The phase reduction theory (PRT) [24]-[31] is an analysis method developed in the field of physics used for investigating the synchronization phenomena. By expressing the oscillator dynamics as functions of phase variables, the synchronization range can be easily and accurately obtained. The phase sensitivity function (PSF) represents a phase gradient on the limit cycle of the oscillator, which is the most important function used for investigating the synchronization ranges in PRT. The locking range can be obtained from the convolution integral of the PSF and the function of the injection signal. In previous research [29]-[31], PRT has been applied to the weakly coupled oscillators, such as Sturart-Landau and van der Pol oscillators, which shows the utility of PRT. Nevertheless, PRT has never been fully utilized in the research field of power electronics. In this sense, it is important to show that PRT can be applied to the design of resonant power oscillators as an application example.

The objective of this study is to present the feasibility of locking range predictions of the resonant power oscillator by PRT. To our knowledge, our study here is the first study to show a systematic design process with respect to the locking ranges of the resonant oscillator, which can be applied to other injection-locked resonant-power-oscillator designs. It is shown that PRT is quite useful for obtaining the locking ranges of injection-locked class-E oscillators. By applying PRT, it is possible to obtain the locking ranges on any injection-signal waveform at a low computation cost. By conducting simulations and circuit experiments, it was confirmed that the locking ranges predicted by the proposed method quantitatively agree with those obtained from the simulations and circuit experiments, thereby demonstrating the validity and effectiveness of the proposed locking-range-derivation method based on PRT.

4.2 Injection-Locked Class-E Oscillator

Figure 4.1(a) shows the circuit topology of the injection-locked class-E oscillator [13], [14]. This circuit consists of the class-E free-running oscillator [2]-[5] and injection circuit. The class-E free-running oscillator has DC-supply voltage V_{DD}, DC-feed inductance L_C, MOSFET as a switching device S, shunt capacitance C_S, series resonant circuit $L_0 - C_0 - R$, voltage-dividing capacitances C_1 and C_2, feedback inductance L_f for phase shifting, and resistances R_{d1} and R_{d2} for supplying the bias voltage across the gate-to-source of the MOSFET, which are sufficiently large to neglect the current through them.

Figure 4.2 shows example waveforms of the free-running class-E oscillator, particularly for $v_{inj} = 0$ in Fig. 4.1(a). Generally, the resonant circuit $L_0 - C_0 - R$ in the oscillator has a high quality factor Q. Therefore, the current through the resonant circuit i is regarded as a pure sinusoidal current. The feedback voltage v_f, which is obtained from the output voltage, controls the MOSFET. During $v_f \geq V_{th}$, the MOSFET is in the "on" state, as shown in Fig. 4.2, where V_{th} is the gate threshold voltage. On the contrary, in the case of $v_f < V_{th}$, the MOSFET is in the "off" state. During the switch to the off state, the current through the shunt capacitance C_S produces a pulse-like shape of voltage across the switch, as shown in Fig. 4.2. The switching losses are reduced to zero by the operating requirements of zero voltage and zero derivative voltage at the turn-on instant, which are known as class-E ZVS/ZDS conditions [2]-[15], [34] and are expressed as

$$v_S(2\pi) = 0 \quad \text{and} \quad \left.\frac{dv_S}{d\theta}\right|_{\theta=2\pi} = 0. \tag{4.1}$$

The power dissipations caused in the feedback network are kept small because the current i_f through the feedback network is much smaller than the output current i.

Usually, the free-running frequency f_{free} has an error from the specified frequency. One of the techniques used to solve this problem is injection locking [13], [14], [16]-[33]. Because the injection-signal power is low, it is possible to obtain the injection-locked oscillator by just adding the injection signal to the original free-running oscillator. Therefore, the circuit design is simple even when the injection-locking technique is applied. For the injection-locked class-E oscillator used in previous studies [13], [14], a small voltage is injected into the MOSFET gate terminal, as shown in Fig. 4.1(a). If the feedback voltage of the class-E free-running oscillator is synchronized with the injection signal v_{inj}, the oscillation frequency is locked with the injection-signal frequency f_{inj}, which means the frequency of the output voltage is fixed with f_{inj}. It is easy to achieve synchronization as the injection-signal power increases. However, high power injection affects the waveforms of the feedback voltage and switch-on duty ratio, which yields the design complexity. It is necessary to conduct the total design of the free-running oscillator and injection circuits for large perturbation. Additionally, low injection-signal power is good from a power-added efficiency perspective.

4.3 Phase Reduction Theory for Injection-Locked Oscillator

PRT [24]-[31] is an analytical method developed in the field of physics for investigating the synchronization phenomena. By expressing the oscillator dynamics as functions of phase variables, the synchronization range can be obtained easily and accurately.

4.3.1 Phase Function

It is considered that a non-perturbed dynamical system can be expressed as

$$\frac{d\boldsymbol{x}(\theta)}{d\theta} = \boldsymbol{F}(\boldsymbol{x}(\theta)), \tag{4.2}$$

where $\theta = \omega t = 2\pi f_{free} t \in \boldsymbol{R}$ and $\boldsymbol{x} \in \boldsymbol{R}^n$ denote the angular time with free-running frequency and the state-variation vector, respectively. In this study, for simplicity,

$$\boldsymbol{F} : \boldsymbol{R} \times \boldsymbol{R}^n \to \boldsymbol{R}^n(\boldsymbol{x}(\theta)) \to \boldsymbol{F}(\boldsymbol{x}(\theta)) \tag{4.3}$$

is periodic in θ with period 2π as follows:

$$\boldsymbol{F}(\boldsymbol{x}(\theta + 2\pi)) = \boldsymbol{F}(\boldsymbol{x}(\theta)). \tag{4.4}$$

It is assumed that (4.2) has a solution $\boldsymbol{x}(\theta) = \boldsymbol{\varphi}(\theta)$, and that this solution has a limit cycle in the phase space, as shown in Fig. 4.3(a). For the dynamical system, a phase variable is defined as

$$\phi(\boldsymbol{\varphi}) = \theta, \tag{4.5}$$

where ϕ has 2π-periodicity. The derivative of ϕ is obtained as

$$\begin{aligned} \frac{d\phi}{d\theta} &= \frac{\partial \phi}{\partial \boldsymbol{x}} \cdot \frac{d\boldsymbol{\varphi}}{d\theta} \\ &= \frac{\partial \phi}{\partial \boldsymbol{x}} \cdot \boldsymbol{F}(\boldsymbol{x}(\theta)) \\ &= 1. \end{aligned} \tag{4.6}$$

The perturbed dynamical system of (4.2) is expressed as

$$\frac{d\boldsymbol{x}(\theta)}{d\theta} = \boldsymbol{F}(\boldsymbol{x}(\theta)) + \boldsymbol{G}(\Theta), \tag{4.7}$$

where $\boldsymbol{G}(\Theta)$ represents the weak perturbation, which expresses the injection signal in this study, and $\Theta = \Omega t$ is the angular time of perturbation with the angular frequency $\Omega = 2\pi f_{inj}$. It is also assumed that (4.7) has a solution $\boldsymbol{x}(\theta) = \boldsymbol{\varphi}_p(\theta)$. The perturbation drives the trajectory away from the limit cycle $\boldsymbol{\varphi}$. However, the trajectory $\boldsymbol{\varphi}_p$ only slightly deviates from the original trajectory $\boldsymbol{\varphi}$ because the injection signal is small if the limit cycle $\boldsymbol{\varphi}_p$ is stable. Therefore, we can define the phase ϕ_p on $\boldsymbol{\varphi}_p$ in the neighborhood of $\boldsymbol{\varphi}$, as shown in Fig. 4.3(a).

From (4.6) and (4.7), the phase dynamics of the perturbed dynamical system can be expressed as

$$\begin{aligned}\frac{d\phi_p}{d\theta} &= \left.\frac{\partial \phi_p}{\partial \boldsymbol{x}}\right|_{\boldsymbol{x}=\boldsymbol{\varphi}_p(\phi_p)} \cdot \frac{d\boldsymbol{\varphi}_p}{d\theta} \\ &= \left.\frac{\partial \phi_p}{\partial \boldsymbol{x}}\right|_{\boldsymbol{x}=\boldsymbol{\varphi}_p(\phi_p)} \cdot \Big(\boldsymbol{F}(\boldsymbol{x}(\theta)) + \boldsymbol{G}(\Theta)\Big) \\ &= 1 + \left.\frac{\partial \phi_p}{\partial \boldsymbol{x}}\right|_{\boldsymbol{x}=\boldsymbol{\varphi}_p(\phi_p)} \cdot \boldsymbol{G}(\Theta). \end{aligned} \tag{4.8}$$

When the perturbation is small, the deviation of $\boldsymbol{\varphi}_p$ from the original trajectory $\boldsymbol{\varphi}$ is also small. Therefore, $\partial\phi_p/\partial\boldsymbol{x}$, which is included in the right-hand side of (4.8), can be approximated as

$$\left.\frac{\partial \phi_p}{\partial \boldsymbol{x}}\right|_{\boldsymbol{x}=\boldsymbol{\varphi}_p(\phi_p)} \approx \left.\frac{\partial \phi}{\partial \boldsymbol{x}}\right|_{\boldsymbol{x}=\boldsymbol{\varphi}(\phi)} = \boldsymbol{Z}(\phi). \tag{4.9}$$

$\boldsymbol{Z}(\phi)$ is known as the phase sensitivity function (PSF). By substituting (4.9) into (4.8), we can obtain the phase function of the perturbed dynamical system as

$$\frac{d\phi_p}{d\theta} \approx 1 + \boldsymbol{Z}(\phi) \cdot \boldsymbol{G}(\Theta). \tag{4.10}$$

4.3.2 Time Averaging for Simplification

The phase difference between the perturbed limit cycle and the external force is

$$\psi = \phi_p - \Theta. \tag{4.11}$$

By eliminating ϕ_p from (4.10) and (4.11), we can obtain

$$\begin{aligned}\frac{d\psi}{d\theta} &\approx 1 - \frac{d\Theta}{d\theta} + \boldsymbol{Z}(\psi+\Theta) \cdot \boldsymbol{G}(\Theta) \\ &= 1 - \frac{\Omega}{\omega} + \boldsymbol{Z}(\psi+\Theta) \cdot \boldsymbol{G}(\Theta). \end{aligned} \tag{4.12}$$

Because $\Omega/\omega \approx 1$ and $\boldsymbol{G}(\Theta) \ll 1$, the variation of ψ is much slower than that of Θ. Therefore, ψ is regarded as constant during one period of the dynamical system and (4.12) can be simplified by averaging Θ as follows:

$$\begin{aligned}\frac{d\psi}{d\theta} &= 1 - \frac{\Omega}{\omega} + \frac{1}{2\pi}\int_0^{2\pi} \boldsymbol{Z}(\psi + \Theta) \cdot \boldsymbol{G}(\Theta) d\Theta, \\ &= 1 - \frac{\Omega}{\omega} + \Gamma(\psi). \end{aligned} \tag{4.13}$$

4.3.3 Locking Range

When $d\psi/d\theta = 0$, the original oscillator is synchronized with the weak forcing signal. Figure 4.3(b) shows $d\psi/d\theta$ as a function of ψ. If there is at least one solution of $d\psi/d\theta = 0$ for ψ, the phase difference is locked in the steady state. $\Gamma(\psi)$ is a periodic function of ψ because $\boldsymbol{Z}$ and $\boldsymbol{G}$ are the 2π-periodicity functions. As shown in Fig. 4.3(b), $d\psi/d\theta$ has at least one solution for ψ if the $1 - \Omega/\omega$ is in the range of

$$-\Gamma_{max} \le 1 - \frac{\Omega}{\omega} \le -\Gamma_{min}, \tag{4.14}$$

where Γ_{min} and Γ_{max} are the minimum and maximum values of $\Gamma(\psi)$. From (4.14), the locking range is obtained as

$$\Gamma_{min} + 1 \le \frac{\Omega}{\omega} \le \Gamma_{max} + 1. \tag{4.15}$$

$\Gamma(\psi)$ can be obtained by the convolution integral of the PSF and forcing signal as given in (4.13). Therefore, the locking ranges of the injection-locked oscillator can be derived regardless of $\boldsymbol{G}$, particularly injection-signal waveforms, after the PSF is obtained.

4.4 Design of Injection-Locked Class-E Oscillator

4.4.1 Assumptions

For both the free-running class-E oscillator design and the locking-range derivations, it is necessary to formulate the circuit equations of the injection-locked class-E oscillator, which corresponds to (4.7). The circuit equations are based on the following assumptions.

a) The MOSFET is used as a switching device S, which has zero switching times, infinite off resistance, and on resistance r_S.

b) The MOSFET has an equivalent series capacitance and equivalent series resistance (ESR) between the gate and the source of the MOSFET, which are C_g and r_g, respectively.

c) IRF530 MOSFET is used as a switching device S. Table 4.1 gives the IRF530 MOSFET parameters. In this table, V_{th}, r_S, and V_{fFET} were obtained from the FET manual, where V_{fFET} is the permissible maximum gate-source voltage. C_g and r_g were measured by HP 16047A at 1 MHz.

d) All of the inductances L_C, L_0, and L_f have an ESR r_{L_C}, L_{L_0}, and r_{L_f}, respectively.

e) The shunt capacitance C_S includes the MOSFET drain-to-source parasitic capacitances.

f) All of the passive elements including switch-on resistance, MOSFET parasitic capacitances, and ESRs of inductances work as linear elements.

g) The MOSFET turns on at $\theta = 0$ and turns off at $\theta = \pi$ in the free-running operation.

From above assumptions, we have an equivalent circuit of the injection-locked class-E oscillator, as shown in Fig. 4.1(b).

4.4.2 Circuit Equations

From the equivalent circuit in Fig. 4.1(b), the circuit equations are expressed as

$$\begin{cases} \dfrac{R}{V_{DD}}\dfrac{di_{DD}}{d\theta} = \dfrac{R}{\omega L_C}\left(1 - \dfrac{v_S}{V_{DD}} - \dfrac{r_{L_C} i_{DD}}{V_{DD}}\right) \\ \dfrac{1}{V_{DD}}\dfrac{dv_S}{d\theta} = \dfrac{1}{\omega C_S V_{DD}}\left(i_{DD} - \dfrac{v_S}{R_S} - i\right) \\ \dfrac{1}{V_{DD}}\dfrac{dv}{d\theta} = \dfrac{i}{\omega C_0 V_{DD}} \\ \dfrac{R}{V_{DD}}\dfrac{di}{d\theta} = \dfrac{R}{\omega L_0}\dfrac{v_S - v - v_1 - v_2 - r_{L_0} i}{V_{DD}} \\ \dfrac{1}{V_{DD}}\dfrac{dv_1}{d\theta} = \dfrac{1}{\omega C_1 V_{DD}}\left(i - \dfrac{v_1 + v_2}{R}\right) \\ \dfrac{1}{V_{DD}}\dfrac{dv_2}{d\theta} = \dfrac{1}{\omega C_2 V_{DD}}\left(i - \dfrac{v_1 + v_2}{R} - i_f\right) \\ \dfrac{r_g}{V_{DD}}\dfrac{di_f}{d\theta} = \dfrac{r_g}{\omega L_f}\dfrac{v_2 - v_f - r_{L_f} i_f}{V_{DD}} \\ \dfrac{1}{V_{DD}}\dfrac{dv_g}{d\theta} = \dfrac{1}{\omega C_g r_g\left(\dfrac{1}{r_g} + \dfrac{1}{R_{d1}} + \dfrac{1}{R_{d2}} + \dfrac{1}{R_{inj}}\right)}\left\{\dfrac{i_f}{V_{DD}} + \dfrac{1}{R_{d1}}\right. \\ \qquad \left. + \dfrac{1}{R_{inj}}\dfrac{v_{inj} - v_{C_{inj}}}{V_{DD}} - \dfrac{v_g}{V_{DD}}\left(\dfrac{1}{R_{d1}} + \dfrac{1}{R_{d2}} + \dfrac{1}{R_{inj}}\right)\right\} \\ \dfrac{1}{V_{DD}}\dfrac{dv_{Cinj}}{d\theta} = \dfrac{v_{inj} - v_{Cinj} - v_f}{\omega C_{inj} R_{inj} V_{DD}} \\ v_f = v_g + \omega C_g r_g \dfrac{dv_g}{d\theta}. \end{cases} \tag{4.16}$$

In (4.16), R_S is the equivalent resistance of the switch. According to the assumption a) and f), R_S is expressed as

$$R_S = \begin{cases} r_S & \text{for } (V_{th} - v_f) \le 0 \\ \infty & \text{for } (V_{th} - v_f) > 0 \end{cases} \tag{4.17}$$

Now, $\boldsymbol{x} \in \boldsymbol{R}^9$ and $\boldsymbol{G} \in \boldsymbol{R}^9$ are defined as

$$\boldsymbol{x}(\theta) = \\ \frac{1}{V_{DD}}[Ri_{DD}(\theta), v_S(\theta), v(\theta), Ri(\theta), v_1(\theta), v_2(\theta), r_g i_f(\theta), v_g(\theta), v_{C_{inj}}(\theta)]^T \tag{4.18}$$

and

$$\boldsymbol{G}(\Theta) = \frac{v_{inj}}{V_{DD}}[0,0,0,0,0,0,g_1,g_2,g_3]^T, \tag{4.19}$$

where

$$g_1 = -\frac{r_g}{\omega L_f R_{inj}\left(\frac{1}{r_g}+\frac{1}{R_{d1}}+\frac{1}{R_{d2}}+\frac{1}{R_{inj}}\right)}, \tag{4.20}$$

$$g_2 = \frac{1}{\omega C_g r_g R_{inj}\left(\frac{1}{r_g}+\frac{1}{R_{d1}}+\frac{1}{R_{d2}}+\frac{1}{R_{inj}}\right)}, \tag{4.21}$$

and

$$g_3 = \frac{1}{\omega C_{inj} R_{inj}}\left[1-\frac{1}{R_{inj}\left(\frac{1}{r_g}+\frac{1}{R_{d1}}+\frac{1}{R_{d2}}+\frac{1}{R_{inj}}\right)}\right]. \tag{4.22}$$

Using $\boldsymbol{x}$ and $\boldsymbol{G}$, (4.16) is expressed as

$$\frac{d\boldsymbol{x}(\theta)}{d\theta} = \boldsymbol{F}(\boldsymbol{x}(\theta)) + \boldsymbol{G}(\Theta), \tag{4.23}$$

which corresponds to (4.7).

In this study, numerical waveforms are obtained by solving the differential equations with the forth-order Runge-Kutta method.

4.4.3 Free-Running Class-E Oscillator Design

The design specifications for the design example are given as follows: operating frequency $f = 1$ MHz, input voltage $V_{DD} = 12$ V, output quality factor $Q = \omega L_0/R = 5$, output resistance $R = 25\ \Omega$, RMS voltage across the output resistance $V_o = 9$ V, ratio of the output resonant inductance to the DC-feed inductance $L_0/L_C = 0.1$, $V_{fmax} = 15$ V, $R_{inj} = 2$ kΩ, and $C_{inj} = 0.1\ \mu$F. Because $V_{th} = 3$ V and $V_{DD} = 12$ V, $R_{d1} = 750$ kΩ and $R_{d2} = 250$ kΩ. Additionally, $r_S = 0.16\ \Omega$, $C_g = 1.78$ nF, and $r_g = 2.17\ \Omega$ were obtained as given in Table 4.1, and all of the ESRs of the inductances are zero in the design process.

The class-E free-running oscillator for achieving the class-E ZVS/ZDS conditions can be obtained, as given in Table 4.2, by following design methods previously reported [5], [8]. It should be noted that $v_{inj} = 0$ is given for the free-running oscillator design.

Figure 4.4 shows the numerical and experimental waveforms of the free-running class-E oscillator, and Table 4.2 gives the measurement results. All experimental element values were measured using a HP4284A LCR meter, and the voltages and currents were measured using a Agilent 3458A multimeter. The parasitic capacitance of the IRF530 MOSFET was estimated to be 270 pF, which was obtained from a previous study [34]. Figure 4.4 and Table 4.2 show that the experimental results quantitatively agreed with the numerical predictions. In the free-running oscillator, the free-running frequency is 1.0077 MHz, which was measured by the multimeter.

4.5 Derivation of Locking Ranges

In this section, the locking ranges for the injection-locked class-E oscillator are estimated on the basis of PRT.

4.5.1 Definition of Impulse Sensitivity Function and Linear Response Region

For deriving the locking ranges, it is necessary to obtain the PSF as stated in Sect. 4.3 because $\Gamma(\psi)$ is obtained by the convolution integral of the PSF and the injection signal. The PSF can be regarded as the impulse response of the phase [18], [20], [21], [23], [28]. In the proposed locking-range derivation method, the PSF is obtained numerically.

It is assumed that the free-running class-E oscillator is in the steady state because the phase in (4.7) is defined in the steady-state. An impulsive voltage perturbation can be injected at any phase of the one-cycle oscillation. Figure 4.5 shows an example of the trajectory when the impulse perturbation is injected at $\phi = \phi_i$. After injecting the pulse waveform, the waveforms return to the steady state via transient response. However, a phase shift $\Delta\phi$ remains, as shown in Fig. 4.5. In particular, the phase shift $\Delta\phi$ is expressed as a function of the injection phase ϕ_i. This function is known as the impulse sensitivity function (ISF) [18], [20], [21], [23], [28]. The ISF is apparently equivalent to the PSF because the PSF represents the phase gradient on the limit cycle of the oscillator $\partial\phi/\partial\boldsymbol{x}$. When the ISF is determined numerically, the injection-pulse width w_p and height h_p are important because the phase shift depends on the impulse-perturbation injection phase ϕ_i in addition to the pulse shape. If the pulse is narrow and low, the phase shift is in proportion to the pulse area. The region where $\Delta\phi$ is in proportion to h_p/V_{DD} is defined as the linear response region (LRR). When the ISF is obtained in this region, it is uniquely determined by normalizing the phase shift by the pulse area.

$\Gamma(\psi)$ is obtained from

$$\Gamma(\psi) = \frac{1}{2\pi}\int_0^{2\pi} Z_0(\psi + \Theta) \cdot \frac{v_{inj}(\Theta)}{V_{DD}} d\Theta, \tag{4.24}$$

where $Z_0(\phi_i)$ is the ISF.

4.5.2 Numerical Derivation of ISF

Figure 4.6 shows $\Delta\phi$ as a function of the impulse amplitude for $\phi_i = 0$ and $\omega = 0.002{\cdot}2\pi$. In particular, the injection voltage v_{inj}/V_{DD} is

$$\frac{v_{inj}}{V_{DD}} = \begin{cases} \dfrac{h_p}{V_{DD}}, & \text{for } \phi_i \le \theta < w_p \\ 0. & \text{for other} \end{cases} \tag{4.25}$$

The pulse-shape waveforms were injected at the instant of switch turn-on ($\phi_i = \theta = 0$), and the phase shifts through the transient state with 5000 periods was plotted. It was confirmed that 5000 periods are sufficiently long for the oscillator to be in the steady state. It is seen from the extended region in Fig. 4.6 that the phase shift varies linearly with the pulse height. From this figure, the impulse signal that has $h_p/V_{DD} = 0.833$, particularly $h_p = 10$ V, and $w_p = 0.002 \cdot 2\pi$ is used for the ISF derivation.

Figure 4.7 shows the ISF of the designed class-E oscillator. The ISF is defined as the phase shift by applying a unit impulse as a function of injection point. It is ensured that the phase shift is in proportion to the pulse area because it is in the LRR, as shown in Fig. 6. Therefore, the ISF is obtained from

$$Z_0(\phi_i) = \frac{\Delta\phi}{\dfrac{h_p}{V_{DD}} \cdot w_p}. \tag{4.26}$$

It is seen in Fig. 4.7 that a discontinuous point appears at $\phi_i = \pi$, particularly switch turn-off instant, because there was a jump in the switch current at the turn-off instant, as shown in Fig. 4.2. In contrast, Z_0 at $\phi_i = 2\pi$, particularly turn-on instant, was continuous, as shown in Fig. 4.7. This is because the class-E ZVS/ZDS conditions, which are given in (1), were achieved. Because of these conditions, both the switch current and voltage waveforms were continuous at $\theta = 2\pi$.

4.5.3 Locking Ranges of Designed Oscillator

The locking ranges of the class-E oscillator for three types of injection signals v_{inj}, which are sinusoidal, rectangular, and triangle waveform signals, are predicted. The injection signals are expressed as

1. sinusoidal wave

$$\frac{v_{inj}}{V_{DD}} = \frac{V_s}{V_{DD}} \sin\Theta, \tag{4.27}$$

2. rectangular wave

$$\frac{v_{inj}}{V_{DD}} = \begin{cases} \dfrac{V_r}{V_{DD}}, & \text{for } 0 \le \Theta < \pi \\ 0, & \text{for } \pi \le \Theta < 2\pi \end{cases} \tag{4.28}$$

and

3. triangle wave

$$\frac{v_{inj}}{V_{DD}} = \begin{cases} \dfrac{2V_t}{\pi V_{DD}}\Theta, & \text{for } 0 \le \Theta < \dfrac{\pi}{2} \\ \dfrac{V_t}{V_{DD}} - \dfrac{2V_t}{\pi V_{DD}}\left(\Theta - \dfrac{\pi}{2}\right), & \text{for } \dfrac{\pi}{2} \le \Theta < \dfrac{3\pi}{2} \\ \dfrac{-V_t}{V_{DD}} + \dfrac{2V_t}{\pi V_{DD}}\left(\Theta - \dfrac{3\pi}{2}\right), & \text{for } \dfrac{3\pi}{2} \le \Theta < 2\pi \end{cases} \tag{4.29}$$

where V_s, V_r, and V_t are the peak values of each waveforms.

$\Gamma(\psi)$ can be obtained numerically by the convolution integral of the ISF shown in Fig. 4.7 and the injection signal. For the numerical calculations, the 50th order Fourier expansion of the ISF is applied to the convolution integral calculations with the injection waveforms, which provides an accurate approximation.

Figure 4.8 shows the locking ranges of the designed injection-locked class-E oscillator for each injection waveform. It is shown in (4.24) that $\Gamma(\psi)$ varies linearly with the injection signal. Therefore, the theoretical locking ranges increase in proportion to the peak voltage of the injection voltages. The numerical results in Fig. 4.8 were obtained by the calculation algorithm in [14]. It is shown in Fig. 4.8 that the theoretical locking ranges quantitatively agree with the experimental and the numerical ranges, regardless of injection-signal waveforms, which validates the effectiveness and usefulness of the locking-range predictions based on PRT. Because (4.15) and (4.16) are normalized by the free-running frequency, it can be stated that the locking ranges in Fig. 4.8 are independent of the specified operating frequency.

Figure 4.8(a) also shows the analytical locking range from a previous study [13] based on Adler's equation [16]. It can be stated that the proposed locking-range prediction method gives more accurate locking ranges than the values from the analytical method [13]. Compared with the analytical derivation method of locking ranges [13], [32], [33], the numerical derivation method presented in this chapter includes the following advantages: (1) When the circuit equations are formulated, the locking ranges can be estimated following the similar calculations steps presented in this chapter. In particular, the proposed method can be adapted to any practical oscillators with many variables. In addition, the accurate locking ranges can be obtained by formulating circuit model in detail. (2) Locking ranges on any injection-signal waveform can be efficiently obtained because the ISF is independent of the injection-signal waveform.

Figure 4.9 shows the output power and power conversion efficiency as a function of frequency ratio for the sinusoidal-wave injection at $V_s/V_{DD} = 0.25$ ($V_s = 3.0$ V). For obtaining the numerical results in Fig. 4.9, the ESRs of the inductances given in Table 4.2 were considered. In this figure, it is shown that a power conversion efficiency of more than 93 % can be kept in all locking ranges. This is because the injection signal does not affect the switch-voltage waveform, and the class-E ZVS/ZDS conditions can be achieved. Figure 4.10 shows the numerical and measured waveforms for $\Omega = 0.99551\omega$ and $\Omega = 1.00449\omega$ at $V_s = 3$ V. It is shown in the figure that the class-E ZVS/ZDS conditions were satisfied in both numerical and measured switch-voltage waveforms. The figure also shows that the oscillation frequencies were locked with the injection-signal frequencies in both Fig. 4.10(a) and (b). Additionally, it was confirmed that the phase shift between v_{inj} and i_f, particularly ψ in Fig. 4.10(a), is different from that in Fig. 4.10(b).

4.6 Conclusion

This chapter has presented the numerical derivation method of the locking range for the injection-locked class-E oscillator using PRT. It is possible to obtain the locking ranges on any injection-signal waveform accurately from PRT with low computation cost. The predicted locking ranges from the proposed locking-range derivation method quantitatively agree with those obtained from the simulations and circuit experiments, which shows the validity of this method.

Table 4.1: IRF530 MOSFET model used in design

Threshold voltage V_{th}	3 V
Switch on resistance r_S	0.16 Ω
Equivalent series capacitance C_g	1.78 nF
Equivalent series resistance r_g	2.17 Ω
Maximum gate-source voltage V_{fFET}	20 V

Table 4.2: Design values of injection-locked class-E oscillator

	Calculated	Measured	Differences
L_C	199 μH	214 μH	7.5 %
L_0	19.9 μH	19.9 μH	-0.20 %
L_f	16.5 μH	16.5 μH	-0.36 %
C_S	1.50 nF	1.46 nF	-2.5 %
C_0	1.75 nF	1.74 nF	-0.68 %
C_1	1.80 nF	1.79 nF	-0.83 %
C_2	17.3 nF	17.4 nF	-0.38 %
R	25.0 Ω	25.0 Ω	-0.090 %
R_{d1}	750 kΩ	752 kΩ	0.20 %
R_{d2}	250 kΩ	249 kΩ	-0.21 %
r_{L_C}	-	0.0100 Ω	-
r_{L_0}	-	0.503 Ω	-
r_{L_f}	-	0.400 Ω	-
R_{inj}	2 kΩ	1.98 kΩ	-0.80 %
C_{inj}	0.100 μF	0.101 μF	1.4 %
f_{free}	1 MHz	1.0077 MHz	0.77 %
V_{DD}	12.0 V	12.0 V	0.0 %
V_o	9.0 V	8.80 V	-2.2 %
I_{DD}	0.277 A	0.278 A	0.36 %

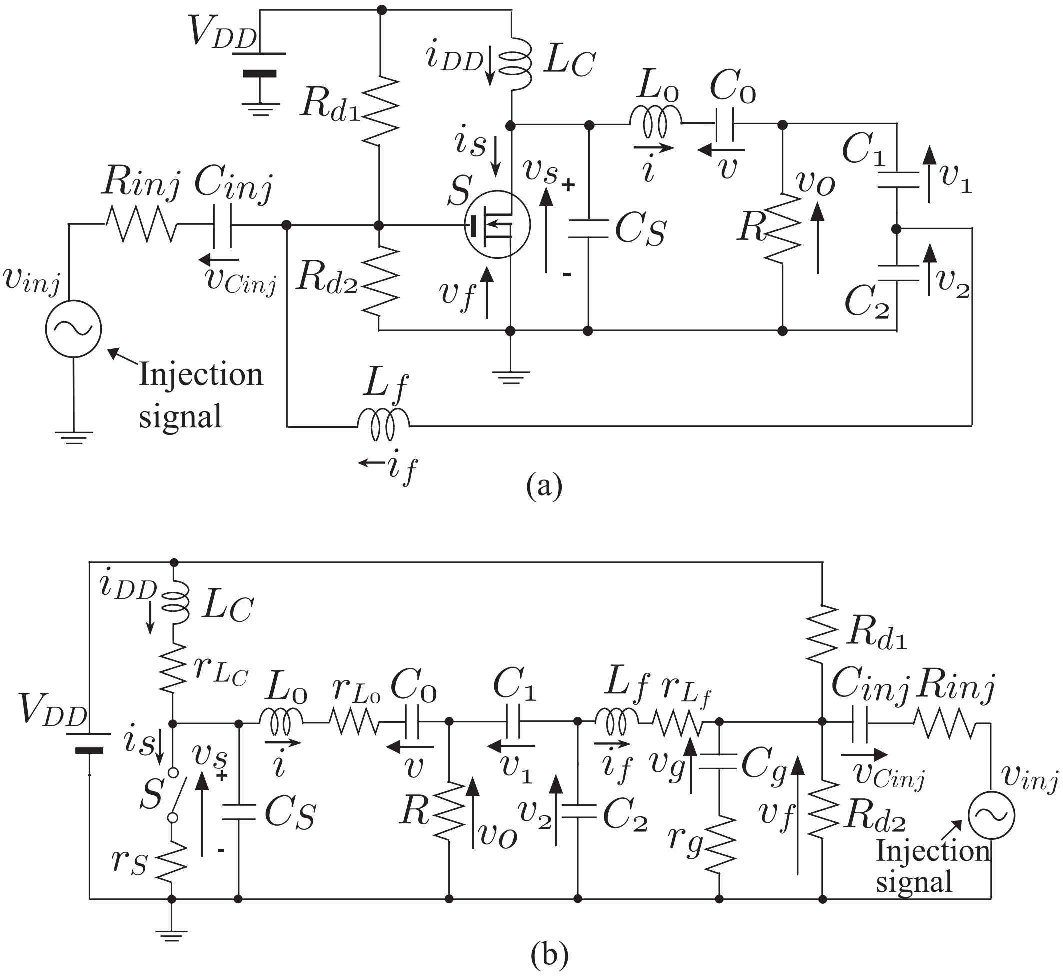

Figure 4.1: Circuit descriptions. (a) Injection-locked class-E oscillator. (b) Equivalent circuit.

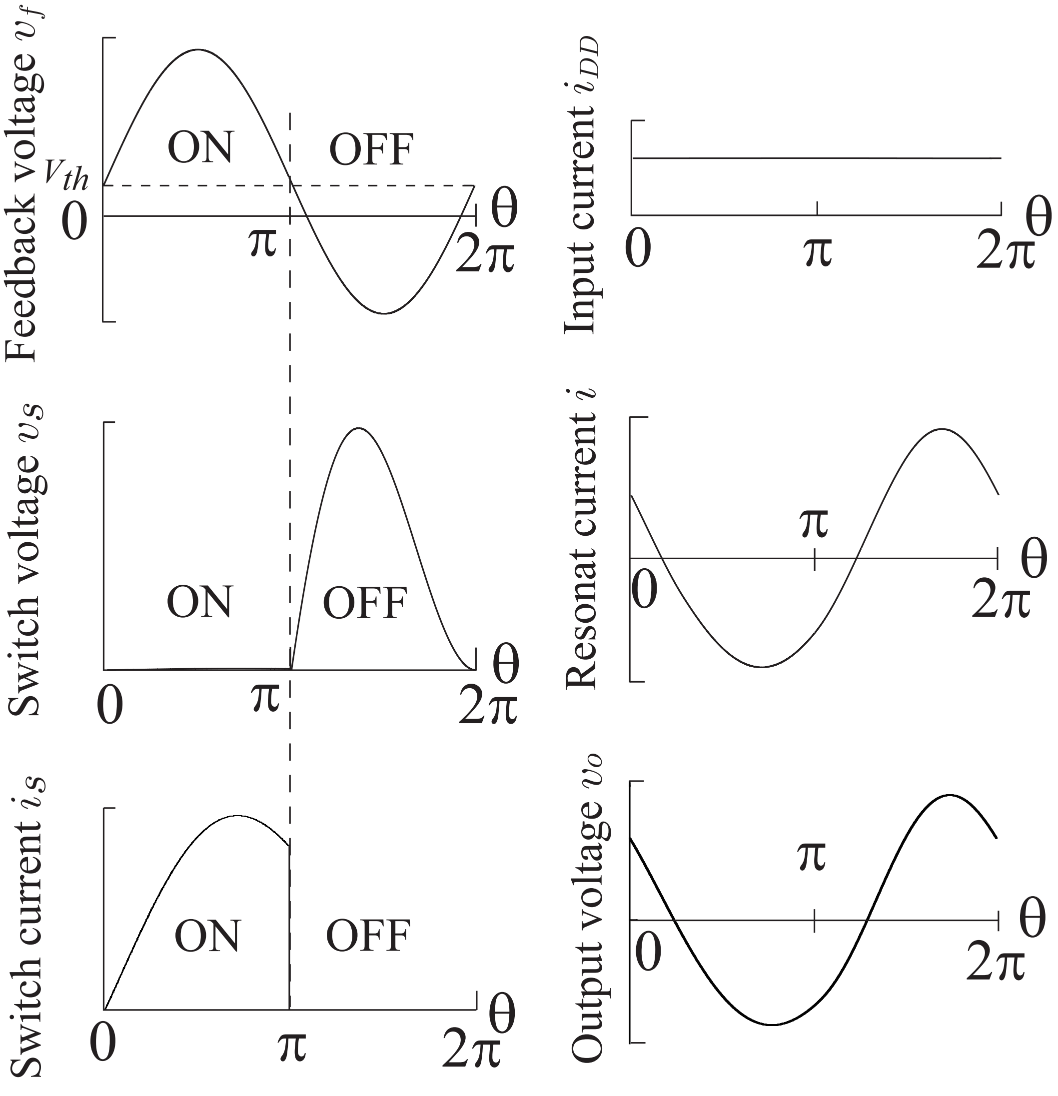

Figure 4.2: Nominal waveforms of free-running class-E oscillator.

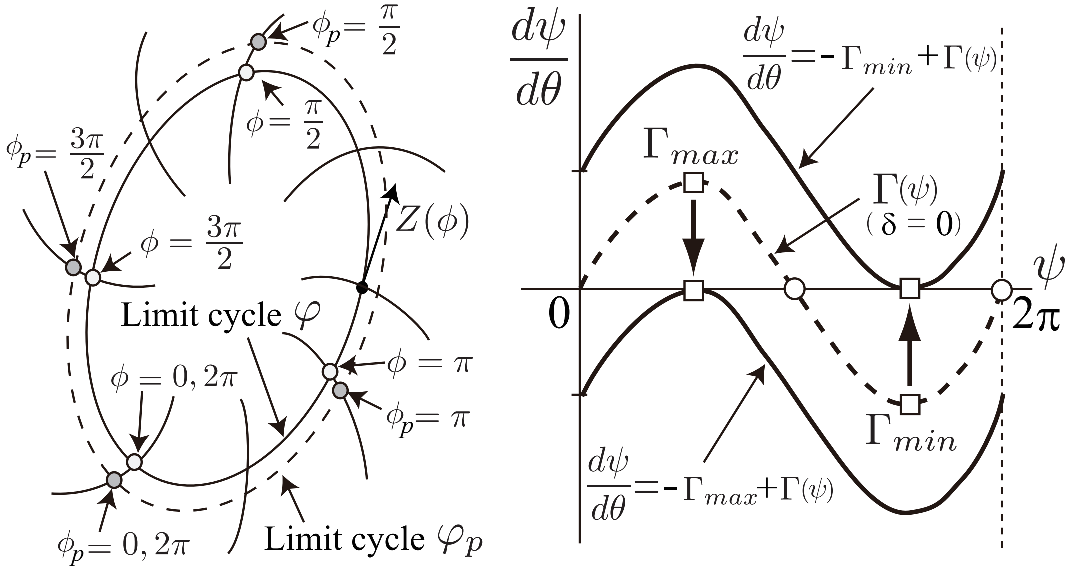

(a) (b)

Figure 4.3: Example of oscillator dynamics. (a) Limit cycle. (b) $d\psi/dt$ versus ψ.

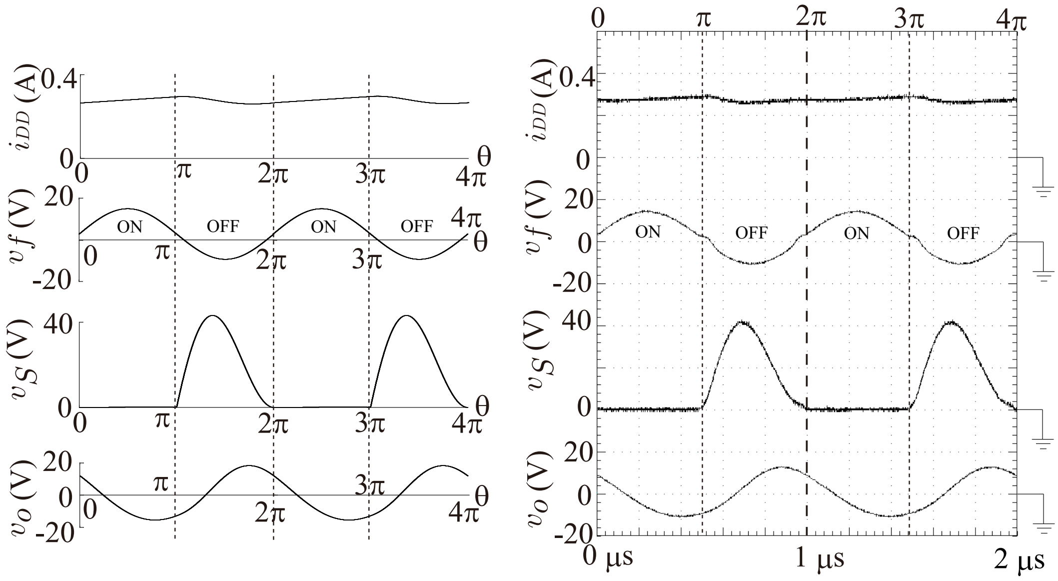

(a) (b)

Figure 4.4: Waveforms of designed injection-locked class-E oscillator. (a) Numerical waveforms. (b) Experimental waveforms.

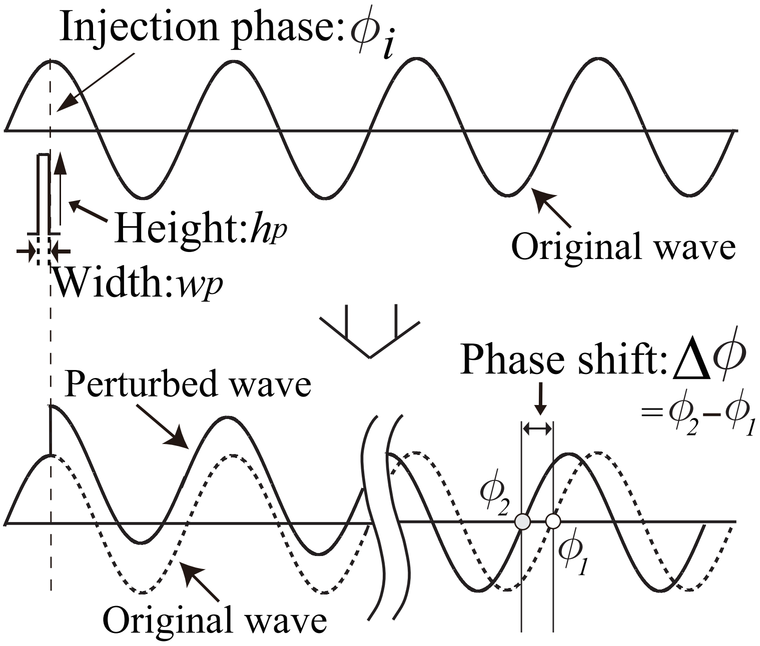

Figure 4.5: Phase shift due to impulse perturbation at ϕ_i.

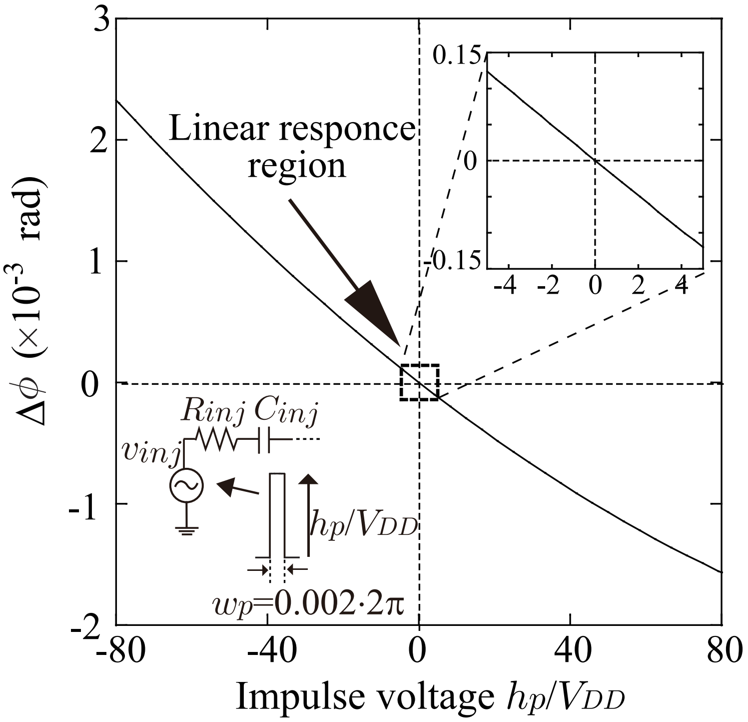

Figure 4.6: $\Delta\phi$ of the designed injection-locked class-E oscillator for $\phi_i = 0$.

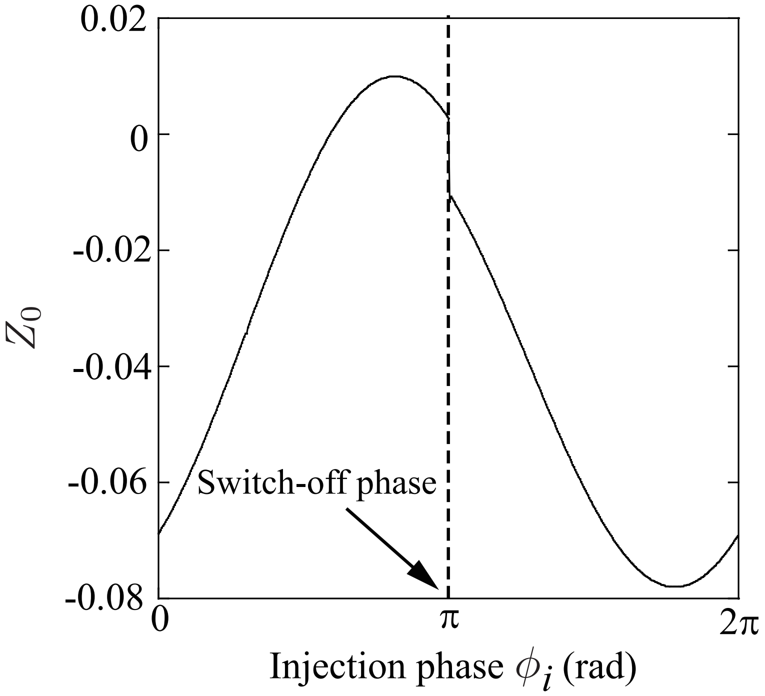

Figure 4.7: Impulse sensitivity function (ISF) of the designed injection-locked class-E oscillator.

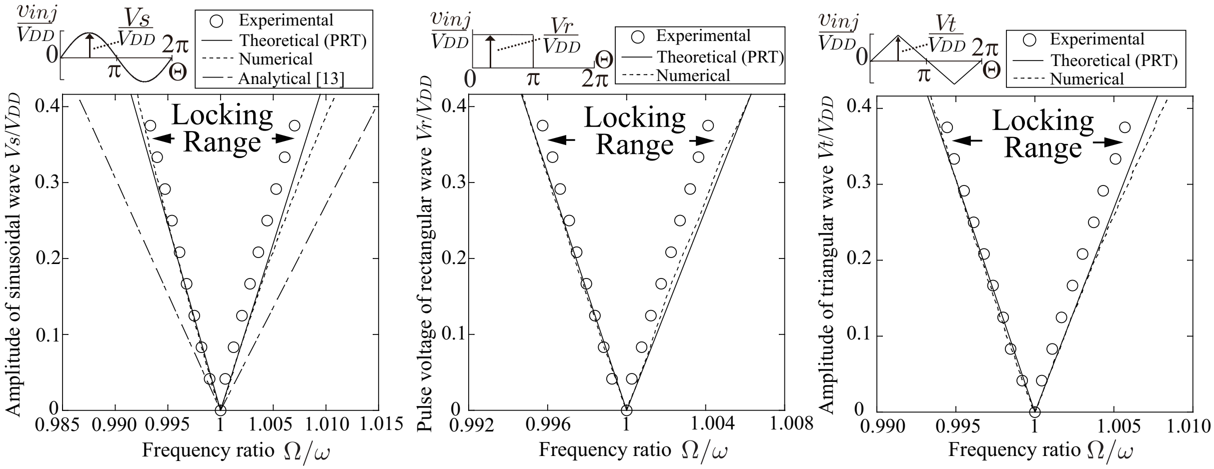

(a) (b) (c)

Figure 4.8: Experimental, calculated (phase reduction theory; PRT), and numerical locking ranges. (a) Sinusoidal-wave injection. (b) Rectangular-wave injection. (c) Triangular-wave injection.

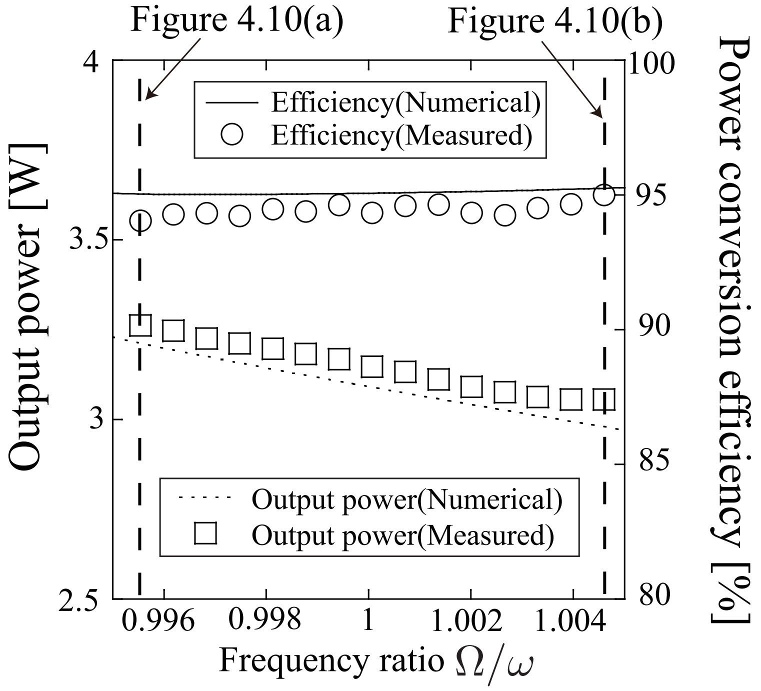

Figure 4.9: Experimental and numerical output power and power conversion efficiency in the locking range of the sinusoidal-wave injection at $V_s/V_{DD} = 0.250$.

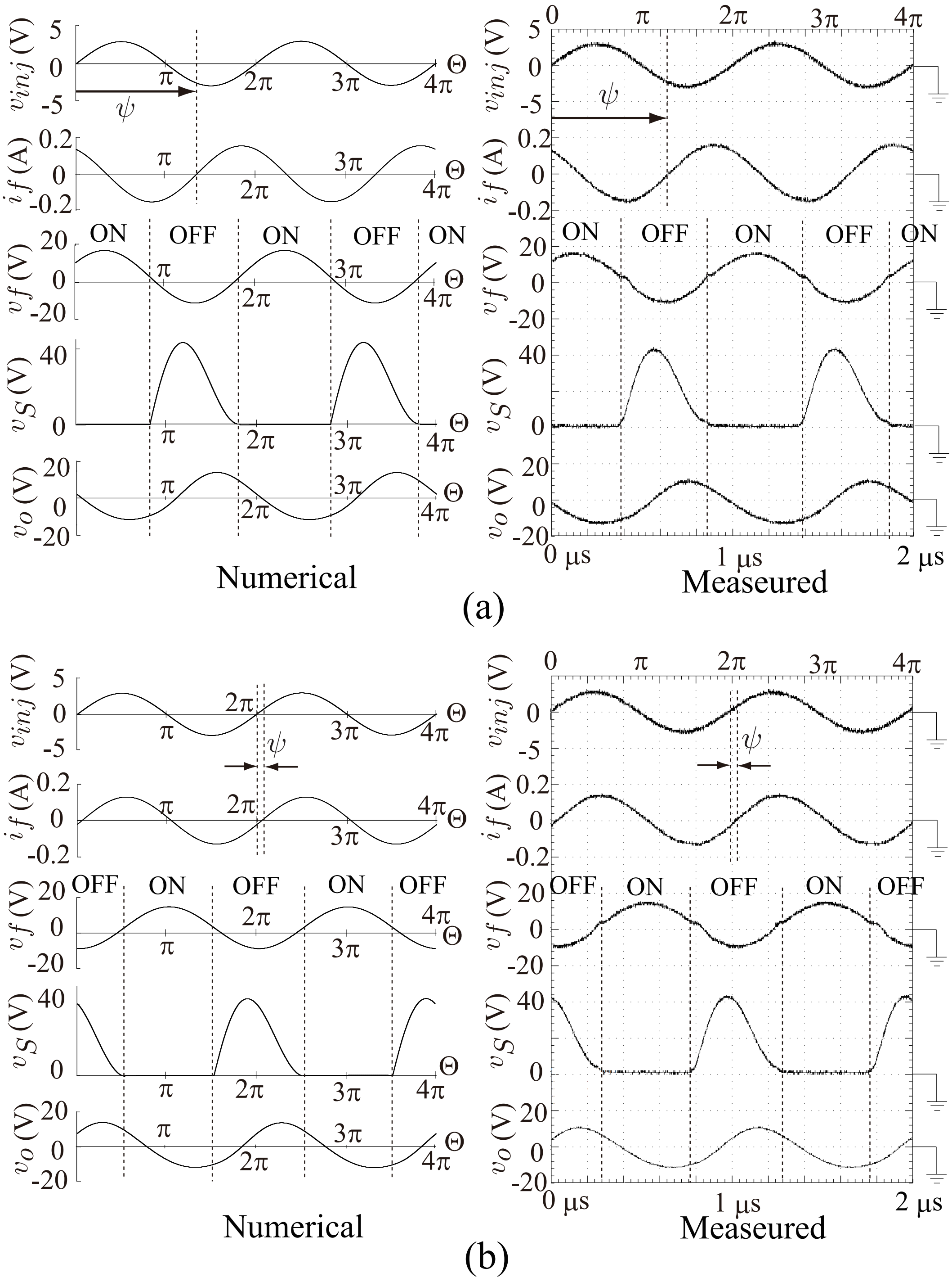

Figure 4.10: Waveforms at $V_s = 3$ V for (a) $\Omega = 0.99551\omega$ and (b) $\Omega = 1.00449\omega$.

References

[1] D. Ahn and S. Hong, “Class-D CMOS oscillators,” *IEEE J. Solid-State Circuits*, vol. 48, no. 12, pp. 3105–3119, Dec. 2013.

[2] J. Ebert and M. Kazimierczuk, “Class E high-efficiency tuned power oscillator,” *IEEE J. Solid-State Circuits*, vol. SC-16, no. 2, pp. 62–66, Apr. 1981.

[3] D. V. Chernov, M. K. Kazimierczuk, and V. G. Krizhanovski, “Class-E MOSFET low-voltage power oscillator,” *in Proc. IEEE ISCAS*, Phoenix, AZ, vol. 5, May 2002, pp. 509–512.

[4] M. K. Kazimierczuk, V. G. Krizhanovski, J. V. Rassokhina, and D. V. Chernov, “Class-E MOSFET tuned power oscillator design procedure,” *IEEE Trans. Circuits Syst. I,* vol. 52, no. 6, pp. 1138–1147, Jun. 2005.

[5] H. Hase, H. Sekiya, J. Lu, and T. Yahagi, “Novel design procedure for MOSFET class-E oscillator,” *IEICE Trans. Fund.,* vol. E87-A, no. 9, pp. 2241–2247, Sep. 2004.

[6] V. G. Krizhanovski, D. V. Chernov, and M. K. Kazimierczuk, “Low-voltage electronic ballast based on class E oscillator,” *IEEE Trans. Power Electron.* vol. 22, no. 3, pp. 863–870, May 2007.

[7] L. R. Nerone, “Novel self-oscillating class E ballast for compact fluorescent lamps,” *IEEE Trans. Power Electron.* vol. 16, no. 2, Mar. 2001.

[8] H. Hase, H. Sekiya, J. Lu, and T. Yahagi, “Resonant dc/dc converter with class E oscillator,” *IEEE Trans. Circuits Syst. I,* vol. 53, no. 9, pp. 2025–2035, Sept. 2006.

[9] T. Andersen, S. K. Christensen, A. Knott, and M. A. E. Andersen, “A VHF class E DC-DC converter with self-oscillating gate driver,” *in Proc. IEEE APEC,* Fort Worth, TX, Mar. 2011, pp. 885–891.

[10] C. M. Zierhofer and E. S. Hochmair, "High-efficiency coupling-insensitive transcutaneous power and data transmission via an inductive link," *IEEE Trans. Bio. Eng.,* vol. 37, no. 7, pp. 716–722, Jul. 1990.

[11] M. Qingyun, M. R. Haider, Y. Song, and S. K. Islam, "Power-oscillator based high efficiency inductive power-link for transcutaneous power transmission," *in Proc. IEEE MWSCAS*, Seattle, WA, Aug. 2010, pp. 537–540

[12] F. Ellinger, U. Lott, and W. Bachtold, "Design of a low-supply-voltage high-efficiency Class-E voltage-controlled MMIC oscillator at C-band," *IEEE Trans. Microw. Theory Tech.,* vol. 49, no. 1, pp. 203–206, Jan. 2001.

[13] M. K. Kazimierczuk, V. G. Krizhanovski, J. V. Rassokhina, and D. V. Chernov,"Injection-locked class-E oscillator," *IEEE Trans. Circuits Syst. I,* vol. 53, no. 6, pp. 1214–1222, Jun. 2006.

[14] T. Nagashima, X. Wei, H. Tanaka, and H. Sekiya, "Numerical derivations of locking ranges for injection-locked class-E oscillator," *in Proc. IEEE PEDS,* Kitakyushu, Japan, Apr. 2013, pp. 1021–1024.

[15] M. Matsuo, H. Sekiya, T. Suetsugu, K. Shinoda, and S. Mori, "Design of a high-efficiency class DE tuned power oscillator," *IEEE Trans. Circuits Syst. I,* vol. 47, no. 11, pp. 1645–1649, Nov. 2000.

[16] R. A. Adler, "Study of locking phenomena in oscillators, " in *Proc. IRE,* Jun. 1946, vol. 34, no. 6, pp. 351–357.

[17] A. Mirzaei, M. E. Heidari, R. Bagheri, S. Chehrazi, and A. A. Abidi, "The quadrature LC oscillator: a complete portrait based on injection locking," *IEEE J. Solid-State Circuits,* vol. 42, no. 9, pp. 1916–1932, Sept. 2007.

[18] P. Maffezzoni, “Analysis of oscillator injection locking through phase-domain impulse-response,” *IEEE Trans. Circuits Syst. I*, vol. 55, no. 5, pp. 1297–1305, Jun. 2008.

[19] C. T. Chen, T. S. Horng, K. C. Peng, and C. J. Li, “High-gain and high-efficiency EER/Polar transmitters using injection-locked oscillators,” *IEEE Trans. Microw. Theory Tech.,* vol. 60, no. 12, pp. 4117–4128, Dec. 2012.

[20] D. Dunwell and A. C. Carusone, “Modeling oscillator injection locking using the phase domain response,” *IEEE Trans. Circuits Syst. I,* vol. 60, no. 11, pp. 2823–2833, Nov. 2013.

[21] P. Maffezzoni, “Nonlinear phase-domain macromodeling of injection-locked frequency dividers,” *IEEE Trans. Circuits Syst. I,* vol. 60, no. 11, pp. 2878–2887, Nov. 2013.

[22] P. Bhansali and J. Roychowdhury, “Gen-Adler: The generalized Adler’s equation for injection locking analysis in oscillators,” *in Proc. ASP-DAC,* Yokohama, Japan, Jan. 2009, pp. 522–527.

[23] A. Hajimiri and T. H. Lee, “A general theory of phase noise in electrical oscillators,” *IEEE J. Solid-State Circuits,* vol. 33, no. 2, pp. 179–194, Feb. 1998.

[24] Y. Kuramoto, *Chemical Oscillations, Waves, and Turbulence.* New York: Springer-Verlag, 1984.

[25] A. T. Winfree, *The Geometry of Biological Time.* New York: Springer, 1980.

[26] A. Pikovsky, M. Rosenblum, and J. Kurths, *Synchronization: A Universal Concept in Nonlinear Sciences* Cambridge, U. K.: Cambridge Univ. Press, 2001.

[27] S. Boccaletti, J. Kurths, G. Osipov, D. L. Valladares, and C. S. Zhou, “The synchronization of chaotic systems,” *Phys. Rep.,* vol. 366, no. 1/2, pp. 1–101, Aug. 2002.

[28] H. Tanaka, A. Hasegawa, H. Mizuno, and T. Endo, “Synchronizability of distributed clock oscillators,” *IEEE Trans. Circuits Syst. I,* vol. 49, no. 9, pp. 1271–1278, Sept. 2002.

[29] M. Bonnin, F. Corinto, and M. Gilli, “A phase model approach synchronization analysis of coupled nonlinear oscillators,” *in Proc. ECCTD*, Antalya, Turkey, Aug. 2009, pp. 335–338.

[30] M. Bonnin, F. Corinto, and M. Gilli, “Phase model reduction and synchronization of nonlinear oscillators by a periodic force,” *in Proc. ISCAS*, Paris, France, May 2010, pp. 3385–3388.

[31] M. Bonnin and F. Corinto, “Phase noise and noise induced frequency shift in stochastic nonlinear oscillators,” *IEEE Trans. Circuits Syst. I*, vol. 60, no. 8, pp. 2104–2115, Aug. 2013.

[32] A. Buonomo and A. L. Schiavo, “Analytical approach to the study of injection-locked frequency dividers,” *IEEE Trans. Circuits Syst. I,* vol. 60, no. 1, pp. 51–62, Jan. 2013.

[33] A. Buonomo, A. L Schiavo, M. A. Awan, M. S. Asghar, and M. P. Kennedy, “A CMOS injection-locked frequency divider optimized for divide-by-two and divide-by-three operation,” *IEEE Trans. Circuits Syst. I,* vol. 60, no. 12, pp. 3126–3135, Dec. 2013.

[34] T. Suetsugu and M. K. Kazimierczuk, “Comparison of class-E amplifier with nonlinear and linear shunt capacitance,” *IEEE Trans. Circuits Syst. I,* vol. 50, No. 8, pp. 1089–1097, Aug. 2003.

Chapter 5

Analysis and Design of Loosely Inductive Coupled Wireless Power Transfer With Class-E^2 DC-DC Converter

●● ABSTRACT ●●

This chapter presents analytical expressions and a design procedure for the loosely inductive coupled WPT systems with the class-E^2 dc-dc converter. By using the analytical expressions, it is possible to obtain component values of the class-E^2 WPT system for achieving high power-delivery efficiency. The analytical predictions agree with the PSpice-simulation and experimental results quantitatively, which showed the validities of the analytical expressions and design procedure.

5.1 Introduction

Recently, wireless power transfer (WPT) systems have received considerable attentions [1]-[17]. Loosely inductive coupling (LIC) is one of the coupling states for WPT systems and it has been widely used for a variety of applications, such as wireless battery charging for electric vehicles [5], bio-medical implants [6], and so on. For achieving high power-delivery efficiency, it is important to design not only a low power-loss LIC, but also a high power-conversion-efficiency dc-ac inverter and an ac-dc rectifier. For achieving high power-conversion efficiency, the class-E inverter [18]-[23] or the class-DE inverter [24], [25] was applied in the inverter part of the WPT systems [7]-[13]. Because of the class-E zero-voltage switching and zero-derivative switching (ZVS/ZDS) conditions [18], the class-E and -DE inverters can achieve high power-conversion efficiency at high frequencies. In [7]-[13], [24], and [25], however, the power-conversion-efficiency enhancement of the rectifier was not considered.

The class-E^2 dc-dc converter [26]-[28], which consists of the class-E inverter and the class-E rectifier [17], [29]-[31], is one of the resonant dc-dc converters achieving high power-conversion efficiency at high frequencies. This is because both the inverter and the rectifier satisfy the class-E ZVS/ZDS conditions. The WPT systems with the class-E^2 dc-dc converter and its numerical design procedure have been presented in [14] and [16]. Because of the numerical design approach, the class-E^2 WPT system can be designed with no system analysis and no impedance-matching consideration. Accurate component values for achieving the class-E ZVS/ZDS conditions can be obtained by the numerical design procedure. However, further power-delivery efficiency enhancement has never been considered in the numerical design procedure. This is because it is difficult to comprehend the relationships among component values and system performance such as power-delivery efficiency from the numerical designs. The analytical design approach may cultivate designer's fundamental understanding and intuition of WPT system designs compared with the numerical design approach.

This chapter presents analytical expressions and a design procedure for the LIC-WPT system with class-E^2 dc-dc converter. By using the analytical expressions, it is possible to obtain component values of the class-E^2 WPT system for achieving the class-E ZVS/ZDS conditions. Additionally, the analytical expressions suggest designers how to determine the component values for power-delivery efficiency enhancement. I propose that component values of the rectifier are used for the power-delivery efficiency enhancement and the output power is adjusted by the inverter component values. The analytical predictions agree with the PSpice-simulation and experimental results quantitatively, which showed the validities of the analytical expressions and the design procedure. In the laboratory experiment, the WPT system for 10 cm coil distance achieved 77.1 % power-delivery efficiency with 10 W (50 Ω/22.4 V) output power at 1 MHz operating frequency.

5.2 Class-E^2 DC-DC Converter

Figure 5.1 shows a topology of the class-E^2 dc-dc converter [26]-[28], which consists of the class-E inverter [18]-[23] and the class-E rectifier [17], [29]-[31]. Figure 5.2 shows example waveforms of the class-E^2 dc-dc converter, where $\theta = 2\pi f t = \omega t$ is the angular time and f is the operating frequency. Because both the class-E inverter and the class-E rectifier satisfy the class-E ZVS/ZDS conditions, the class-E^2 dc-dc converter can achieve high power conversion efficiency at high frequencies with low level of EMI/RFI.

5.2.1 Class-E Inverter

The class-E inverter consists of input voltage V_I, dc-feed inductance L_C, MOSFET S as a switching device, shunt capacitance C_S, and series resonant network $C_r - L_r$ as shown on the left-hand side of Fig. 5.1. If the dc-feed inductance L_C is large, the input current I_I of the inverter is approximately constant as shown in Fig. 5.2. If the loaded quality factor Q of the resonant network is high, the current through the resonant network i_{inv} has a sinusoidal waveform. The MOSFET is driven by the driving signal v_g. When the switch is in on-state, the voltage across the switch is approximately zero and the switch current i_S flows through the MOSFET as shown in Fig. 5.2. During the switch-off interval, the difference of currents through the dc-feed inductance and the resonant filter, which is expressed as $i_{C_S} = \omega C_S dv_S/d\theta$, flows through the shunt capacitance. The current through the shunt capacitance produces the pulse-shape switch voltage as shown in Fig. 5.2. The most important operation of the class-E inverter is the operation under the class-E ZVS/ZDS conditions at turn-on instant, which are expressed as

$$v_S(2\pi) = 0 \quad \text{and} \quad \left.\frac{dv_S}{d\theta}\right|_{\theta=2\pi} = 0. \tag{5.1}$$

Because of the class-E ZVS/ZDS conditions, the class-E inverter achieves high power-conversion efficiency at high frequencies. It is, however, not easy to achieve the class-E ZVS/ZDS conditions because the two strict conditions in (5.1) should be satisfied simultaneously. Generally, input voltage, MOSFET on-duty ratio, resonant inductor, and load resistance are given as design specifications in the class-E inverter designs. Therefore, the shunt capacitance and the resonant capacitance are determined uniquely for achieving the class-E ZVS/ZDS conditions. In addition, the output power of the inverter is fixed from the combination of the input voltage and the load resistance. For obtaining the component values, many analytical expressions and design procedures for the class-E inverter have been presented until now [19]-[23].

5.2.2 Class-E Rectifier

The class-E rectifier consists of diode D as a switching device, shunt capacitance C_D, low-pass filter network $L_f - C_f$, and load resistance R_L as shown on the right-hand side of Fig. 5.1. The waveforms of the class-E rectifier are reversed versions of those of the class-E inverter as shown in Fig. 5.2. The diode works as a half-wave voltage rectifier and the rectified voltage is converted into a dc voltage through the low-pass filter $L_f - C_f$. While the diode D is in the off-state, the current, which is expressed as $i_{C_D} = \omega C_D dv_D/d\theta$, flows through the shunt capacitance C_D. During the diode-off period, the power dissipation in the diode is nearly zero since the diode current i_D is negligible. The diode turns on when the diode voltage decreases to the threshold voltage. While the diode D is in the on-state, the current i_D flows through the diode. In the diode-on duration, the power dissipation in the diode is also kept small since the diode voltage v_D is equal to the threshold voltage, which is regarded as approximately zero. At the diode turn-off transition, the capacitance current, namely the derivative of the capacitance voltage, is zero as shown in Fig. 5.2. From above discussion, it can be stated that the class-E rectifier also satisfies the class-E ZVS/ZDS conditions at turn-off instant. The class-E ZVS/ZDS conditions reduce the switching losses and noise. Therefore, the class-E rectifier can operate with high power-conversion efficiency at high frequencies.

The class-E rectifier operates autonomously though the class-E inverter works with external driving signal. Therefore, the class-E rectifier always achieves the class-E ZVS/ZDS conditions automatically, which is different from the class-E inverter. In the class-E rectifier, the shunt capacitance C_D is a key component. The combination of the input current amplitude of the rectifier and the shunt capacitance value determine the duty ratio of the diode, switch stress on the diode, and output voltage.

5.3 WPT System with Class-E^2 dc-dc converter

5.3.1 Proposed System Topology

Figure 5.3(a) shows a topology of the WPT system with the class-E^2 dc-dc converter [14]-[17], which consists of class-E inverter, resonant inductive coils, and class-E rectifier. This system is regarded as the extended version of the class-E^2 dc-dc converter. By applying the class-E ZVS/ZDS technique to both the inverter and the rectifier, the WPT system can achieve high power-delivery efficiency at high frequencies. Compared with the class-E^2 dc-dc converter as shown in Fig. 5.1, the capacitances C_p and C_2 are newly added in the proposed WPT system as shown in Fig. 5.3(a) to form an impedance matching circuit. In the typical topology of the class-E^2 dc-dc converters, the output power is adjusted by the diode shunt capacitance C_D [26]-[28]. By adding the impedance transformation capacitance C_p to the output network of the inverter, it is possible to adjust the required output power at the inverter part. This is because the degree of freedom increases by adding C_p. Therefore, the diode shunt capacitance C_D can be used for the power-delivery efficiency enhancement. Additionally, the equivalent resistance of the rectifier is changed by varying C_2. The power-delivery efficiency increases as the equivalent resistance of the rectifier increases, which is explained analytically in Section 5.5. For the above reasons, a high power-delivery efficiency can be obtained by adding C_p and C_2, which is one of the emphasis points in this study.

5.3.2 Loosely Inductive Coupled Coils

The loosely inductive coupled coils are considered as a connection part between the inverter and the rectifier. The coupled coils L_1 and L_2 can be modeled as a transformer with mutual inductance M as shown in Fig. 5.3(a). The magnetizing inductance L_1 also acts as the resonant inductance of the inverter, which is related to L_r in Fig. 5.1. The secondary-side coil L_2 and C_2 provides the sinusoidal current i_2 to the rectifier, where C_2 realizes the impedance matching between the primary and secondary parts.

In the MHz frequency range of the resonant converter, the powder core such as listed in [32] is often used for coil implementations. Most of cores, however, have a toroidal shape, which cannot be used at the coupled part of the WPT system. If another core material is adopted, we suffer from a large core loss and thermal management because the big-swing and high frequency current is very hard to achieve a small core loss [33]. Therefore, the air-core coils are often applied to the inductive coupled part of the WPT system with high frequencies [1]-[4], [7]-[17].

The long length of wire is necessary for keeping high inductance in air-core coil, which yields large winding loss. Therefore, the ESRs of the coils in the WPT system are much larger than those in the resonant converter, which is the largest difference between the class-E^2 dc/dc converter and the WPT system designs. Therefore, the conduction losses in the coils are a dominant factor in the WPT system when the switching losses are zero. The purpose of this chapter is to design of the class-E inverter and the class-E rectifier for achieving the class-E ZVS/ZDS conditions as well as power-delivery efficiency enhancement. In this study, the coupling coil parameters are given as design specifications.

5.4 Analytical Expressions

In this section, the analysis of the class-E^2 WPT system is carried out. The circuit operation is considered in the interval $0 \leq \theta < 2\pi$. Because the class-E^2 WPT system is regarded as the extended version of the class-E^2 dc/dc converter, many analytical expressions of the converter such as [23] and [26] can be applied to those of the WPT system.

5.4.1 Assumptions

The system analysis is based on the following assumptions for simplicity:

a) The MOSFET S is operated as an ideal switching device, namely, it has zero on-resistance, infinite off-resistance, and zero switching times.

b) The diode D is also operated as an ideal switching device. Therefore, it has zero forward voltage drop, infinite off-resistance, and zero switching times.

c) The shunt capacitances C_S and C_D include the parasitic capacitances of the MOSFET S and the diode D, respectively.

d) The dc-feed inductance L_C is high enough so that the current through the dc-feed inductance is constant.

e) The loaded Q-factor in the inverter is high enough to generate a pure sinusoidal resonant current i_1.

f) All the passive elements including switching-device parasitic capacitances operate as linear elements.

g) By applying the class-E ZVS/ZDS conditions, not only the switching loss reduction, but also the switching-noise reduction can be achieved. Therefore, it is assumed that both inverter and rectifier satisfy the class-E ZVS/ZDS conditions.

h) The MOSFET is in on-state for $0 \leq \theta < 2\pi D_S$ and in off-state for $2\pi D_S \leq \theta < 2\pi$, where D_S is the MOSFET on-duty ratio.

From above assumptions, the equivalent circuit of the WPT system is illustrated in Fig. 5.3(b), where $k = |M/\sqrt{L_1 L_2}|$ is a coupling coefficient.

5.4.2 Class-E Rectifier

The detailed analysis of the class-E rectifier was carried out in [26]. This subsection shows a summary of the results in [26]. The input current of the rectifier i_2, which flows through the $L_2 - C_2$ resonant filter, is

$$i_2 = \sqrt{2} I_2 \sin(\theta + \phi_r), \tag{5.2}$$

where I_2 and ϕ_r are the effective value of i_2 and the phase shift between the driving signal of the inverter v_g and the input current of the rectifier i_2. Because the diode current i_D is zero at $\theta = 2\pi - \phi_r + \phi_d$, namely $i_D = I_o - \sqrt{2} I_2 \sin\phi_d = 0$, I_2 is expressed as

$$I_2 = \frac{I_o}{\sqrt{2}\sin\phi_d} = \frac{V_o}{\sqrt{2} R_L \sin\phi_d}, \tag{5.3}$$

where I_o, V_o, R_L, and ϕ_d are output dc current, output dc voltage, load resistance of the WPT system, and phase shift between i_2 and the diode voltage v_D, respectively. ϕ_d can be obtained from

$$\tan\phi_d = \frac{1 - \cos(2\pi D_d)}{2\pi(1 - D_d) + \sin(2\pi D_d)}, \tag{5.4}$$

where D_d is the switch-on duty ratio of the diode.

By using D_d and R_L, the shunt capacitance of the diode is expressed as

$$C_D = \frac{1}{2\pi\omega R_L}\left\{1 - \cos(2\pi D_d) - 2\pi^2(1 - D_d)^2 + \frac{[2\pi(1 - D_d) + \sin(2\pi D_d)]^2}{1 - \cos(2\pi D_d)}\right\}. \tag{5.5}$$

The class-E rectifier can be replaced by the input capacitance C_i and the input resistance R_i, which are connected in serial as shown in Fig. 5.3(d). The input capacitance C_i is

$$\begin{aligned} C_i &= 4\pi C_D[4\pi(1 - D_d) + 4\sin(2\pi D_d) - \sin(4\pi D_d)\cos(2\phi_d) \\ &\quad -2\sin(2\phi_d)\sin^2(2\pi D_d) - 8\pi(1 - D_d)\sin\phi_d\sin(2\pi D_d - \phi_d)]^{-1}. \end{aligned} \tag{5.6}$$

The input resistance R_i can be also obtained as

$$R_i = 2R_L\sin^2\phi_d \tag{5.7}$$

The equivalent capacitance of C_2 and C_i connected in serial C_{sec} is expressed as

$$C_{sec} = \frac{C_2 C_i}{C_2 + C_i}. \tag{5.8}$$

From the equivalent capacitance and the input resistance, ϕ_r is expressed as

$$\phi_r = \phi_{inv} + \phi_p + \phi_t = \phi_{inv} + \phi_p + \frac{\pi}{2} - \tan^{-1} \frac{\left(\omega L_2 - \dfrac{1}{\omega C_{sec}}\right)}{R_i}, \tag{5.9}$$

where ϕ_{inv}, ϕ_p, and ϕ_t are the phase shifts between the driving signal v_g and the inverter current i_{inv}, between i_{inv} and the current through the primary coil i_1, and between i_1 and i_2, respectively. ϕ_{inv} and ϕ_p are derived in Section 5.4-D.

5.4.3 Coupling Part

From (5.6) and (5.7), the impedance Z_{sec}, which is defined in Fig. 5.3(d), is expressed as

$$Z_{sec} = R_{L_2} + R_i + j\left(\omega L_2 - \frac{1}{\omega C_{sec}}\right), \tag{5.10}$$

From (5.10), the effective value of induced voltage from the primary part can be obtained as

$$V_{ind} = |Z_{sec}| I_2 = \sqrt{(R_{L_2} + R_i)^2 + \left(\omega L_2 - \frac{1}{\omega C_{sec}}\right)^2} I_2. \tag{5.11}$$

In this analysis, the equivalent transformer model in Fig. 5.3(c) is adopted. Z_{rec} in Fig. 5.3(c) is the same as that in Fig. 5.3(d), namely

$$Z_{rec} = R_{L2} + R_i + \frac{1}{j\omega C_{sec}}. \tag{5.12}$$

The equivalent resistance R_{eq} and inductance L_{eq} of the LIC and rectifier, which is denoted in Fig. 5.3(e), are

$$R_{eq} = \frac{k^2 \omega^2 L_1 L_2 (R_{L_2} + R_i)}{(R_{L_2} + R_i)^2 + \left(\omega L_2 - \dfrac{1}{\omega C_{sec}}\right)^2}, \tag{5.13}$$

and

$$L_{eq} = \frac{k^2 L_1 \left[(R_{L_2} + R_i)^2 - \frac{L_2}{C_{sec}} + \left(\frac{1}{\omega C_{sec}} \right)^2 \right]}{(R_{L_2} + R_i)^2 + \left(\omega L_2 - \frac{1}{\omega C_{sec}} \right)^2} + L_1(1 - k^2). \tag{5.14}$$

5.4.4 Class-E Inverter

From the above analysis, the equivalent circuit of the class-E^2 WPT system is illustrated as shown in Fig. 5.3(e). For satisfying the assumption g), it is quite important to derive the component values for achieving the class-E ZVS/ZDS conditions at the inverter.

Because of the assumption e), the current through the primary coil is

$$i_1 = \sqrt{2} I_1 \sin(\theta + \phi_{inv} + \phi_p), \tag{5.15}$$

where I_1 is effective value of i_1. From the transformer relationship, I_1 can be expressed as

$$I_1 = \frac{V_{ind}}{\omega k \sqrt{L_1 L_2}} = \frac{\sqrt{(R_{L_2} + R_i)^2 + \left(\omega L_2 - \frac{1}{\omega C_{sec}} \right)^2} I_2}{\omega k \sqrt{L_1 L_2}}. \tag{5.16}$$

From [23], ϕ_{inv} is obtained from

$$\tan \phi_{inv} = \frac{\cos(2\pi D_S) - 1}{2\pi(1 - D_S) + \sin(2\pi D_S)}. \tag{5.17}$$

From the impedance calculation of the network that consists of C_p, R_{L_1}, R_{eq}, and L_{eq}, ϕ_p is expressed as

$$\tan \phi_p = \frac{R_{eq} + R_{L_1}}{\omega L_{eq} - \frac{1}{\omega C_p}}, \tag{5.18}$$

The output impedance of the inverter $R_{L_1} + R_{eq} + j\omega L_{eq}$ is transformed into Z_{inv} by the impedance transformation capacitance C_p as shown in Fig. 5.3(f). Z_{inv} is

$$Z_{inv} = \frac{1}{\frac{1}{R_{eq} + R_{L_1} + j\omega L_{eq}} + j\omega C_p} = R_{inv} + j\omega L_{inv}, \tag{5.19}$$

where R_{inv} and L_{inv} are

$$R_{inv} = \frac{(R_{eq} + R_{L_1})}{\omega^2 C_p^2 \left[(R_{eq} + R_{L_1})^2 + \left(\omega L_{eq} - \frac{1}{\omega C_p} \right)^2 \right]}, \tag{5.20}$$

and

$$L_{inv} = \frac{L_{eq}(1 - \omega^2 L_{eq} C_p) - C_p (R_{eq} + R_{L_1})^2}{\omega^2 C_p^2 \left[(R_{eq} + R_{L_1})^2 + \left(\omega L_{eq} - \frac{1}{\omega C_p} \right)^2 \right]}. \tag{5.21}$$

The inverter current i_{inv} is

$$i_{inv} = \sqrt{2} I_{inv} \sin(\theta + \phi_{inv}). \tag{5.22}$$

where I_{inv} is the effective value of i_{inv}. From the relationship between the input voltage and the output current of the class-E inverter [23], I_{inv} and I_I for achieving the class-E ZVS/ZDS conditions are obtained as

$$I_{inv} = \frac{\sqrt{2} \sin(\pi D_S) \sin(\pi D_S + \phi_{inv})}{\pi (1 - D_S) R_{inv}} V_I, \tag{5.23}$$

and

$$I_I = \frac{\cos(2\pi D_S + \phi_{inv}) - \cos\phi_{inv}}{2\pi(1 - D_S)} I_{inv}, \tag{5.24}$$

respectively.

It is known that the resonant filter of the inverter should be inductive for achieving the class-E ZVS/ZDS conditions in the inverter. In this analysis, L_{inv} is divided into L_0 and L_x virtually, where L_0 and C_1 realize resonant filter for ω as shown in Fig. 5.3(f). In this case, L_x, which is used for current phase shift, for achieving the class-E ZVS/ZDS conditions can be obtained from [23] as

$$\begin{aligned} \frac{\omega L_x}{R_{inv}} = & \{2(1 - D_S)^2 \pi^2 - 1 + 2\cos\phi_{inv} \cos(2\pi D_S + \phi_{inv}) \\ & - \cos 2(\pi D_S + \phi_{inv})[\cos(2\pi D_S) - \pi(1 - D_S)\sin(2\pi D_S)]\} \\ & \cdot\{4 \sin(\pi D_S) \cos(\pi D_S + \phi_{inv}) \sin(\pi D_S + \phi_{inv}) \\ & \cdot[(1 - D_S)\pi \cos(\pi D_S) + \sin(\pi D_S)]\}^{-1}. \end{aligned} \tag{5.25}$$

On the other hand, we can have another expression for R_{inv} from the class-E inverter design viewpoint. According to the power relationship between Figs. 5.3(e) and (f), we have

$$I_1^2(R_{eq}+R_{L_1}) = I_{inv}^2 R_{inv}. \tag{5.26}$$

From (5.23) and (5.26), R_{inv} can be obtained as

$$R_{inv} = \frac{2\sin^2(\pi D_S)\sin^2(\pi D_S+\phi_{inv})V_I^2}{\pi^2(1-D_S)^2 I_1^2(R_{eq}+R_{L_1})}. \tag{5.27}$$

Now, we have two expressions of R_{inv} as given in (5.20) and (5.27). By equating the right-had side of (5.20) and (5.27), C_p for achieving both the class-E ZVS/ZDS conditions and the specified output power is obtained as

$$C_p = \frac{\omega L_{eq}R_{inv} \pm \sqrt{R_{inv}(R_{eq}+R_{L_1})\left[(R_{eq}+R_{L_1})(R_{eq}+R_{L_1}-R_{inv})+\omega^2L_{eq}^2\right]}}{\omega R_{inv}\left[(R_{eq}+R_{L_1})^2+\omega^2L_{eq}^2\right]}. \tag{5.28}$$

It is shown in (5.28) that there are two solutions. The solution that satisfies $L_0 = L_{inv} - L_x > 0$ should be selected because L_0 resonates with C_1.

The design equations of C_1 and C_S for satisfying the class-E ZVS/ZDS conditions can be derived by using L_{inv} and R_{inv} [23]. Because the ideal filter for ω is constructed by L_0 and C_1, we have

$$C_1 = \frac{1}{\omega^2 L_0} = \frac{1}{\omega^2(L_{inv}-L_x)}. \tag{5.29}$$

The shunt capacitance for satisfying the class-E ZVS/ZDS conditions is

$$C_S = \frac{2\sin(\pi D_S)\cos(\pi D_S+\phi_{inv})\sin(\pi D_S+\phi_{inv})[(1-D_S)\pi\cos(\pi D_S)+\sin(\pi D_S)]}{\omega\pi^2(1-D_S)R_{inv}} \tag{5.30}$$

Finally, the dc-feed inductance L_C for ensuring less than 10 % current ripple of the input current should satisfy

$$L_C > \frac{R_{inv}}{f}\left(\frac{\pi^2}{2}+2\right). \tag{5.31}$$

In this study, operating frequency f, dc-supply voltage V_I, duty ratio at the inverter D_S, load resistance R_L, and output voltage V_o are given as design specifications. Additionally, the parameters of the LIC part, which are L_1, L_2, R_{L_1}, R_{L_2}, and k, are also given as design specifications. L_C is fixed for achieving the direct input current from (5.31). Additionally, L_f and C_f in the rectifier are determined independently with low cut-off frequency for obtaining the direct output current. Under these design specifications, it is necessary to determine C_S, C_1, and C_p uniquely for achieving the class-E ZVS/ZDS conditions and the specified output power.

The remained component values are C_2 and C_D. In this chapter, these parameters are used for enhancing the power-delivery efficiency.

5.5 Power-Delivery Efficiency

The power-delivery efficiency is defined as

$$\eta = \frac{P_o}{P_I} = \frac{P_o}{P_o + P_{Loss}}, \tag{5.32}$$

where P_{LOSS} is the total power losses in the WPT system.

5.5.1 Power Losses

The cause of the power losses are ESRs of passive elements, MOSFET on-resistance, and forward voltage drop of the rectifier when the switching loss is zero. In this study, the power losses in MOSFET on-resistance r_S; diode due to the forward voltage drop V_{th}; and ESRs of primary coil R_{L_1} and secondary coil R_{L_2} are considered. Figure 5.4 shows the equivalent circuit model of the class-E^2 WPT system for the power-loss calculations. It is assumed that the MOSFET on-resistance and the diode forward voltage drop are small enough not to affect the waveforms [19]-[21] [25].

The output power of the load resistance is

$$P_o = I_o^2 R_L. \tag{5.33}$$

The conduction loss in the MOSFET on-resistance r_S is

$$\begin{aligned} P_S =& \frac{r_S}{2\pi} \int_0^{2\pi} i_S^2 d\theta = \frac{r_S}{2\pi} \int_0^{2\pi D_S} (I_C - i_{in})^2 d\theta \\ =& \frac{r_S}{4\pi} \Big\{ 4\pi D_S (I_C^2 + I_{in}^2) + 4\sqrt{2} I_C I_{in} [\cos(2\pi D_S + \phi_{in}) - \cos\phi_{in}] \\ & + I_{in}^2 [\sin 2\phi_{in} - \sin(4\pi D_S + 2\phi_{in})] \Big\} . \end{aligned} \tag{5.34}$$

The winding losses in the coils are

$$P_{L_1} = R_{L_1} I_1^2 = \frac{R_{L_1} I_o^2}{2k^2 \omega^2 L_1 L_2 \sin^2 \phi_d} \left[(R_{L_2} + R_i)^2 + \left(\omega L_2 - \frac{1}{\omega C_{sec}} \right)^2 \right], \tag{5.35}$$

and

$$P_{L_2} = R_{L_2} I_2^2 = \frac{R_{L_2} I_o^2}{2 \sin^2 \phi_d}. \tag{5.36}$$

Additionally, the power loss in the diode is

$$\begin{aligned} P_D =& \frac{V_{th}}{2\pi} \int_0^{2\pi} i_D \ d\theta_{rec} = \frac{V_{th}}{2\pi} \int_{2\pi(1-D_d)}^{2\pi} I_o - i_2 \ d\theta_{rec} \\ =& \frac{V_{th}}{2\pi} \Big\{ 2\pi D_d I_o + \sqrt{2} I_2 [\cos\phi_d - \cos(\phi_d - 2\pi D_d)] \Big\} \\ =& \frac{V_{th} I_o}{2\pi} \left\{ 2\pi D_d + \frac{\cos\phi_d - \cos(\phi_d - 2\pi D_d)}{\sin\phi_d} \right\}, \end{aligned} \tag{5.37}$$

where $\theta_{rec} = \theta + \phi_r - \phi_d$.

From (5.32) through (5.37), the overall power-delivery efficiency can be obtained as

$$\begin{aligned} \eta_{all} =& \frac{P_o}{P_o + P_S + P_{L_1} + P_{L_2} + P_D} \\ =& 1 \Big/ \Big\langle 1 + \frac{R_{L_1}}{2R_L k^2 \omega^2 L_2 L_2 \sin^2 \phi_d} \left[(R_i + R_{L_2})^2 + \left(\omega L_2 - \frac{1}{\omega C_{sec}} \right)^2 \right] + \frac{R_{L_2}}{2R_L \sin^2 \phi_d} \\ & + \frac{r_S}{4\pi I_o^2 R_L} \Big\{ 4\pi D_S (I_C^2 + I_{in}^2) + 4\sqrt{2} I_C I_{in} [\cos(2\pi D_S + \phi_{in}) - \cos\phi_{in}] \\ & + I_{in}^2 [\sin 2\phi_{in} - \sin(4\pi D_S + 2\phi_{in})] \Big\} \\ & + \frac{V_{th}}{2\pi V_o} \left\{ 2\pi D_d + \frac{\cos\phi_d - \cos(\phi_d - 2\pi D_d)}{\sin\phi_d} \right\} \Big\rangle . \end{aligned} \tag{5.38}$$

5.5.2 Efficiency Enhancement

The power delivery efficiency enhancement of the class-E^2 WPT system is considered from the analytical expression (5.38). Because the MOSFET on-resistance r_S and the diode forward-voltage drop V_{th} are small compared with the load resistance R_L and the output voltage V_o, respectively, we assume that $r_S/R_L = 0$ and $V_{th}/V_o = 0$ in (5.38). In this case, the winding losses of the primary and secondary coils needed to be considered. From this assumption and (5.7), (5.38) can be rewritten as

$$\eta_{en} = \frac{k^2\omega^2 L_1 L_2 R_i}{R_{L_1}(R_i + R_{L_2})^2 + k^2\omega^2 L_1 L_2 (R_i + R_{L_2}) + R_{L_1}\left(\omega L_2 - \dfrac{1}{\omega C_{sec}}\right)^2}. \tag{5.39}$$

In the variations of (5.39), C_2 is a element of C_{sec} as given in (5.8). Additionally, C_D is also a element of C_{sec} as given in (5.4), (5.5), and (5.6). When power-delivery efficiency enhancement by varying C_2 is considered, it is seen from (5.39) that the condition for maximizing η_{en} is

$$\omega L_2 - \frac{1}{\omega C_{sec}} = 0, \tag{5.40}$$

namely

$$C_{2opt} = \frac{C_i}{\omega^2 L_2 C_i - 1}. \tag{5.41}$$

This condition means that the power-delivery efficiency can be enhanced when series connected capacitance C_2 and input capacitance of the rectifier C_i resonate with the secondary coupling inductor L_2. It is seen from (5.13) that the maximization of (5.39) for C_2 is the same as that of the equivalent resistance R_{eq}. The power-conversion efficiency of the inverter part can be simply obtained as $1/(1 + R_{L_1}/R_{eq})$ because the switching loss is equal to zero due to the class-E switching. Therefore, the maximization of R_{eq} leads to a high power-delivery efficiency. By substituting (5.40) into (5.13) and (5.14), we have

$$R_{eqopt} = \frac{k^2\omega^2 L_1 L_2}{R_{L_2} + R_i}. \tag{5.42}$$

and

$$L_{eqopt} = L_1. \tag{5.43}$$

In addition, R_i, which is a function of C_D, is also the parameter enhancing the power-delivery efficiency. The condition for maximizing the power-delivery efficiency is

$$\frac{\partial \eta_{enopt}}{\partial R_i} = \frac{k^2\omega^2 L_1 L_2 (R_{L_1} R_{L_2}^2 - R_{L_1} R_i^2 + k^2\omega^2 L_1 L_2 R_{L_2})}{[R_{L_1}(R_i + R_{L_2})^2 + k^2\omega^2 L_1 L_2 (R_i + R_{L_2})]^2} = 0. \tag{5.44}$$

From (5.44), we obtain R_i for maximizing the power-delivery efficiency as

$$R_{iopt} = \sqrt{\frac{R_{L_1} R_{L_2}^2 + k^2\omega^2 L_1 L_2 R_{L_2}}{R_{L_1}}}. \tag{5.45}$$

By equating the right-hand side of (5.7) and (5.45), the diode on-duty ratio D_d for the maximum power-delivery efficiency can be obtained numerically and the optimum shunt capacitance of the diode C_D is given by (5.5).

5.6 Design Example

5.6.1 Design Specifications

In this section, the step-by-setp design procedure and experimental results are shown. First, the design specifications of the WPT system were given as follows: operating frequency $f = 1$ MHz, output power $P_o = 10$ W, output resistance $R_L = 50\ \Omega$, duty ratio of the inverter $D_S = 0.5$, and distance between the primary and the secondary coils $d_{coils} = 10$ cm.

Additionally, the specifications of the coupling coils are necessary. As stated in Section II, air-core solenoid coils were used as coupling coils. The parameters of the coupling coils are: the diameter $d = 15.5$ cm and the number of turns $N = 8$. Additionally, the number of layers $N_l = 1$ is adopted for the proximity effect reduction [33]. The parameters of the

the primary coil are the same as those of the secondary one in this study. The Litz wires (KERRIGAN LEWIS WIRE) were used for the skin effect reduction. Figure 5.5(a) shows the hand-made coils used in the experiments. The self inductances and the ESRs of the coils were $L_1 = 23.1$ μH, $L_2 = 22.7$ μH, $R_{L_1} = 0.891$ Ω, and $R_{L_2} = 0.829$ Ω at 1 MHz, respectively. These values were measured by HP4284A LCR meter. When these coils are coupled with 10 cm distance, the coupling coefficient was measured as $k = 0.0559$.

5.6.2 Design Procedure

From (5.45), we obtain

$$R_{iopt} = \sqrt{\frac{R_{L_1}R_{L_2}^2 + k^2\omega^2 L_1 L_2 R_{L_2}}{R_{L_1}}} = 7.80\ \Omega. \tag{5.46}$$

The duty ratio of the rectifier for maximizing power delivery efficiency is calculated numerically from (5.7) and (5.46) as

$$D_{dopt} = 0.330. \tag{5.47}$$

From (5.4), the phase shift is

$$\phi_d = \tan^{-1}\left[\frac{1-\cos(2\pi D_d)}{2\pi(1-D_d)+\sin(2\pi D_d)}\right] = 0.283 \text{ rad}. \tag{5.48}$$

From (5.5), the optimum shunt capacitance of the diode is

$$C_D = \frac{1-\cos(2\pi D_d) - 2\pi^2(1-D_d)^2 + \dfrac{[2\pi(1-D_d)+\sin(2\pi D_d)]^2}{1-\cos(2\pi D_d)}}{2\pi\omega R_L} = 5.12 \text{ nF}. \tag{5.49}$$

From (5.6) and (5.41), the secondary resonant capacitance for the maximum power-delivery efficiency is

$$\begin{aligned} C_{2opt} \;=\; & 4\pi C_D \cdot \{\omega^2 L_2[4\pi(1-D_d) - \sin(4\pi D_d)\cos(2\phi_d)\sin(2\phi_d)\sin^2(2\pi D_d) \\ & +4\sin(2\pi D_d) - 8\pi(1-D_d)\sin\phi\sin(2\pi D_d - \phi_d)] - \pi C_D\}^{-1} = 1.28 \text{ nF}. \end{aligned}$$

From (5.42) and (5.43), the equivalent output resistance and inductance of the inverter are

$$R_{eq} = \frac{k^2\omega^2 L_1 L_2}{R_{iopt} + R_{L_2}} = 7.49\ \Omega, \tag{5.50}$$

and

$$L_{eq} = L_1 = 23.1\ \mu H, \tag{5.51}$$

respectively.

From (5.17), the phase shift between the driving signal and output current of the inverter is

$$\phi_{inv} = \pi + \tan^{-1}\left[\frac{\cos(2\pi D_S) - 1}{2\pi(1 - D_S) + \sin(2\pi D_S)}\right] = 2.57\ \text{rad}. \tag{5.52}$$

From (5.27), we obtain

$$R_{inv} = \frac{2\sin^2(\pi D_S)\sin^2(\pi D_S + \phi_{inv})V_I^2}{\pi^2(1 - D_S)^2 I_1^2 (R_{eq} + R_{L_1})} = 26.8\ \Omega. \tag{5.53}$$

From (5.25), the inductance of the resonant filter of the inverter is

$$\begin{aligned} L_x &= R_{inv}\{2(1 - D_S)^2\pi^2 - 1 + 2\cos\phi_{inv}\cos(2\pi D_S + \phi_{inv}) \\ &- \cos 2(\pi D_S + \phi_{inv})[\cos(2\pi D_S) - \pi(1 - D_S)\sin(2\pi D_S)]\} \\ &\cdot\{4\omega\sin(\pi D_S)\cos(\pi D_S + \phi_{inv})\sin(\pi D_S + \phi_{inv})[(1 - D_S)\pi\cos(\pi D_S) + \sin(\pi D_S)]\}^{-1} \\ &= 4.92\ \mu\text{H}. \end{aligned} \tag{5.54}$$

From (5.28), the impedance transformation capacitance is

$$\begin{aligned} C_p &= \frac{\omega L_{eq} R_{inv} - \sqrt{R_{inv}(R_{eq} + R_{L_1})\left[(R_{eq} + R_{L_1})(R_{eq} + R_{L_1} - R_{inv}) + \omega^2 L_{eq}^2\right]}}{R_{inv}\left[(R_{eq} + R_{L_1})^2 + \omega^2 L_{eq}^2\right]} \\ &= 484\ \text{pF}. \end{aligned} \tag{5.55}$$

From (5.21) and (5.29), the resonant capacitance of the primary part is

$$C_1 = \frac{1}{\omega^2(L_{inv} - L_x)} = \frac{1}{\dfrac{L_{eq}(1 - \omega^2 L_{eq} C_p) - C_p(R_{eq} + R_{L_1})^2}{C_p^2\left[(R_{eq} + R_{L_1})^2 + \left(\omega L_{eq} - \dfrac{1}{\omega C_p}\right)^2\right]} - \omega^2 L_x} = 691\ \text{pF}. \tag{5.56}$$

From (5.30), we obtain

$$\begin{aligned} C_S = & \frac{2\sin(\pi D_S)\cos(\pi D_S + \phi_{inv})\sin(\pi D_S + \phi_{inv})[(1-D_S)\pi\cos(\pi D_S) + \sin(\pi D_S)]}{\omega\pi^2(1-D_S)R_{inv}} \\ = & 1.09 \text{ nF}. \end{aligned} \tag{5.57}$$

Finally, the dc-feed inductance of the inverter is

$$L_C > \frac{R_{inv}}{f}\left(\frac{\pi^2}{2} + 2\right) = 186\ \mu\text{H}. \tag{5.58}$$

The low-pass filter $L_f - C_f$ is designed as $L_f = 300\ \mu$H and $C_f = 47\ \mu$F whose cut-off frequency is 1.3 kHz.

The maximum switch and diode voltages were obtained from [23] and [26] as $V_{Smax} = 85.5$ V and $V_{Dmax} = 59.8$ V. Therefore, the IRFS4410 MOSFET and the STPS5H100B Schottky Barrier Diode, whose breakdown voltages are 100 V, were selected as switching devices. From the datasheets, the MOSFET on-resistance and the diode forward-voltage drop were obtained as $r_S = 0.009\ \Omega$ and $V_{th} = 0.61$ V, respectively. In experimental circuits, the shunt capacitances of the MOSFET and the diode were composed of the parasitic capacitances and external capacitances connected in parallel. The parasitic capacitances of the IRFS4410 and the STPS5H100B were estimated to be 500 pF and 170 pF, respectively, which were obtained from the datasheets. Figure 5.5(b) shows the overview of the implemented WPT system. Table 5.1 gives the obtained component values.

5.6.3 Experimental Verification

Figure 5.6 shows the waveforms of the designed system obtained from analysis, PSpice simulation, and experiment. Table 5.1 gives the theoretical and measurements values, which were measured by Iwatsu VOAC7523. It is seen from Fig. 5.6 that all the switch voltage waveforms in this system satisfied the class-E ZVS/ZDS conditions. Additionally, the measured output power was $P_o = 10.1$ W in the experiment. It can be stated from Fig. 5.6 and Table 5.1 that the both simulation and experimental results agreed with the analytical predictions quantitatively, which showed the validities of the presented analytical expressions and design procedure. The measured power-delivery efficiency was 77.1 %, which also agreed with the analytical prediction well.

5.6.4 Validity of Efficiency-Enhancement Design

Figure 5.7 shows the analytical and the PSpice simulated power-delivery efficiencies using the re-designed parameters for C_2 and D_d variations, where the analytical results were obtained from (5.38) and (5.39). It is seen from Fig. 5.7 that analytical predictions η_{all} quantitatively agreed with the PSpice results. It is also seen from Fig. 5.7 that the power delivery efficiency highly depends on C_2 and D_d and the maximum power-delivery efficiencies are achieved at the design values obtained in Section 5.5. The optimal values of C_2 and C_D can be obtained by efficiency optimization with ignoring power losses in the MOSFET and the diode. These results show that C_2 and D_d are important and useful components for enhancing the power-delivery efficiency. The validity of the power-delivery efficiency enhancement technique in Section 5.5 is confirmed from Fig. 5.7.

5.6.5 Comparison With Other System Topologies

For confirming the usefulness and the effectiveness of the class-E^2 dc-dc converter in WPT systems, the efficiency obtained above is compared with those of other systems. Figure 5.8 shows other system topologies compared in this section, which are the system with the class-D inverter and the class-E rectifier and that with the class-E inverter and the half-wave rectifier. The design specifications of the two systems are same as those in this section. These systems were designed by applying the design methods and equations in [12] and [23]. In the system with the class-D inverter, the impedance transformation capacitance C_p should be the inductor L_p because (5.28) was less than zero in the specifications. Table 5.2 gives the obtained component values and the PSpice simulated power-delivery efficiencies of the two systems. As given in Table 5.1 and 5.2, the efficiency of the class-E^2 WPT system is much higher than those of other systems. In the system with the class-D inverter, the switching loss in the MOSFETs becomes a dominant power loss factor, which was measured as about 10 W in the PSpice simulation. The high switching losses lead to the low power-delivery efficiency. On the other hand, in the system with the half-wave rectifier, the efficiency is very low even though the secondary coil L_2 resonates with the secondary capacitor C_2 and the class-E inverter satisfies class-E ZVS/ZDS conditions. This is because the equivalent resistance of the half-wave rectifier, which is related to R_i, cannot be changed and optimized in this topology, whereas R_i can be changed in the class-E rectifier by the diode shunt capacitance C_D. It is seen from this result that the optimization of the equivalent resistance of the rectifier is quite effective for the power-delivery efficiency. These results demonstrate the usefulness and the effectiveness of applying the class-E^2 dc-dc converter to WPT systems.

Table 5.3 shows comparisons of the state of the art in WPT systems. In Table 5.3, “DC-AC system” means a system with only an inverter, namely the secondary side consists of only receiving coil, resonant capacitor, and load resistor. It is seen from Table 5.3 that the efficiency enhancement technique in this chapter is quite useful and effective for WPT systems.

5.7 Conclusion

This chapter has presented analytical expressions and a design procedure for the class-E^2 LIC-WPT system. By using the analytical expressions, it is possible to obtain component values of the class-E^2 WPT system for achieving the class-E ZVS/ZDS conditions. Additionally, the analytical expressions suggest designers how to determine the component values for power-delivery efficiency enhancement. The presented analysis procedure and the efficiency enhancement theory can be adopted for other WPT systems. The analytical predictions agreed with the PSpice-simulation and experimental results quantitatively, which showed the validities of the analytical expressions and the design procedure. In the laboratory experiment, the WPT system for coil distance 10 cm ($k = 0.0559$) achieved 77.1 % power-delivery efficiency with 10 W (50 Ω/22.4 V) output power at 1 MHz operating frequency.

Table 5.1: Design values of design example

	Analytical	Simulated	Measured	Difference*
L_C	186 μH	186 μH	206 μH	10.4 %
L_f	300.0 μH	300.0 μH	315 μH	5.1 %
C_S	1.09 nF	1.09 nF	1.06 nF	-2.5 %
C_1	691 pF	691 pF	696 pF	0.80 % -
C_p	484 pF	484 pF	486 pF	0.35 % -
C_{2opt}	1.28 nF	1.28 nF	1.26 nF	-1.2 % -
C_D	5.12 nF	5.12 nF	5.16 nF	0.70 %
C_f	47 μF	47 μF	-	-
R_L	50.0 Ω	50.0 Ω	50.2 Ω	0.4 %
L_1	-	23.1 μH	23.1 μH	-
L_2	-	22.7 μH	22.7 μH	-
k	-	0.0559	0.0559	-
r_{L_1}	-	0.891 Ω	0.891 Ω	-
r_{L_2}	-	0.829 Ω	0.829 Ω	-
d_{coils}	-	-	10 cm	-
f	1 MHz	1 MHz	1 MHz	0.0 %
D_{dopt}	0.330	-	-	-
V_I	24.0 V	24.0 V	24.0 V	0.0 %
P_o	10.0 W	10.1 W	10.1 W	0.66 %
η_{all}	79.0 %	78.4 %	77.1 %	-2.4 %

* “Difference” is the difference between analytical and experimental results.

Table 5.2: PSpice simulated design values of other systems

	Class-D inverter and Class-E rectifier	Class-E inverter and Half-wave rectifier
L_C	-	70 μH
L_f	300.0 μH	-
C_S	-	6.25 nF
C_1	2.18 nF	587 pF
C_p or L_p	25.8 μH (L_p)	528 pF (C_p)
C_2	1.28 nF	130 pF
C_D	5.12 nF	-
C_f	47 μF	47 μF
R_L	50.0 Ω	50.0 Ω
L_1	23.1 μH	23.1 μH
L_2	22.7 μH	22.7 μH
k	0.0559	0.0559
r_{L_1}	0.891 Ω	0.891 Ω
r_{L_2}	0.829 Ω	0.829 Ω
f	1 MHz	1 MHz
D_d	0.330	-
V_I	24.0 V	24.0 V
P_o	10.8 W	9.66 W
η_{all}	30.7 %	22.5 %

Table 5.3: WPT systems comparison

	Distance (cm)	Frequency (kHz)	Coupling coefficient	Diameter of coils TX, RX (cm)	Inductance of coils TX, RX (μH)	Output Power (W)	Load resistance (Ω)	System topology	Efficiency (%)
[16]	0	200	0.5	4.3, 4.3	24, 24	13	10	DC-DC system: Class-E^2 dc-dc converter	78.6
[8]	0	134	0.373	21, 13	-, -	69	50	DC-AC system: Class-E inverter	74.2
[9]	0	240	0.139	18, 5	34.58, 4.05	3.7	60	DC-AC system: Class-E inverter	66
[34]	0.1	60	0.52	-, -	166.5, 166.5	3k	18	DC-DC system: H-bridge inverter and Full-wave rectifier	93
[11]	5	800	0.1	8, 7	5.76, 6.69	12	470	DC-AC system: Class-E inverter	57
This work	10	1000	0.0559	15.5, 15.5	23.1, 22.1	10	50	DC-DC system: Class-E^2 dc-dc converter	77.1
[10]	30	6000	0.035	30, 20	-, -	95	50	DC-AC system: Class-E inverter	77
[35]	100	500	0.0256	100, 100	161, 158	40	15	DC-AC system: H-bridge inverter	76

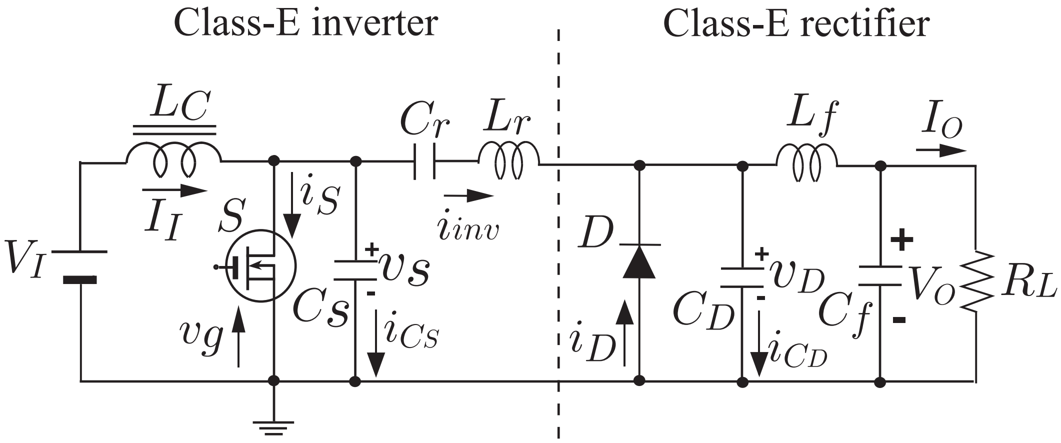

Figure 5.1: Class-E^2 dc-dc converter.

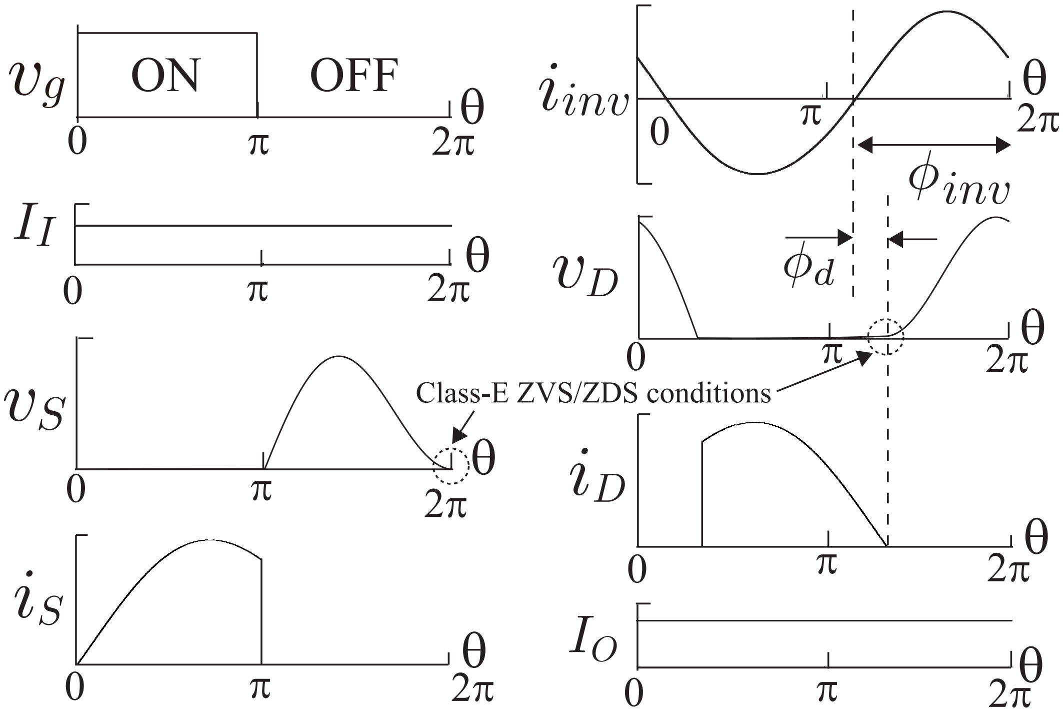

Figure 5.2: Waveforms of the class E^2 dc-dc converter.

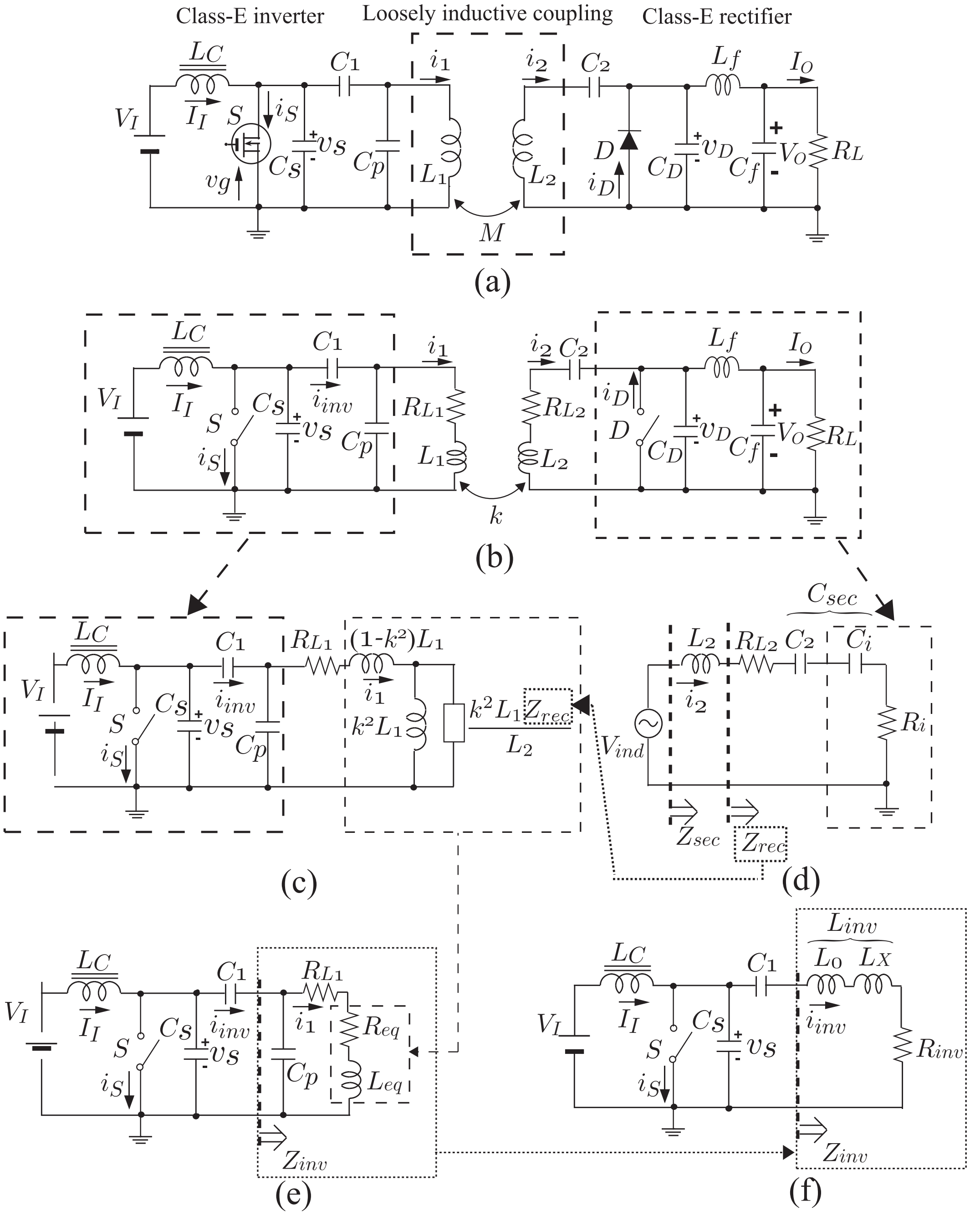

Figure 5.3: Class-E^2 WPT system. (a) System topology. (b) Equivalent circuit model. (c) Equivalent circuit of the inverter part. (d) Equivalent circuit of the rectifier part. (e) and (f) Equivalent circuits boiled down to the class-E inverter.

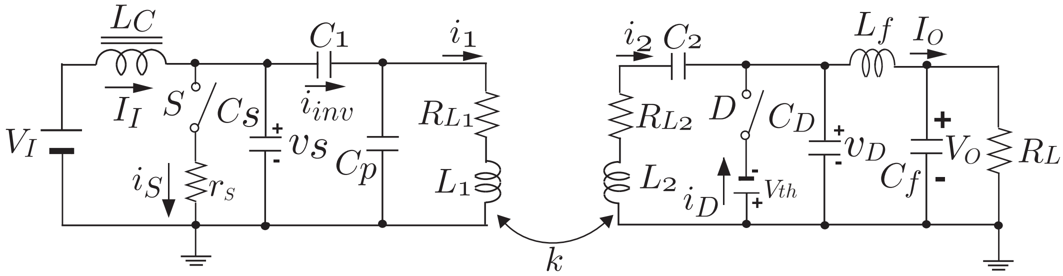

Figure 5.4: Equivalent circuit of class-E^2 WPT system for power-loss calculations.

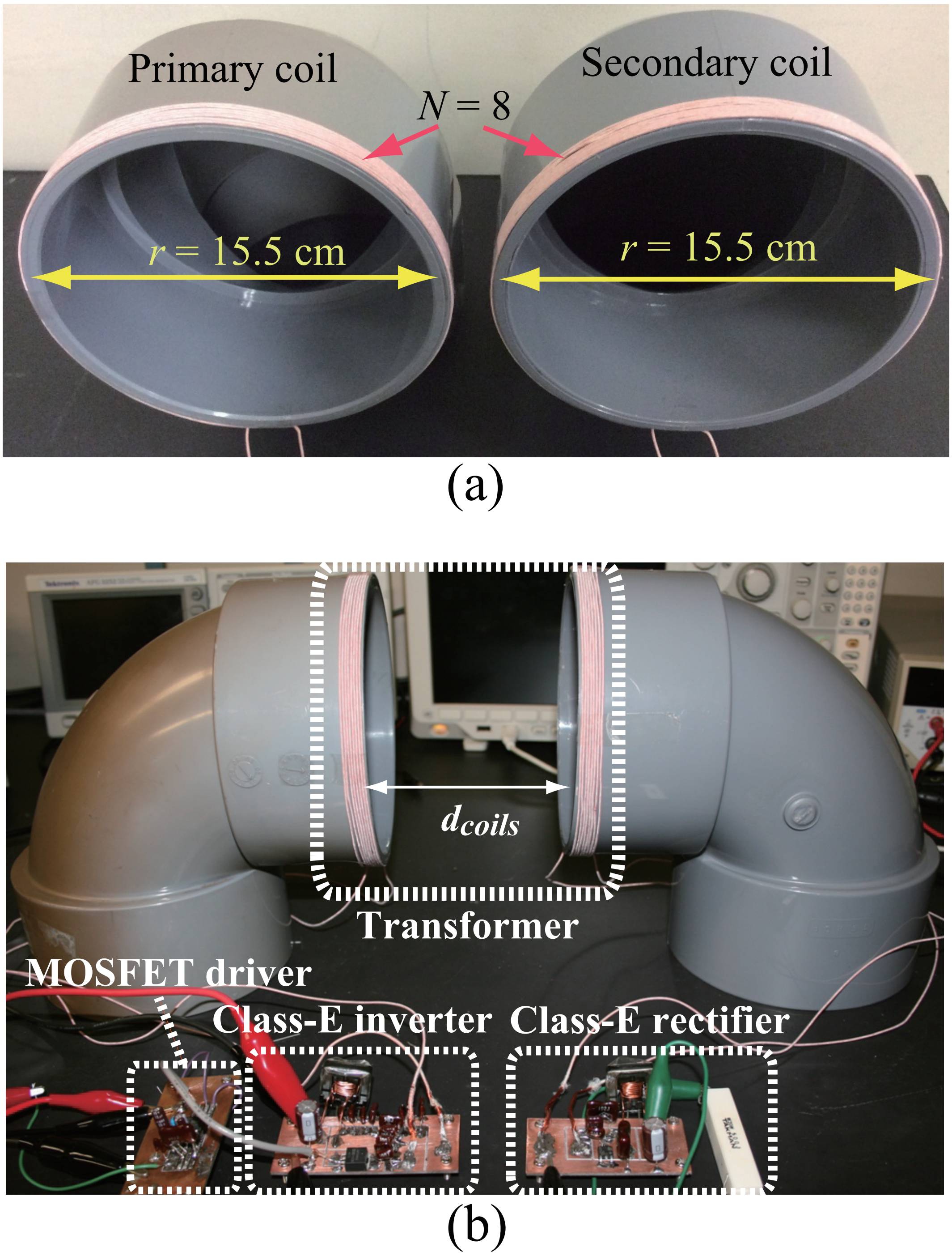

Figure 5.5: Experimental set up. (a) Hand-made coils. (b) Overview of implemented system.

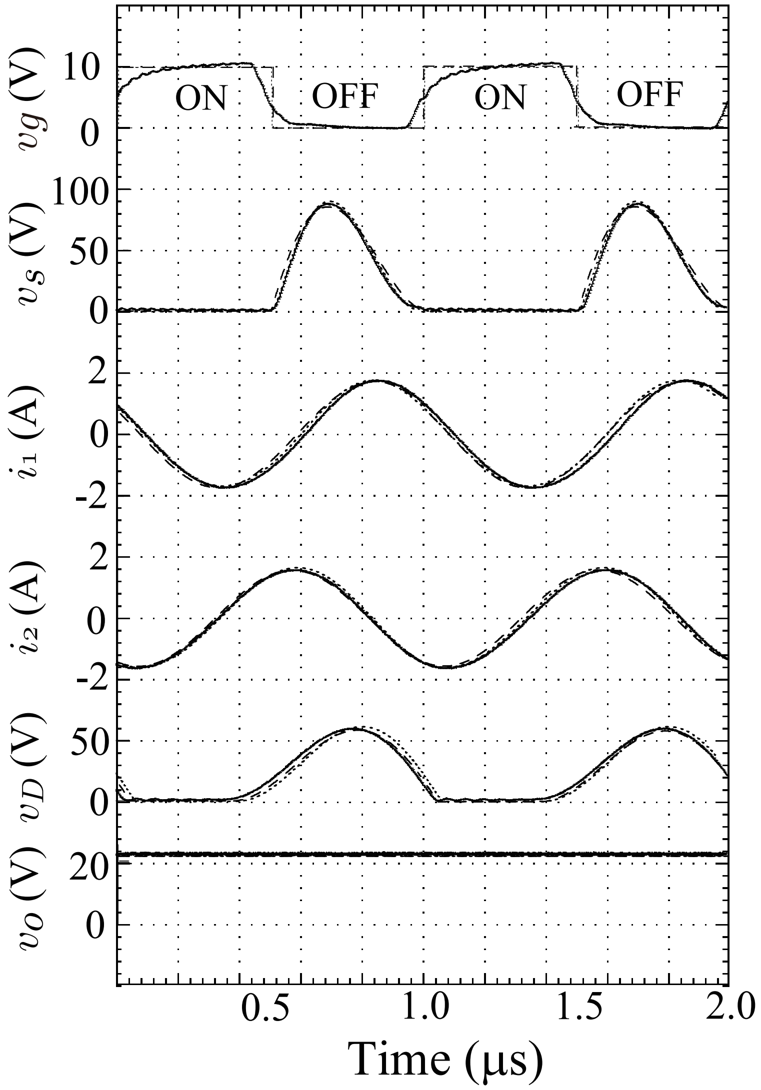

Figure 5.6: Analytical(dashed), PSpice(dotted), and experimental(solid) waveforms for design example.

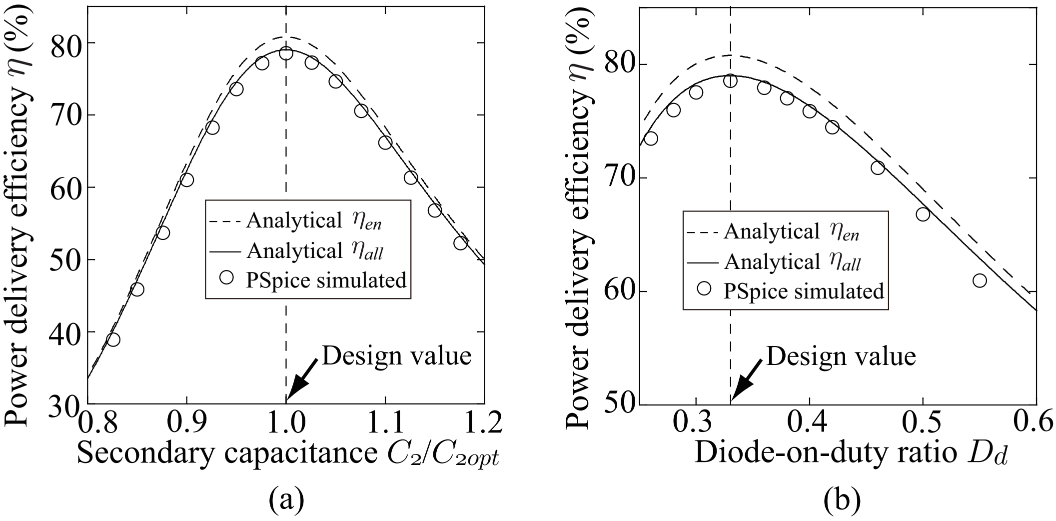

Figure 5.7: Power-delivery efficiencies using re-designed parameters (a) for C_2 variation and (b) for D_d variation.

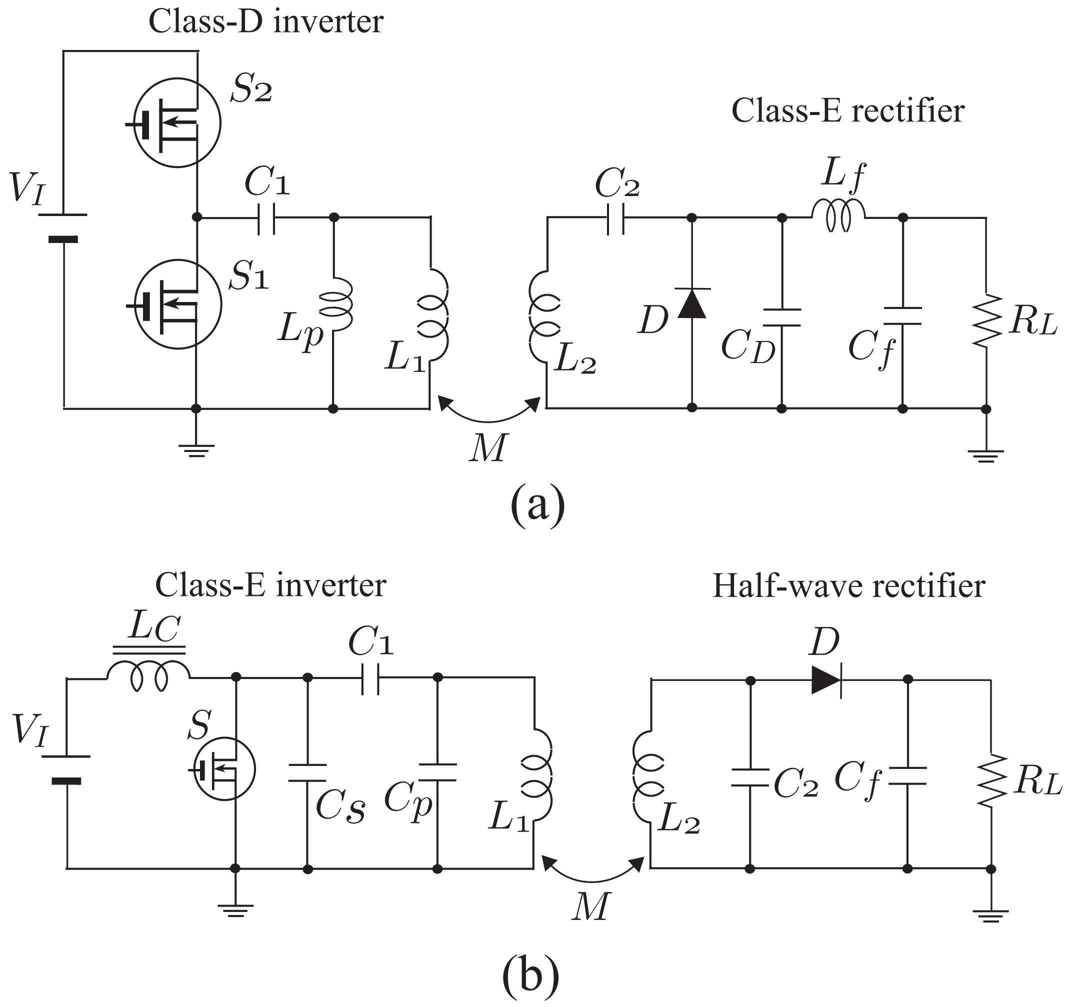

Figure 5.8: Other WPT system topologies. (a) System with class-D inverter and class-E rectifier. (b) System with class-E inverter and half-wave rectifier.

References

[1] A. Kurs, A. Karalis, R. Moffatt, J. D. Joannopoulos, P. Fisher, and M. Soljacic, “Wireless power transfer via strongly coupled magnetic resonances,” *Sci. Express,* vol. 317, no. 5834, pp. 83–86, Jul. 2007.

[2] A. P. Sample, D. A. Meyer, and J. R. Smith, “Analysis, experimental results, and range adaptation of magnetically coupled resonators for wireless power transfer,” *IEEE Trans. Ind. Electron.,* vol. 58, no. 2, pp. 544–554, Feb. 2011.

[3] T. Imura and Y. Hori, “Maximizing air gap and efficiency of magnetic resonant coupling for wireless power transfer using equivalent circuit and Neumann formula,” *IEEE Trans. Ind. Electron.,* vol. 58, no. 10, pp. 4746–4752, Oct. 2011.

[4] E. Bou, E. Alarcon, and R. Sedwick, “Maximizing efficiency through impedance matching from a circuit-centric model of non-radiative resonant wireless power transfer,” *in Proc. IEEE ISCAS,* May 2013, pp. 29–32.

[5] C. Wang, O. H. Stielau, and G. A. Covic, “Design considerations for a contactless electric vehicle battery charger,” *IEEE Trans. Ind. Electron.,* vol. 52, no. 5, pp. 1308–1314, Oct. 2005.

[6] G. Wang, W. Liu, M. Sivaprakasam, and G. A. Kendir, “Design and analysis of an adaptive transcutaneous power telemetry for biomedical implants,” *IEEE Trans. Circuits Systems I, Reg. Papers,* vol. 52, no. 10, pp. 2109–2117, Oct. 2005.

[7] G. A. Kendir, W. Liu, R. Bashirullah, G. Wang, M. S. Humayun, and J. Weiland, “An optimal design methodology for inductive power link with Class-E amplifier,” *IEEE Trans. Circuits Syst. I,* vol. 52, no. 5, pp. 857–866, May 2005.

[8] Z. N. Low, R. Chinga, R. Tseng, and J. Lin, “Design and test of a high-power high-efficiency loosely coupled planar wireless power transfer system,” *IEEE Trans. Ind. Electron.,* vol. 56, no. 5, pp. 1801–1812, May 2009.

[9] J. J. Casanova, Z. N. Low, and J. Lin, “Design and optimization of a Class-E amplifier for a loosely coupled planar wireless power system”, *IEEE Trans. Circuits Syst. II, Exp. Briefs,* vol. 56, no. 11, pp. 830–834, Nov. 2009.

[10] M. Pinuela, D. C. Yates, S. Lucyszyn, and P. Mitcheson, “Maximizing DC to load efficiency for inductive power transfer,” *IEEE Trans. Power Electron.,* vol. 28, no. 5, pp. 2437–2447, May 2013.

[11] S Aldhaher, P Luk, and J Whidborne, “Tuning class E inverters applied in inductive links using saturable reactors,” *IEEE Trans. Power Electron.,* vol. 29, no. 6, pp. 2969–2978, Jun. 2014.

[12] T. Nagashima, X. Wei, T. Suetsugu, and H. Sekiya “Inductively coupled wireless power transfer with class-DE power amplifier,” *in Proc. IEEE APCCAS,* Dec. 2012, pp. 73–76.

[13] D. Murthy-Buller, A. Bauer, W. Kerin, and M. K. Kazimierczuk, “Inverter using loosely coupled inductors for wireless power transfer,” *in Proc. IEEE MWSCAS,* Aug. 2012, pp. 1164–1167.

[14] T. Nagashima, K. Inoue, X. Wei, E. Bou, E. Alarcon, and H. Sekiya, “Inductively coupled wireless power transfer with class-E^2 DC-DC converter,” *in Proc. European Conference on Circuit Theory and Design (ECCTD),* Sept. 2013.

[15] T. Nagashima, K. Inoue, X, Wei, E. Bou, E. Alarcon, M. K. Kazimierczuk, and H. Sekiya, “Analytical design procedure for resonant inductively coupled wireless

power transfer with class-E^2 DC-DC converter" *in Proc. IEEE ISCAS,* Jun. 2014, pp. 113–116.

[16] P. Luk, S. Aldhaher, W. Fei, and J. Whidborne, "State-space modelling of a class E^2 converter for inductive links," *IEEE Trans. Power Electron.,* vol. 30, no. 6, pp. 3242–3251, Jun. 2015.

[17] S. Aldhaher, P. Luk, K. Drissi, and J. Whidborne, "High input voltage high frequency class E rectifiers for resonant inductive links," *IEEE Trans. Power Electron.,* vol. 30, no. 3, pp. 1328–1335, Mar. 2015.

[18] N. O. Sokal and A. D. Sokal, "Class E - A new class of high-efficiency tuned single-ended switching power amplifiers," *IEEE Jounal of Solid State Circuits*, vol. 10, no. 3, pp. 168–176, Jun. 1975.

[19] X. Wei, H. Sekiya, S. Kuroiwa, T. Suetsugu, and M. K. Kazimierczuk, "Design of class-E amplifier with MOSFET linear gate-to-drain and nonlinear drain-to-source capacitances," *IEEE Trans. Circuits Syst.*, vol. 58, no. 10, pp. 2556–2565, Oct. 2011

[20] T. Nagashima, X. Wei, T. Suetsugu, M. K. Kazimierczuk, and H. Sekiya, "Waveform equations, output power, and power conversion efficiency for class-E inverter outside nominal operation," *IEEE Trans. Ind. Electron.,* vol. 61, no. 4, pp. 1799–1810, Apr. 2014.

[21] M. Hayati, A. Lotfi, M. K. Kazimierczuk, and H. Sekiya, "Analysis, design and implementation of class-E ZVS power amplifier with MOSFET nonlinear drain-to-source parasitic capacitance at any grading coefficient," *IEEE Trans. Power Electron.,* vol. 29, no. 9, pp. 4989–4999, Sept. 2014.

[22] M. Hayati, A. Lotfi, M. K. Kazimierczuk, and H. Sekiya, “Generalized design considerations and analysis of class-E amplifier for sinusoidal and square input voltage waveform,” *IEEE Trans. Ind. Electron.,* vol. 62, no. 1, pp. 211–220, Jan. 2015.

[23] M. K. Kazimierczuk and D. Czarkowski, *Resonant Power Converters 2nd Ed.*, New York, NY: John Wiley & Sons, 2011.

[24] H. Koizumi, T. Suetsugu, M. Fujii, K. Shinoda, S. Mori, and K. Ikeda, “Class DE high-efficiency tuned power amplifier,” *IEEE Trans. Circuits Syst.,* vol. 43, no. 1, pp. 51–60, Jan. 1996.

[25] H. Sekiya, N. Sagawa, and M. K. Kazimierczuk, “Analysis of class DE amplifier with nonlinear shunt capacitances at any grading coefficient for high Q and 25 % duty ratio,” *IEEE Trans. Power Electron.,* vol. 25, no. 4, pp. 924–932, Apr. 2010.

[26] M. K. Kazimierczuk and J. Jozwik, “Resonant DC/DC converter with class-E inverter and class-E rectifier,” *IEEE Trans. Ind. Electron.,* vol. 36, no. 4, pp. 468–478, Nov. 1989.

[27] J. Jozwik and M. K. Kazimierczuk, “Analysis and design of class-E^2 DC/DC converter,” *IEEE Trans. Ind. Electron.,* vol. 37, no. 2, pp. 173–183, Apr. 1990.

[28] H. Sekiya, J. Lu, and T. Yahagi, “Design of generalized class E^2 dc/dc converter,” *Int. J. of Circuit Theory and Applications*, vol. 31, no. 3, pp. 229–248, Aug. 2003.

[29] M. K. Kazimierczuk, “Analysis of class E zero-voltage switching rectifier,” *IEEE Trans Circuit Syst.,* vol. 37, no. 6, pp. 747–755, Jun. 1990.

[30] M. Fujii, T. Suetsugu, K. Shinoda, and S. Mori, “Class-E rectifier using thinned-out method,” *IEEE Trans. Power Electron.,* vol. 12, no. 5, pp. 832–836, Sept. 1997.

[31] K. Fukui and H. Koizumi, "Class E rectifier with controlled shunt capacitor," *IEEE Trans. Power Electron.,* vol. 27, no. 8, pp. 3704–3713, Aug. 2012.

[32] [Online]. Available: http://www.micrometals.com/catalog_index.html

[33] M. K. Kazimierczuk and H. Sekiya, "Design of AC resonant inductors using area product method," *in Proc. IEEE ECCE*, Sept. 2009, pp. 994–100.

[34] A. J. Moradewicz and M. P. Kazmierkowski, "Contactless energy transfer system with FPGA-controlled resonant converter," *IEEE Trans. Ind. Electron.,* vol. 57, no. 9, pp. 3181–3190, Sept. 2010.

[35] J. Garnica, J. Casanova, and J. Lin, "High efficiency midrange wireless power transfer system," *Proc. IEEE MTT-S Int. Microw. Workshop Series Innovat. Wireless Power Transmiss.: Technol., Syst., Appl.,* May 2011, pp.73–76.

Chapter 6

Analytical Expressions of Class-E^2 Wireless Power Transfer System for Any System Parameter

●● ABSTRACT ●●

This chapter presents analytical expressions of the class-E^2 wireless power transfer (WPT) system at any system parameter. In the previous researches of the class-E^2 WPT system, system behavior only with the class-E zero-voltage switching and zero-derivative switching (ZVS/ZDS) conditions has been considered. In the WPT system, however, it is important and useful to comprehend the system behavior and performance in system-parameter spaces, especially the coupling coefficient and the load resistance. From the obtained analytical expressions, important information, such as output power, power-delivery efficiency, and state of switching-patterns as a function of system parameters, can be obtained analytically. By carrying out PSpice simulations and circuit experiments, it is shown that the analytical predictions agreed with the simulated and experimental results quantitatively, which indicates the validity of the analytical expressions.

6.1 Introduction

A WPT system with the class-E^2 dc-dc converter [1], [2], which consists of the class-E inverter [3], [4] and the class-E rectifier [5], [6], is one of the high power-delivery efficiency WPT system and the analyses and designs of the class-E^2 WPT system have been investigated [7]-[10]. The class-E^2 dc-dc converter achieves high power-conversion efficiency at high frequencies by satisfying the class-E zero-voltage and zero-derivative switching (ZVS/ZDS) conditions, which are called “nominal conditions”. Therefore, most of previous researches of the class-E^2 WPT system have focused on system designs for the nominal operations. When the class-E^2 WPT systems in practical applications are considered, however, it is important to comprehend the characteristics of the WPT system against system parameter variations, especially coupling-coefficient and load-resistance variations. For example, coupling-coefficient variation, which occurs due to the distance and location variations between the transmitter and the receiver, greatly affects the system performance, such as output power and power-delivery efficiency [10], [11]-[13], [15]-[17], [18]. Additionally, the WPT systems with frequency tuning [12], [16], [17], automatic impedance matching [18], and post regulations [19], [20] operate over wide parameter regions, which indicates the importance of comprehension of system behavior at any system parameter.

It is expected that the system performance can be comprehended easily when circuit simulators are utilized. A high calculation cost is, however, necessary for obtaining the system performance in the steady state because inductive-coupled WPT systems have usually a long transient time. Additionally, circuit simulators can give waveforms at a fixed set of parameters, which means that it is hard to comprehend the circuit behavior in a wide parameter space. For the above reasons, it is an effective approach to obtain the analytical expressions though it is not a simple task. When the analytical expressions are obtained, system performance of the WPT system at any set of system parameters can be derived with low computation cost. Moreover, comprehensions of system performance as well as analytical expressions themselves cultivate designer's fundamental understanding and intuition.

This chapter presents analytical expressions of the class-E^2 WPT system at any system parameter. By considering non-nominal operations of the class-E inverter, system behavior at any system-parameter set can be expressed accurately. For example, the output power and the power-delivery efficiency as functions of coupling coefficient and load resistance are given. It is clarified from the analytical expressions that the ZVS condition is always satisfied when the coupling coefficient decreases or the load resistance increases from the nominal value. Additionally, the switching-pattern distribution map of the class-E^2 WPT system in a parameter space is illustrated from the analytical expressions. By using the distribution map, the WPT system achieving the ZVS at any load resistance conditions can be designed, which is one of the applications of the analytical expressions. The analytical predictions agreed with the PSpice-simulation and experimental results quantitatively, which showed the validities of the analytical expressions.

6.2 Class-E^2 WPT System

The class-E^2 WPT system proposed in Chapter 5, which is shown in Fig. 5.3(a), is analyzed in this chapter.

For achieving the class-E ZVS/ZDS conditions at the class-E inverter, the component values should be determined uniquely. Namely, the class-E ZVS/ZDS conditions are achieved at a certain parameter set and non-nominal operations appear even when system parameters vary from the nominal conditions slightly.

On the other hand, the class-E rectifier works autonomously though the class-E inverter works with external driving signal. The class-E rectifier always achieves the class-E ZVS/ZDS conditions at any parameters, which is different from the class-E inverter.

6.3 Waveform Equations For Any Parameter Variations

In this section, steady-state waveform equations for the class-E^2 WPT system at any parameters are presented. When system parameters, e.g., the coupling coefficient and the load resistance, vary, the switching pattern is changed from the nominal operation. Therefore, it is necessary to consider the switching patterns at non-nominal operations for expressing system behavior at any system parameter.

6.3.1 Switching Patterns of Class-E Inverter

When the system parameter varies from the nominal conditions, the amplitude and the phase shift of the inverter current also vary. As a result, the class-E ZVS/ZDS conditions cannot be achieved and the change of the switching pattern occurs. In this chapter, three switching patterns, which are the same as those in Chapter 3, are considered as non-nominal operations. Example of switch-voltage and switch current waveforms are shown in Fig. 3.3.

On the other hand, the class-E rectifier autonomously achieves the class-E ZVS/ZDS conditions at the diode turn-off instant. Therefore, it is unnecessary to consider the switching patterns non-nominal conditions in the class-E rectifier analysis

6.3.2 Assumptions

The system analysis is based on the following assumptions for simplicity:

a) The MOSFET S operates as an ideal switching device, namely it has zero on-resistance, infinite off-resistance, and zero switching times.

b) The diode D also works as an ideal switching device. Therefore, it has zero forward voltage drop, zero on-resistance, infinite off-resistance, and zero switching times.

c) The shunt capacitances C_S and C_D include the parasitic capacitances of the MOSFET S and the diode D, respectively.

d) The dc-feed inductance L_C is high enough so that the current through the dc-feed inductance is dc-input current I_I.

e) The loaded Q-factor in the inverter is high enough to generate a pure sinusoidal resonant current i_1 with operating frequency.

f) All the passive elements including switching-device parasitic capacitances works as linear elements.

g) The circuit operations are considered in the interval $0 \leq \theta < 2\pi$. The MOSFET is in off-state for $0 \leq \theta < 2\pi D_S$ and in on-state for $2\pi D_S \leq \theta < 2\pi$, where D_S is the MOSFET off-duty ratio.

h) The MOSFET body diode turns on at $\theta = \theta_1$ and turns off at $\theta = \theta_2$ for $0 < \theta_1 \leq \theta_2 < 2\pi D_S$. When θ_1 and/or θ_2 do not appear during switch-off interval, this analysis gives $\theta_1 = 2\pi D_S$ and/or $\theta_2 = 2\pi D_S$, respectively.

From the above assumptions, the equivalent circuit of the WPT system is illustrated in Fig. 5.3(b).

6.3.3 Class-E Rectifier

The detailed analysis of the class-E rectifier was carried out in [1]. This subsection introduces only the resulting equations in [1].

The input current of the rectifier i_2, which flows through the L_2-C_2 resonant filter, is

$$i_2 = I_2 \sin(\theta + \phi_t + \phi_p + \phi_{inv}), \tag{6.1}$$

where I_2, ϕ_t, ϕ_p, and ϕ_{inv} are the amplitude of i_2, the phase shift between the current through the primary coil i_1 and i_2, that between inverter current i_{inv} and i_1, that between the driving signal v_g and i_{inv}, respectively. ϕ_t is derived in Subsection 6.3-D, and ϕ_p and ϕ_{inv} are derived in Subsection 6.3-E. Because the diode current i_D is zero at diode turn-off instant, i_2 is equal to I_o at $\theta = 2\pi - \phi_t - \phi_p - \phi_{inv} + \phi_d$. Namely, we have

$$I_2 = \frac{I_o}{\sin\phi_d} = \frac{V_o}{R_L \sin\phi_d}, \tag{6.2}$$

where V_o, R_L, and ϕ_d are output voltage, load resistance of the WPT system, and phase shift between i_2 and the diode voltage v_D, respectively. The phase shift between i_2 and v_D can be obtained from

$$\tan\phi_d = \frac{1 - \cos(2\pi D_d)}{2\pi(1 - D_d) + \sin(2\pi D_d)}, \tag{6.3}$$

where D_d is the diode-on duty ratio, which depends on $\omega R_L C_D$. The relationship between $\omega R_L C_D$ and D_d is expressed as

$$\begin{aligned}\omega R_L C_D = \frac{1}{2\pi}\Bigg\{ & 1 - \cos(2\pi D_d) - 2\pi^2(1 - D_d)^2 \\ & + \frac{[2\pi(1 - D_d) + \sin(2\pi D_d)]^2}{1 - \cos(2\pi D_d)}\Bigg\}.\end{aligned} \tag{6.4}$$

The diode current and voltage are expressed as

$$i_D = \begin{cases} 0, & \text{for } 0 \le \theta_{rec} < 2\pi(1 - D_d) \\ I_o - I_2 \sin(\theta_{rec} + \phi), & \text{for } 2\pi(1 - D_d) \le \theta_{rec} < 2\pi \end{cases} \tag{6.5}$$

and

$$v_D = \tag{6.6}$$
$$\begin{cases} \dfrac{-I_o}{\omega C_D}\left[\theta_{rec} - \sin\theta_{rec} + \dfrac{\cos\theta_{rec} - 1}{\tan\phi_d}\right], & \text{for } 0 \leq \theta_{rec} < 2\pi(1-D_d) \\ 0, & \text{for } 2\pi(1-D_d) \leq \theta_{rec} < 2\pi \end{cases}$$

respectively, where $\theta_{rec} = \theta + \phi_t + \phi_p + \phi_{inv} - \phi_d$.

The class-E rectifier is modeled as the input capacitance C_i and the input resistance R_i, which are connected in series as shown in Fig. 5.3(d). The equivalent input capacitance and input resistance of the rectifier are expressed as

$$\begin{aligned} C_i &= 4\pi C_D/[4\pi(1-D_d) + 4\sin(2\pi D_d) - \sin(4\pi D_d)\cos(2\phi_d) \\ &-2\sin(2\phi_d)\sin^2(2\pi D_d) - 8\pi(1-D_d)\sin\phi_d\sin(2\pi D_d - \phi_d)], \end{aligned} \tag{6.7}$$

and

$$R_i = 2R_L\sin^2\phi_d, \tag{6.8}$$

respectively. The equivalent resonant capacitance C_r at the receiver is the sum of C_2 and C_i connected in series as shown in Fig. 5.3(d). Therefore, we have

$$C_r = \frac{C_2 C_i}{C_2 + C_i}. \tag{6.9}$$

6.3.4 Coupled Part

From (6.7) and (6.8), the equivalent impedance Z_r, which is defined in Fig. 5.3(d), is expressed as

$$Z_r = R_{L_2} + R_i + j\left(\omega L_2 - \frac{1}{\omega C_r}\right). \tag{6.10}$$

From (6.10), the amplitude of induced voltage from the transmitter to the secondary coil can be obtained as

$$V_{ind} = |Z_r|I_2 = \sqrt{(R_{L_2} + R_i)^2 + \left(\omega L_2 - \frac{1}{\omega C_r}\right)^2}\, I_2. \tag{6.11}$$

In this analysis, the inductive coupling is modeled as the transformer with coupling coefficient as shown in Fig. 5.3(b). From the transformer relationship, (6.8), and (6.9), ϕ_t is expressed as

$$\phi_t = \frac{\pi}{2} - \tan^{-1} \frac{\left(\omega L_2 - \dfrac{1}{\omega C_r}\right)}{R_i}. \tag{6.12}$$

Z_{rec} in Fig. 5.3(c) is the same as that in Fig. 5.3(d), namely

$$Z_{rec} = R_{L_2} + R_i + \frac{1}{j\omega C_r}. \tag{6.13}$$

The equivalent resistance of the coupled coils and rectifier as shown in Fig. 5.3(e) is

$$R_{eq} = \frac{k^2\omega^2 L_1 L_2 (R_{L_2} + R_i)}{(R_{L_2} + R_i)^2 + \left(\omega L_2 - \dfrac{1}{\omega C_r}\right)^2}, \tag{6.14}$$

where k is the coupling coefficient. Additionally, the equivalent inductance of the coupled coils and rectifier L_{eq} as shown in Fig. 5.3(e) can be expressed as

$$L_{eq} = \frac{k^2 L_1 \left[(R_{L_2} + R_i)^2 - \dfrac{L_2}{C_r} + \left(\dfrac{1}{\omega C_r}\right)^2\right]}{(R_{L_2} + R_i)^2 + \left(\omega L_2 - \dfrac{1}{\omega C_r}\right)^2} + L_1(1 - k^2). \tag{6.15}$$

By using R_{eq} and L_{eq}, the equivalent model of the class-E^2 WPT system is illustrated as the class-E inverter as shown in Fig. 5.3(e). In inductive coupled systems, the resonance in both primary and secondary parts is greatly effective for enhancing power-delivery efficiency [11]-[13]. When C_r resonates with L_2, R_{eq} and L_{eq} are

$$R_{eqr} = \frac{k^2\omega^2 L_1 L_2}{R_{L_2} + R_i} \text{ and } L_{eqr} = L_1, \tag{6.16}$$

respectively. It is an important characteristics from (6.16) that coupling coefficient affects only R_{eq} when C_r resonates with L_2, which is an important suggestion for comprehending the WPT-system operation. In the class-E inverter, the ZVS is achieved when load resistance decreases from the nominal value. Therefore, class-E inverter can always achieve the ZVS when the coupling coefficient is smaller than the nominal value.

On the other hand, it is seen from (6.3), (6.4), (6.7), and (6.8) that ϕ_d, D_d, R_i, and C_i are functions of the load resistance. This is because the diode-on duty ratio is a function of the load resistance as given in (6.4). Namely, the rectifier properties vary when the load resistance varies.

6.3.5 Class-E Inverter

Because of the assumption e), the current through the primary coil is

$$i_1 = I_1 \sin(\theta + \phi_{inv} + \phi_p), \tag{6.17}$$

where I_1 is the amplitude of i_1, which can be expressed from the transformer relationship as

$$I_1 = \frac{V_{ind}}{\omega k \sqrt{L_1 L_2}}. \tag{6.18}$$

By using the output-network components, the phase shift between i_{inv} and i_1 is expressed as

$$\tan\phi_p = \frac{R_{eq} + R_{L_1}}{\omega L_{eq} - \dfrac{1}{\omega C_p}}. \tag{6.19}$$

The output impedance of the inverter $R_{L_1} + R_{eq} + j\omega L_{eq}$ and the impedance transformation capacitance C_p are transformed into the inverter impedance Z_{inv} as shown in Fig. 5.3(f), namely

$$Z_{inv} = \frac{1}{\dfrac{1}{R_{eq} + R_{L_1} + j\omega L_{eq}} + j\omega C_p} = R_{inv} + j\omega L_{inv}, \tag{6.20}$$

where R_{inv} and L_{inv} are the inverter equivalent resistance and the inverter equivalent inductance, which are expressed as

$$R_{inv} = \frac{(R_{eq} + R_{L_1})}{\omega^2 C_p^2 \left[(R_{eq} + R_{L_1})^2 + \left(\omega L_{eq} - \dfrac{1}{\omega C_p} \right)^2 \right]}, \tag{6.21}$$

and

$$L_{inv} = \frac{L_{eq}(1-\omega^2 L_{eq}C_p) - C_p(R_{eq}+R_{L_1})^2}{\omega^2 C_p^2 \left[(R_{eq}+R_{L_1})^2 + \left(\omega L_{eq} - \frac{1}{\omega C_p}\right)^2\right]}, \tag{6.22}$$

respectively.

From the transformations described above, the class-E^2 WPT system can be expressed as the typical class-E inverter, whose output network is $L-C-R$ series resonant circuit, as shown in Fig. 5.3(f). Therefore, the analytical expressions in Chapter 3 can be applied to the analysis of the class-E^2 WPT system for comprehending system behavior at any system parameter. In this chapter, the summary of the resulting equation in Chapter 3 are given below.

The inverter current i_{inv} is

$$i_{inv} = I_{inv}\sin(\theta+\phi_{inv}), \tag{6.23}$$

where I_{inv} is the amplitude of the inverter current. The current through the switch is

$$i_S = \begin{cases} 0, & \text{for } 0 \le \theta < \theta_1 \\ I_I - I_{inv}\sin(\theta+\phi_{inv}), & \text{for } \theta_1 \le \theta < \theta_2 \\ 0, & \text{for } \theta_2 \le \theta < 2\pi D_S \\ I_I - I_{inv}\sin(\theta+\phi_{inv}). & \text{for } 2\pi D_S \le \theta < 2\pi \end{cases} \tag{6.24}$$

The switch voltage is obtained as

$$vs = \begin{cases} \dfrac{1}{\omega C_S}\{I_I\theta + I_{inv}[\cos(\theta+\phi_{inv}) - \cos\phi_{inv}]\}, \text{ for } 0 \le \theta < \theta_1 \\ 0, \quad \text{for } \theta_1 \le \theta < \theta_2 \\ \dfrac{1}{\omega C_S}\{I_I(\theta-\theta_2) \\ \qquad + I_{inv}[\cos(\theta+\phi_{inv}) - \cos(\theta_2+\phi_{inv})]\}, \text{ for } \theta_2 \le \theta < 2\pi D_S \\ 0. \text{ for } 2\pi D_S \le \theta < 2\pi \end{cases} \tag{6.25}$$

Because of the assumption d), the dc-voltage drop across the choke inductance L_C is zero. Therefore, the relationship between the dc-supply voltage and the switch voltage can be expressed as

$$V_I = \frac{1}{2\pi D_S}\int_0^{2\pi D_S} v_S d\theta. \tag{6.26}$$

By applying Fourier analyses, the voltage amplitude on the real part and the imaginary part of the output network are

$$R_{inv}I_{inv} = \frac{1}{\pi}\int_0^{2\pi D_S} v_S \sin(\theta+\phi_{inv})d\theta, \tag{6.27}$$

and

$$\left(\omega L_{inv} - \frac{1}{\omega C_1}\right) I_{inv} = \frac{1}{\pi}\int_0^{2\pi D_S} v_S \cos(\theta+\phi_{inv})d\theta, \tag{6.28}$$

respectively. From (6.26), (6.27), and (6.28), I_{inv}, I_I, and ϕ_{inv} can be derived analytically. The amplitude of the inverter current is

$$I_{inv} = \frac{2\pi\omega C_S \beta V_I}{\alpha\delta + \gamma\beta}, \tag{6.29}$$

where

$$\alpha = n_1\cos^2\phi_{inv} + n_2\sin\phi_{inv}\cos\phi_{inv} + n_3, \tag{6.30}$$

$$\beta = n_4 \cos \phi_{inv} + n_5 \sin \phi_{inv}, \tag{6.31}$$

$$\gamma = n_6 \cos \phi_{inv} + n_7 \sin \phi_{inv}, \tag{6.32}$$

and

$$\delta = \frac{1}{2}\theta_1^2 + \frac{1}{2}\theta_2^2 + 2\pi^2 D_S^2 - 2\pi D_S \theta_2. \tag{6.33}$$

The coefficients n_k in (6.30)–(6.33) are

$$\begin{aligned} n_1 =& \frac{1}{2}\cos(2\theta_1) - \cos\theta_1 + \frac{1}{2}\cos(4\pi D_S) + \frac{1}{2}\cos(2\theta_2) + \frac{1}{2} \\ & - \cos\theta_2 \cos(2\pi D_S) + \sin\theta_2 \sin(2\pi D_S), \end{aligned} \tag{6.34}$$

$$\begin{aligned} n_2 =& -\frac{1}{2}\sin(2\theta_1) + \sin\theta_1 - \frac{1}{2}\sin(4\pi D_S) - \frac{1}{2}\sin(2\theta_2) \\ & + \sin\theta_2 \cos(2\pi D_S) + \cos\theta_2 \sin(2\pi D_S), \end{aligned} \tag{6.35}$$

$$\begin{aligned} n_3 =& -\frac{1}{4}\cos(2\theta_1) - \frac{1}{4}\cos(4\pi D_S) - \frac{1}{4}\cos(2\theta_2) + \pi\omega C_S R_{inv} + \frac{3}{4} \\ & - \sin\theta_2 \sin(2\pi D_S), \end{aligned} \tag{6.36}$$

$$\begin{aligned} n_4 =& -\theta_1 \cos\theta_1 + \sin\theta_1 + (\theta_2 - 2\pi D_S)\cos(2\pi D_S) \\ & + \sin(2\pi D_S) - \sin\theta_2, \end{aligned} \tag{6.37}$$

$$\begin{aligned} n_5 =& \theta_1 \sin\theta_1 + \cos\theta_1 + (2\pi D_S - \theta_2)\sin(2\pi D_S) \\ & + \cos(2\pi D_S) - \cos\theta_2 - 1, \end{aligned} \tag{6.38}$$

$$n_6 = \sin\theta_1 + \sin(2\pi D_S) - \sin\theta_2 + (\theta_2 - 2\pi D_S)\cos\theta_2 - \theta_1, \tag{6.39}$$

and

$$n_7 = \cos\theta_1 + \cos(2\pi D_S) + (2\pi D_S - \theta_2)\sin\theta_2 - \cos\theta_2 - 1. \tag{6.40}$$

The input current is expressed as

$$I_I = \frac{2\pi\omega C_S \alpha V_I}{\alpha\delta + \gamma\beta}. \tag{6.41}$$

Additionally, the phase shift between the driving signal and the inverter current is obtained by solving the following algebraic equation:

$$\begin{aligned}(n_4 n_3 + n_5 n_{10}) \tan^3 \phi_{inv} + (n_2 n_4 + n_3 n_9 - n_3 n_5 + n_4 n_{10}) \tan^2 \phi_{inv}\\ +(n_1 n_4 - n_2 n_5 + n_4 n_9 + n_5 n_8 + n_3 n_4 + n_5 n_{10}) \tan \phi_{inv}\\ +(n_4 n_8 - n_1 n_5 - n_3 n_5 + n_4 n_{10}) = 0,\end{aligned} \tag{6.42}$$

where

$$\begin{aligned}n_8 =& -\frac{1}{2}\sin(2\theta_1) + \sin\theta_1 - \frac{1}{2}\sin(4\pi D_S) - \frac{1}{2}\sin(2\theta_2)\\ &+ \cos\theta_2 \sin(2\pi D_S) + \sin\theta_2 \cos(2\pi D_S),\end{aligned} \tag{6.43}$$

$$\begin{aligned}n_9 =& -\frac{1}{2}\cos(2\theta_1) + \cos\theta_1 - \frac{1}{2}\cos(2\theta_2) - \frac{1}{2}\cos(4\pi D_S) - \frac{1}{2}\\ &+ \cos\theta_2 \cos(2\pi D_S) - \sin\theta_2 \sin(2\pi D_S),\end{aligned} \tag{6.44}$$

and

$$\begin{aligned}n_{10} =& -\frac{\theta_1}{2} + \frac{\theta_2}{2} + \frac{1}{4}\sin(2\theta_2) + \frac{1}{4}\sin(4\pi D_S) - \frac{1}{4}\sin(2\theta_2) - \pi D_S\\ &- \sin\theta_2 \cos(2\pi D_S) + \sin\theta_2 \cos\theta_2 + \pi\left(\omega^2 L_{inv} C_S - \frac{C_S}{C_1}\right).\end{aligned} \tag{6.45}$$

Newton's method is used for solving the algebraic equations in this study.

Additionally, the relationship between I_{inv} and I_1 is expressed as

$$I_1 = \sqrt{\frac{R_{inv}^2 + \omega^2 L_{eq}^2}{(R_{eq} + R_{L_1})^2 + \omega^2 L_{eq}^2}} I_{inv}. \tag{6.46}$$

The waveform equations given in this section are valid for all the switching patterns in Cases 1, 2, and 3. For obtaining the waveforms, we firstly need to derive the inverter parameters, namely I_{inv}, I_I, and ϕ_{inv}, from the circuit parameters. In this process, it is necessary to derive θ_1 and θ_2, which are obtained numerically following the calculation algorithms given in Chapter 3.

6.4 Output Power and Power Delivery Efficiency

In real circuits, the power losses occur in ESRs of passive elements, MOSFET on-resistance, diode in the rectifier, and MOSFET body diode. It is assumed in this study that the parasitic resistances and the diode forward voltage drop are small enough not to affect the waveforms [3], [4]. Figure 6.1 shows the equivalent circuit model for the power-loss calculations. In this study, the power losses in MOSFET on-resistance, rectifier and MOSFET-body diodes due to the forward voltage drops, and ESRs of inductances are considered.

The output power is obtained from

$$P_o = R_L I_o^2. \tag{6.47}$$

The conduction loss in the MOSFET on-resistance r_S is

$$\begin{aligned} P_S &= \frac{r_S}{2\pi}\int_0^{2\pi} i_S^2 d\theta = \frac{r_S}{2\pi}\int_{2\pi D_S}^{2\pi} i_S^2 d\theta \\ &= \frac{r_S}{2\pi}\left\{2\pi(1-D_S)I_I^2 + 2I_I I_{inv}[\cos\phi_{inv} - \cos(2\pi D_S + \phi_{inv})]\right. \\ &\left. + \frac{I_{inv}^2}{4}\left[4\pi(1-D_S) + \sin(4\pi D_S + 2\phi_{inv}) - \sin 2\phi_{inv}\right]\right\}. \end{aligned} \tag{6.48}$$

The power losses in the inductances are

$$P_{L_1} = \frac{R_{L_1} I_1^2}{2},\ P_{L_2} = \frac{R_{L_2} I_2^2}{2},\ P_{L_C} = r_{L_C} I_I^2,\ \text{and } P_{L_f} = r_{L_f} I_o^2. \tag{6.49}$$

The power loss in the diode of the rectifier is

$$\begin{aligned} P_D &= \frac{V_{th}}{2\pi}\int_0^{2\pi} i_D\ d\theta_{rec} = \frac{V_{th}}{2\pi}\int_{2\pi(1-D_d)}^{2\pi} i_D \theta_{rec} \\ &= \frac{V_{th} I_o}{2\pi}\left\{2\pi D_d + \frac{\cos\phi_d - \cos(\phi_d - 2\pi D_d)}{\sin\phi_d}\right\}, \end{aligned} \tag{6.50}$$

where V_{th} is the forward voltage drop of the diode. Additionally, power losses in the MOSFET should be considered. In Cases 1 and 3, the turn-on switching losses occur, which is expressed as

$$\begin{aligned}P_{SW} &= \frac{1}{2}C_S f v_S^2(2\pi D_S^-)\\ &= \frac{1}{4\pi\omega C_S}\Big\langle \theta_1^2 I_I^2 + 2\theta_1 I_I I_{inv}[\cos(\theta_1+\phi_{inv}) - \cos\phi_{inv}]\\ &\quad + I_{inv}^2[\cos(\theta_1+\phi_{inv}) - \cos\phi_{inv}]^2 + (2\pi D_S - \theta_2)^2 I_I^2\\ &\quad + 2I_{inv}I_I\{(2\pi D_S - \theta_2)[\cos(2\pi D_S + \phi_{inv}) - \cos(\theta_2+\phi_{inv})]\}\\ &\quad + I_{inv}^2[\cos(2\pi D_S+\phi_{inv}) - \cos(\theta_2+\phi_{inv})]^2\Big\rangle. \end{aligned} \tag{6.51}$$

(6.51) expresses the switching loss of all the switching patterns. In Case-2 and Case-3 switching patterns, the MOSFET body diode turns on and the conduction loss in the MOSFET body diode should be considered. The MOSFET-body-diode conduction loss is

$$\begin{aligned}P_{D_b} &= \frac{1}{2\pi}\int_0^{2\pi} V_{thb} i_S d\theta = \frac{1}{2\pi}\int_{\theta_1}^{\theta_2} V_{thb} i_S d\theta\\ &= \frac{V_{thb}}{2\pi}\Big\{ I_I(\theta_2 - \theta_1) + I_{inv}[\cos(\theta_2+\phi_{inv}) - \cos(\theta_1+\phi_{inv})]\Big\},\end{aligned} \tag{6.52}$$

where V_{thb} is the forward voltage drop of the body diode. From the above considerations, the total power loss of the class-E^2 WPT system is

$$P_{loss} = P_S + P_{L_1} + P_{L_2} + P_{L_C} + P_{L_f} + P_D + P_{SW} + P_{D_b}. \tag{6.53}$$

From (6.47) and (6.53), the power-delivery efficiency can be obtained analytically as

$$\eta = \frac{P_o}{P_o + P_{loss}} \tag{6.54}$$

The analytical power-delivery efficiency is valid at any system parameter, namely for all the switching patterns.

6.5 Experimental Verification

6.5.1 Nominal State

For validating the analytical expressions, PSpice simulations and circuit experiments were carried out. The design specifications of the WPT system were given as follows: dc-supply voltage $V_I = 20\ V$, operating frequency $f = 1$ MHz, output power $P_o = 5$ W, load resistance $R_{Lnom} = 50\ \Omega$, MOSFET-off duty ratio $D_S = 0.5$, diode-on duty ratio $D_d = 0.5$, and distance between the primary and the secondary coils $d_{coils} = 7$ cm.

Additionally, the coupled coil parameters were given. The circle-shape coils were made for coupled coils whose diameter $d = 15.5$ cm, number of turns $N = 8$, and layer number $N_l = 1$. One layer coils were adopted because the proximity effect can be reduced [21]. Additionally, the Litz wire (KERRIGAN LEWIS WIRE) was used as winding wire for the skin effect reduction [21]. The parameters of the primary coil were the same as those of the secondary one in this experiment. The self inductances and the ESRs of the coils were measured by HP4284A LCR meter, which were $L_1 = 23.1\ \mu$H, $L_2 = 22.7\ \mu$H, $R_{L_1} = 0.891\ \Omega$, and $R_{L_2} = 0.829\ \Omega$ at 1 MHz, respectively. Figure 6.2(a) explains the distance between the primary and the secondary coils d_{coils} and the transverse offset h_{coils}. When these coils are coupled with $d_{coils} = 7$ cm and $h_{coils} = 0$ cm, which is given as the specified position, the coupling coefficient was measured as $k_{nom} = 0.100$. We investigated the coupling coefficient when the position misalignment occurs from the specified position. Figure 6.2(b) shows the measured values of coupling coefficients as functions of d_{coils} for $h_{coils} = 0$ cm and h_{coils} for $d_{coils} = 7$ cm. It is seen from the analytical expressions that the WPT system performance can be expressed as a function of coupling coefficient. The physical position relationship between the primary and secondary coils can be transformed to the coupling coefficient from Fig. 6.2(b). Therefore, we show system characteristics as functions of coupling coefficient in the following results.

The design of the class-E^2 WPT system with the given design specifications was carried out following the design procedure in [8]. From the analytical waveforms, the maximum switch and diode voltages were predicted as $V_{Smax} = 71.2$ V and $V_{Dmax} = 56.3$ V [1]. Therefore, the IRF530 MOSFET and the STPS5H100B Schottky Barrier Diode, whose breakdown voltages are 100 V, were selected as the switching devices. From the datasheets, MOSFET on-resistance, forward-voltage drops of the MOSFET body diode, and that of the rectifier diode were obtained as $r_S = 0.16\ \Omega$, $V_{thb} = 2.5$ V, and $V_{th} = 0.61$ V, respectively. From the assumption c), the analytical shunt capacitances include the parasitic capacitance of the switching devices. The parasitic capacitances of the IRF530 and the STPS5H100B were estimated to be 350 pF and 150 pF, respectively, which were also obtained from the datasheets. Figure 6.3(a) shows the overview of the implemented WPT system.

Table 6.1 gives the analytical predictions and experimental measurements of the WPT system for the design specifications. In Table 6.1, input voltage V_I, input current I_I, and output voltage V_o were measured by Iwatsu VOAC7523. In addition, the power delivery efficiency was measured by

$$\eta = \frac{P_o}{P_I} = \frac{V_o^2}{R_L V_I I_I}, \tag{6.55}$$

where P_I is the dc-supply power. Figure 6.3(b) shows the waveforms of the designed WPT system obtained from analysis, PSpice simulation, and experiment with the specified parameters. It is seen from Fig. 6.3(b) that all the switch-voltage waveforms of the class-E inverter and those of the class-E rectifier satisfied the class-E ZVS/ZDS conditions. We define the state in Table 6.1 and Fig. 6.3(b) as the nominal state. In the experimental measurement for nominal operation, 80.8 % power-delivery efficiency was achieved at 4.90 W output power at 1 MHz operation. At the following investigations, system parameters varied from the nominal state.

6.5.2 Predictions of ZVS Region From Analytical Expressions

Because the class-E^2 WPT system can be modeled as a typical topology of the class-E inverter as discussed in Section 6.3, the ZVS region of the inverter can be predicted from the inverter output network. Figure 6.4 shows the equivalent inverter resistance and inductance as functions of the coupling coefficient and the load resistance, which are normalized by their nominal values. The other parameters are fixed at the design specifications. It is seen form Fig. 6.4 that R_{inv} decreases from the nominal value when the coupling coefficient decreases or load resistance increases from the nominal state. It is also seen that L_{inv} is almost constant with the decrease in k and the increase in R_L. Therefore, it can be analytically predicted that the class-E^2 WPT system achieves the ZVS in the region of $k/k_{nom} < 1$ and $R_L/R_{Lnom} > 1$.

6.5.3 Output Power and Power Delivery Efficiency

Figure 6.5 shows the output power and power-delivery efficiency as a function of the normalized coupling coefficient. Additionally, the switching patterns are marked on Fig. 6.5. It is seen from Fig. 6.5 that both the output power and the power delivery efficiency are sensitive to the coupling coefficient. It can be also confirmed that both the output power and the power-delivery efficiency decrease even if the coupling coefficient is larger than that for the nominal state. For $k/k_{nom} > 1$, R_{inv} increases from its nominal value as shown in Fig. 6.4(a), which is the reason of the decrease in the output power. In addition, non-ZVS with the Case-1 switching pattern appears at the inverter for $k/k_{nom} > 1$. Therefore, the power-delivery efficiency decreases because of the switching loss in this region. It is also seen from Fig. 6.5(a) that the output power decreases as the coupling coefficient decreases from the nominal state. This is because the induced voltage V_{ind} decreases as the coupling coefficient decreases, which is confirmed from (6.18). On the other hand, the ZVS is achieved for $k/k_{nom} < 1$, which agrees with the analytical predictions as described in Subsection 6.5-B. However, the power-delivery efficiency decreases for $k/k_{nom} < 1$. This is because the equivalent resistance of the coupled coils and the rectifier R_{eq} decreases in this region. The power-conversion efficiency of the inverter in the WPT system can be approximated as $R_{eq}/(R_{eq} + R_{L_1})$ when the switching loss is negligible. Therefore, the power-delivery efficiency decreases as the coupling coefficient decreases even if the ZVS is achieved for $k/k_{nom} < 1$.

Figure 6.6 shows the output power and power-delivery efficiency as a function of the normalized load resistance. It is seen from Fig. 6.6 that the class-E inverter always achieves the ZVS when the load resistance is larger than the nominal value, which agrees with the analytical prediction in Subsection 6.5-B. Additionally, for $R_L/R_{Lnom} > 1$, R_{eq} decreases slightly. Therefore, high power-delivery efficiency can be kept for $R_L/R_{Lnom} > 1$ as shown in Fig. 6.6(b). It is seen from Fig. 6.6(a) that the output power almost constant for $R_L/R_{Lnom} > 1$. This is because the increase in L_{inv} causes the decrease in the resonant frequency, which cancels out the effect of the increase in the output power due to the decrease in R_{inv}. As a result, the inverter current and the output power is almost constant for $R_L/R_{Lnom} > 1$ though R_{inv} decreases. It is seen from Fig. 6.6(a) that the output power increases as R_L decreases. It is known that the output filter, namely $C_1 - L_{inv}$, should be inductive for achieving the class-E ZVS/ZDS conditions. Due to the decrease in L_{inv} for $R_L/R_{Lnom} < 1$, the resonant frequency of the output filter approaches the operating frequency, which leads to the increase in the output power. In addition, R_{inv} decreases for $R_L/R_{Lnom} < 0.75$, which also lets the output power increase. Additionally, it is also confirmed from Fig. 6.6(a) that the output power sharply decreases for $R_L/R_{Lnom} < 0.2$. This is because the equivalent capacitance of the rectifier C_i sharply increases from that of the nominal state.

It is seen from Figs. 6.5 and 6.6 that the analytical predictions of the output power and the power-delivery efficiency agreed with the PSpice-simulation and the experimental results quantitatively, which validated the accuracy and effectiveness of the analytical expressions in this chapter. As shown in above discussions, much information of the class-E^2 WPT system can be obtained from the analytical expressions, which shows usefulness and effectiveness of the analytical expressions.

6.6 Distribution of Switching Patterns

Because the switching pattern can be obtained from the analytical expressions, it is possible to obtain switching-pattern distribution maps, which is one of the applications of the analytical expressions. From the switching-pattern distribution maps, important information can be obtained. Figure 6.7(a) shows the switching-pattern distribution of the inverter on $k/k_{nom} - R_L/R_{Lnom}$ plane.

It is seen from Fig. 6.7(a) that the Case-2 region for any load resistance appears at $k/k_{nom} < 0.75$. This result indicates that the ZVS WPT system at any load resistance can be designed. Figure 6.8(a) shows an algorithm for the ZVS WPT system design, where k_{max} is the maximum coupling coefficient on an implemented system. As a design example, we set $k_{max} = 0.100$ and the same design specifications as those in Section 6.5. By using the algorithm in Fig. 6.8(a), $k_{nom} = 0.132$ was obtained. Figure 6.8(b) shows the switching-pattern distribution for the designed ZVS WPT system. In the designed system, ZVS is always achieved at any load resistance in the region of $k/k_{max} \leq 1$, which was also confirmed by the PSpice simulation. The above discussion is a good example to state that the analytical expressions are powerful tools for obtaining important information on the class-E^2 WPT system.

Figures 6.7(b), (c), and (d) show the analytical, PSpice-simulation, and experimental waveforms for the Case-1, Case-2, and Case-3 switching patterns. Each parameter set is marked on Fig. 6.7(a). It can be confirmed from these waveforms that all the switching patterns of the analytical waveforms agreed with those of simulation and experimental ones, which showed the validity of the switching-pattern distribution map in Fig. 6.7(a) and the accuracy of the analytical waveform expressions.

6.7 Conclusion

This chapter has presented the analytical expressions of the class-E^2 WPT system for any system parameter. By considering non-nominal operations of the class-E inverter, system behavior at any system-parameter set can be expressed accurately. In this chapter, output power, power-delivery efficiency, and state of switching-pattern as functions of system parameters have been shown. The important characteristics of the WPT system, which are clarified from the analytical expressions, are that the transmitter of the class-E^2 WPT system always achieves ZVS when the coupling coefficient decreases or the load resistance increases from the nominal state. Additionally, the switching-pattern distribution map has been shown, which can be obtained from the analytical waveform equations. By using the distribution map, it is possible to design the WPT system whose transmitter achieves the ZVS at any load resistance. By carrying out PSpice simulations and circuit experiments, it has been shown that the analytical predictions agreed with the PSpice-simulation and experimental results quantitatively, which indicates the validity of the analytical expressions.

Table 6.1: Design Values

	Analytical	Simulated	Measured	Difference*
L_C	276 μH	276 μH	303 μH	9.8 %
L_f	300 μH	300 μH	308 μH	2.7 %
r_{L_C}	-	0.0162 Ω	0.0162 Ω	-
r_{L_f}	-	0.0212 Ω	0.0212 Ω	-
C_S	734 pF	734 pF	757 nF	3.1 %
C_1	571 pF	571 pF	576 pF	0.89 % -
C_p	610 pF	610 pF	609 pF	0.098 % -
C_2	1.46 nF	1.46 nF	1.45 nF	-0.55 % -
C_D	1.01 nF	1.01 nF	997 pF	-1.3 %
C_f	47 μF	47 μF	-	-
R_{Lnom}	50 Ω	50 Ω	50.3 Ω	0.60 %
L_1	-	23.1 μH	23.1 μH	-
L_2	-	22.7 μH	22.7 μH	-
k_{nom}	-	0.100	0.100	-
r_{L_1}	-	0.891 Ω	0.891 Ω	-
r_{L_2}	-	0.829 Ω	0.829 Ω	-
d_{coils}	-	-	7 cm	-
f	1 MHz	1 MHz	1 MHz	0.0 %
D_S	0.5	0.5	-	-
D_d	0.5	-	-	-
V_I	20.0 V	20.0 V	20.0 V	0.0 %
I_I	0.290 V	0.289 V	0.303 V	4.5 %
V_o	15.8 V	15.5 V	15.7 V	-0.70 %
P_o	5.00 W	4.79 W	4.90 W	-2.0 %
η	82.9 %	83.0 %	80.8 %	-2.5 %

* “Difference” is the difference between analytical and experimental results.

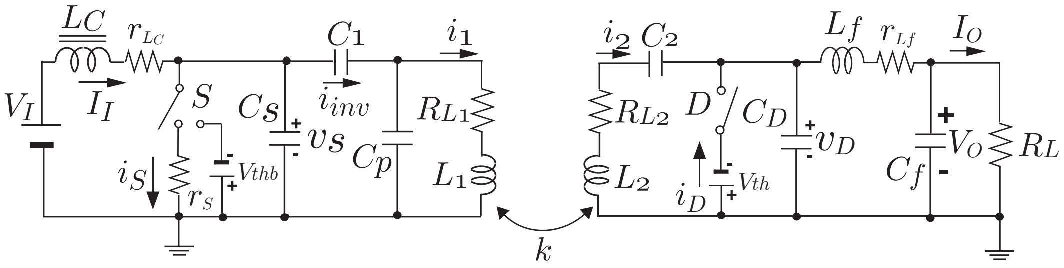

Figure 6.1: Equivalent circuit of class-E^2 WPT system for power-loss calculations.

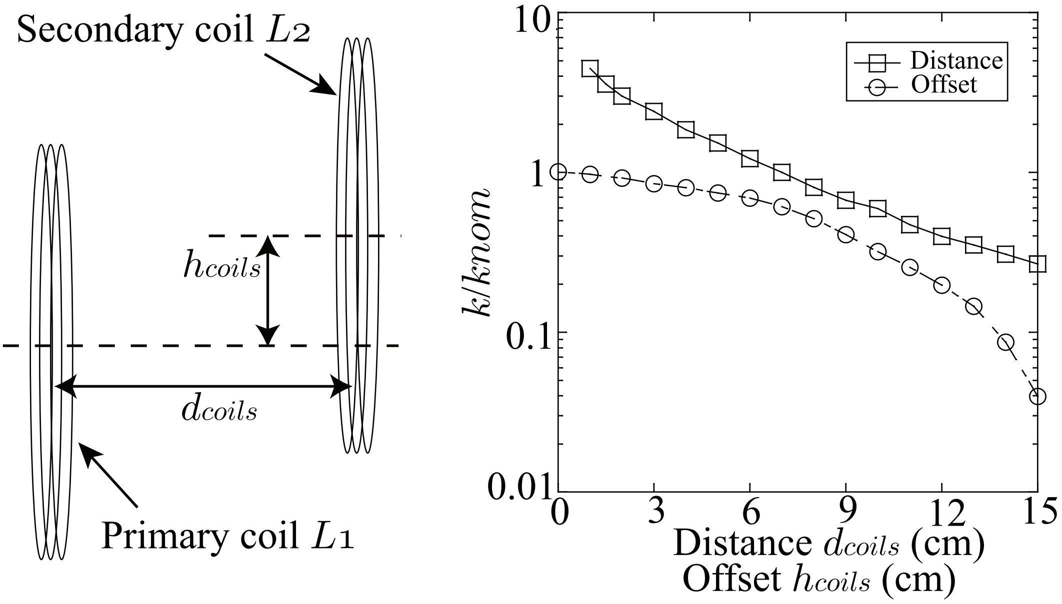

(a)

(b)

Figure 6.2: Measurements of coupling coefficient. (a) Experimental setup for distance and transverse offset measurements. (b) Coupling coefficient as functions of distance and offset.

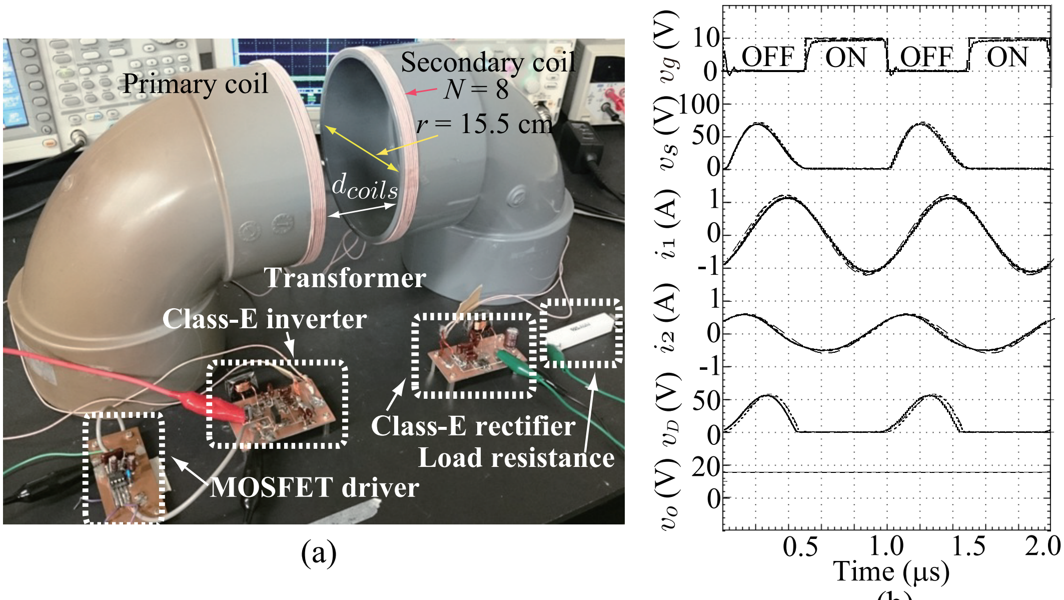

(a) (b)

Figure 6.3: Experimental set up and nominal waveforms. (a) System overview. (b) Analytical(dashed), PSpice(dotted), and experimental(solid) waveforms for the design specifications.

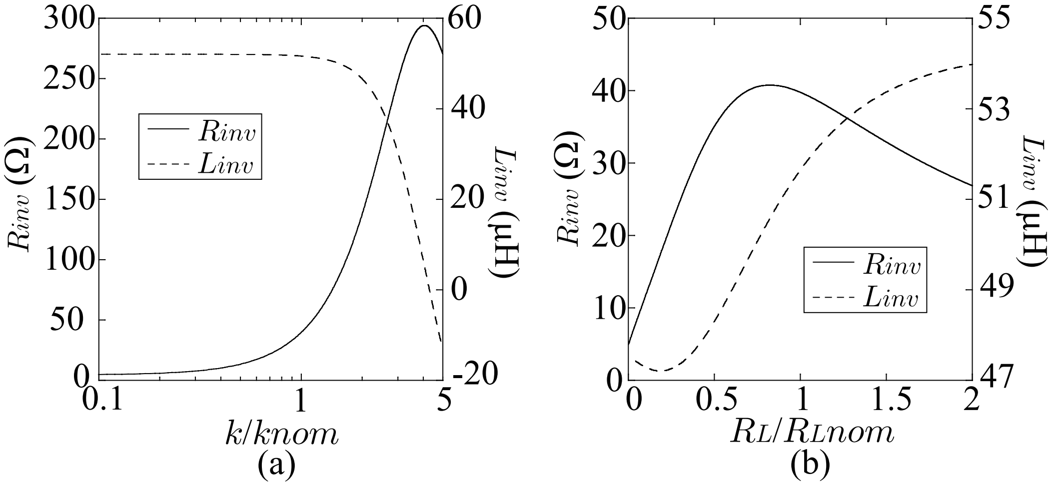

Figure 6.4: Equivalent inverter resistance and inductance as functions of (a) coupling coefficient and (b) load resistance.

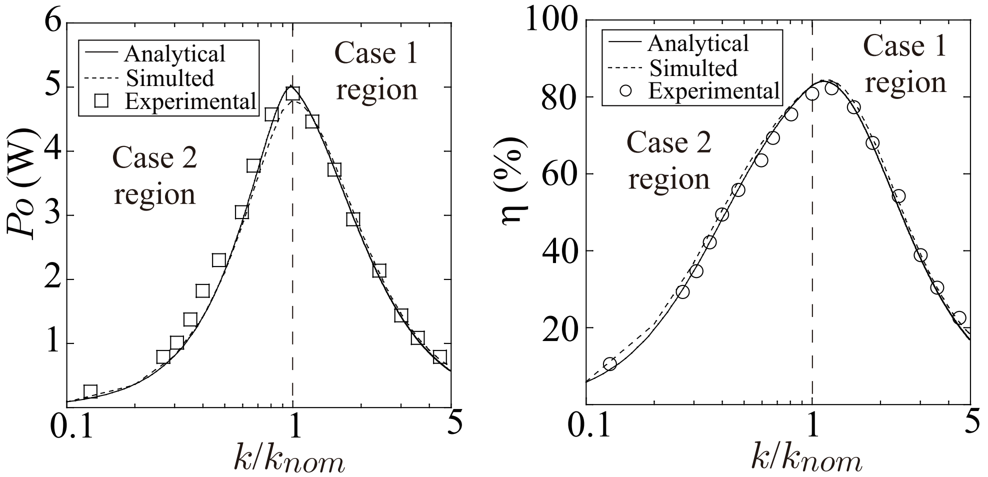

(a) (b)

Figure 6.5: Output power and power delivery efficiency as functions of k/k_{nom}. (a) Output power.(b) Power delivery efficiency.

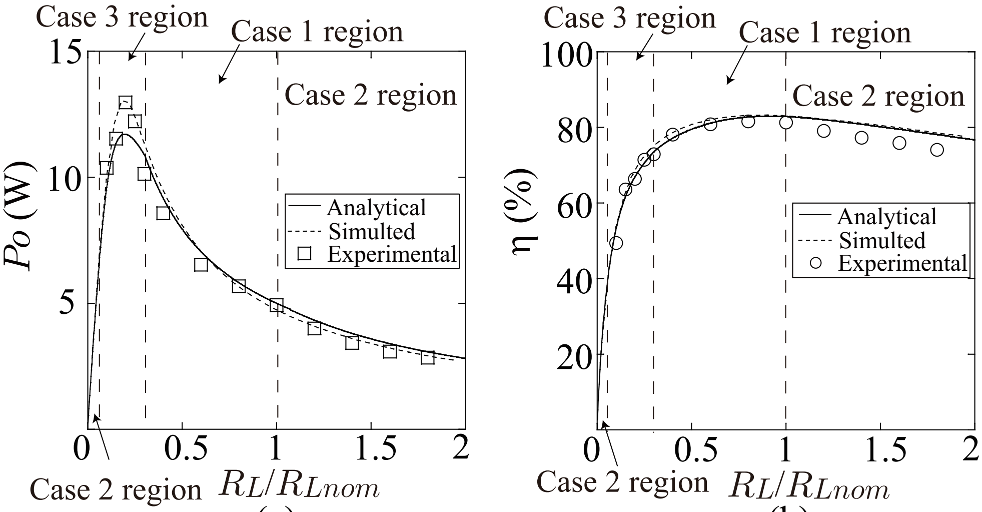

(a) (b)

Figure 6.6: Output power and power delivery efficiency as functions of R_L/R_{Lnom}. (a) Output power.(b) Power delivery efficiency.

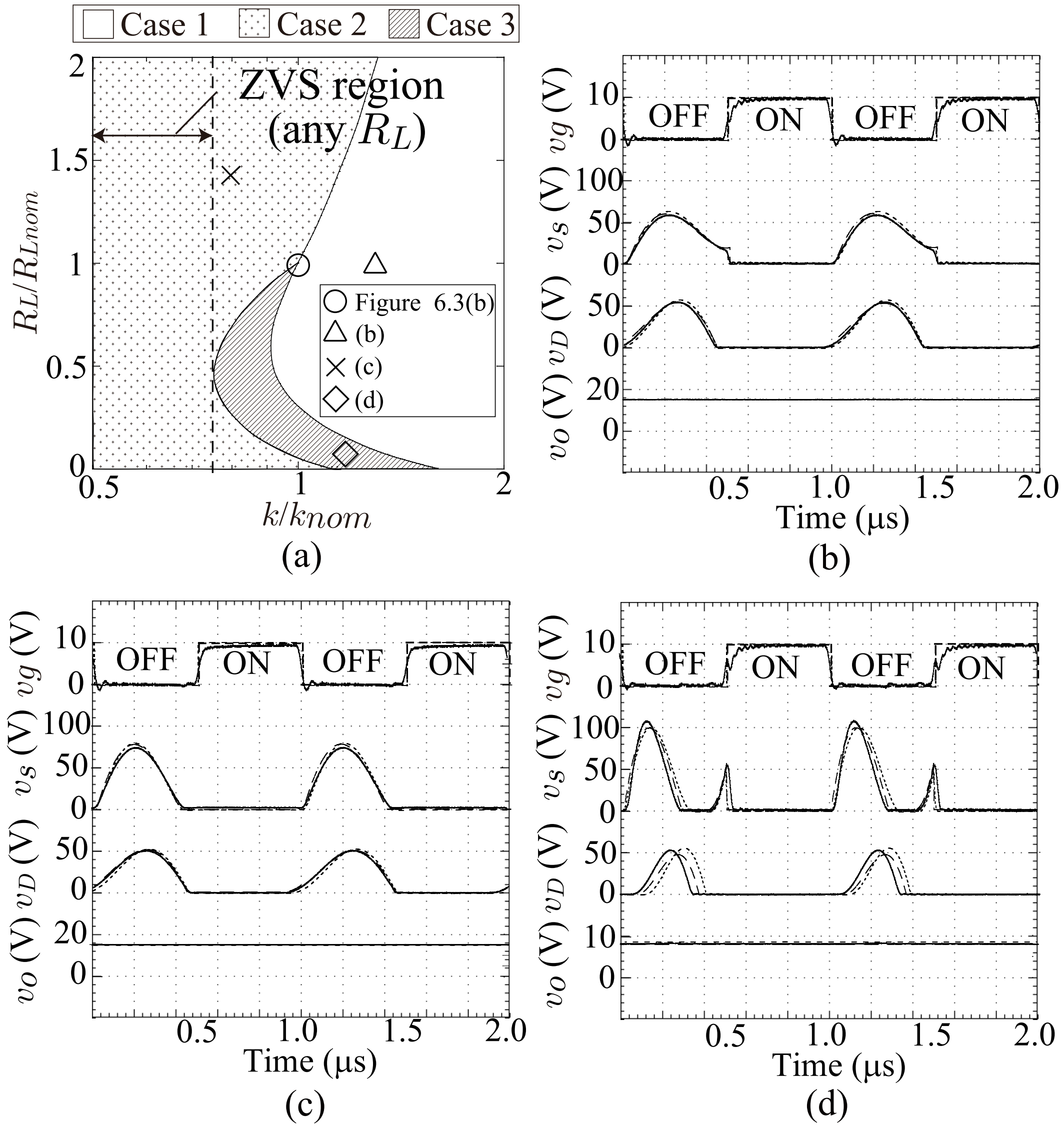

(a) (b) (c) (d)

Figure 6.7: Switching-pattern distribution and waveforms obtained from analytical expressions (dashed line), PSpice simulations (dotted line), and circuit experiments (solid line). (a) Switching-pattern distribution of the inverter on $k/k_{nom} - R_L/R_{Lnom}$ plane. (b) Case 1 waveforms for $k/k_{nom} = 1.22$ ($d_{coils} = 6$ cm) and $R_L/R_{Lnom} = 1$. (c) Case 2 waveforms for $k/k_{nom} = 0.809$ ($d_{coils} = 8$ cm) and $R_L/R_{Lnom} = 1.4$. (d) Case 3 waveforms for $k/k_{nom} = 1.11$ ($d_{coils} = 6.5$ cm) and $R_L/R_{Lnom} = 0.1$

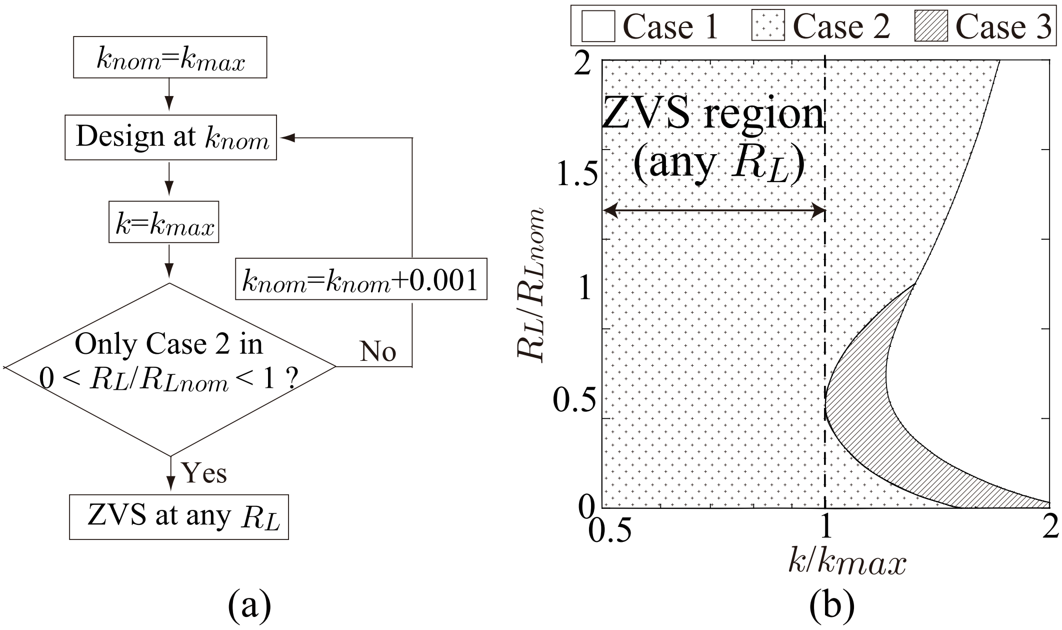

Figure 6.8: Algorithm and designed distribution map. (a) Design algorithm for ZVS WPT system. (b) Designed switching-pattern distribution on $k/k_{max} - R_L/R_{Lnom}$ plane.

References

[1] M. K. Kazimierczuk and J. Jozwik, "Resonant DC/DC converter with class-E inverter and class-E rectifier," *IEEE Trans. Ind. Electron.,* vol. 36, no. 4, pp. 468–478, Nov. 1989.

[2] J. Jozwik and M. K. Kazimierczuk, "Analysis and design of class-E^2 DC/DC converter," *IEEE Trans. Ind. Electron.,* vol. 37, no. 2, pp. 173–183, Apr. 1990.

[3] D. J. Kessler and M. K. Kazimierczuk, "Power losses and efficiency of class-E power amplifier at any duty ratio," *IEEE Trans. Circuits Syst.-I*, vol. 51, no. 9, pp. 1675–1689, Sept. 2004.

[4] X. Wei, H. Sekiya, S. Kuroiwa, T. Suetsugu, and M. K. Kazimierczuk, "Design of class-E amplifier with MOSFET linear gate-to-drain and nonlinear drain-to-source capacitances," *IEEE Trans. Circuits Syst.-I*, vol. 58, no. 10, pp. 2556–2565, Oct. 2011.

[5] M. K. Kazimierczuk, "Analysis of class E zero-voltage switching rectifier," *IEEE Trans Circuit Syst.,* vol. 37, no. 6, pp. 747–755, Jun. 1990.

[6] Y. Kamito, K. Fukui, and H. Koizumi, "An analysis of the class-E zero-voltage-switching rectifier using the common-grounded multistep-controlled shunt capacitor," *IEEE Trans. Power Electron.,* vol. 29, no. 9, pp. 4807–4816, Sept. 2014.

[7] T. Nagashima, K. Inoue, X. Wei, E. Bou, E. Alarcon, and H. Sekiya, "Inductively coupled wireless power transfer with class-E^2 DC-DC converter," *in Proc. European Conference on Circuit Theory and Design (ECCTD),* Sept. 2013.

[8] T. Nagashima, K. Inoue, X, Wei, E. Bou, E. Alarcon, M. K. Kazimierczuk, and H. Sekiya, "Analytical design procedure for resonant inductively coupled wireless

power transfer with class-E^2 DC-DC converter" *in Proc. IEEE ISCAS,* Jun. 2014, pp. 113–116.

[9] S. Aldhaher, P. Luk, K. Drissi, and J. Whidborne, "High input voltage high frequency class E rectifiers for resonant inductive links," *IEEE Trans. Power Electron.,* vol. 30, no. 3, pp. 1328–1335, Mar. 2015.

[10] P. Luk, S. Aldhaher, W. Fei, and J. Whidborne, "State-space modelling of a class E^2 converter for inductive links," *IEEE Trans. Power Electron.,* vol. 30, no. 6, pp. 3242–3251, Jun. 2015.

[11] A. Kurs, A. Karalis, R. Moffatt, J. D. Joannopoulos, P. Fisher, and M. Soljacic, "Wireless power transfer via strongly coupled magnetic resonances," *Sci. Express,* vol. 317, no. 5834, pp. 83–86, Jul. 2007.

[12] A. P. Sample, D. A. Meyer, and J. R. Smith, "Analysis, experimental results, and range adaptation of magnetically coupled resonators for wireless power transfer," *IEEE Trans. Ind. Electron.,* vol. 58, no. 2, pp. 544–554, Feb. 2011.

[13] M. Kiani and M. Ghovanloo, "The circuit theory behind coupled-mode magnetic resonance-based wireless power transmission," *IEEE Trans. Circuits Syst.-I* vol. 59, no. 9, pp. 2065–2074, Sept. 2012.

[14] J. Sallan, J. L. Villa, A. Llombart, and J. F. Sanz, "Optimum design of ICPT systems applied to electric vehicle battery charge," *IEEE Trans. Ind. Electron.,* vol. 56, no. 6, pp. 2140–2149, Jun. 2009.

[15] S. Y. Hui, "Planar wireless charging technology for portable electronic products and Qi," *in Proc. of the IEEE,* vol. 101, no. 6, pp. 1290–1301, Jun. 2013.

[16] R. Xue, K. Cheng, and M. Je, “High-efficiency wireless power transfer for biomedical implants by optimum resonant load transformation,” *IEEE Trans. Circuits Syst.-I* vol. 60, no. 4, pp. 867–874, Apr. 2013.

[17] D. Ahn, and S. Hong, “Wireless power transmission with self-regulated output voltage for biomedical implant,” *IEEE Trans. Ind. Electron.,* vol. 61, no. 5, pp. 2225–2235, May 2014.

[18] T. C. Beh, M. Kato, T. Imura, S. Oh, and Y. Hori, “Automated impedance matching system for robust wireless power transfer via magnetic resonance coupling,” *IEEE Trans. Ind. Electron.,* vol. 60, no. 9, pp. 3689–3698, Sep. 2013.

[19] M. Fu, C. Ma, and X. Zhu, “A cascaded boost-buck converter for high efficiency wireless power transfer systems,” *IEEE Trans. Ind. Informatics,* vol. 10, no. 3, pp. 1972–1980, Aug. 2014.

[20] H. Li, J. Li, K. Wang, and X. Yang, “A maximum efficiency point tracking control scheme for wireless power transfer systems using magnetic resonant coupling,” *IEEE Trans. Power Electron.,* to be published.

[21] M. K. Kazimierczuk and H. Sekiya, “Design of AC resonant inductors using area product method,” *in Proc. IEEE ECCE*, Sept. 2009, pp. 994–100.

Chapter 7

Overall Conclusion and Future Problems

7.1 Overall Conclusion

This thesis presents analyses and designs of the class-E switching circuits for WPT system.

Chapter 2 has been dedicated to the basics of the inductive coupling WPT system. It has started off with a summary of magnetic induction theory and then delves into coupling states of coils, which are the loosely inductive coupling and the resonant inductive coupling. The resonant class-D and -E inverters and the class-E oscillator along with the injection-lock technique have been introduced as dc-ac inverters. Additionally, the class-D and -E rectifiers have been shown as ac-dc converters.

In Chapter 3, analytical expressions for steady-state waveforms, output power, and power conversion efficiency of the class-E inverter outside the class-E ZVS/ZDS conditions at a high Q and any duty ratio have been presented, taking into account MOSFET-body-diode effect. By considering the switch-voltage recovery during the MOSFET body diode on-state, the applicable parameter range of the analytical expressions is much wider than that of the previous analytical expressions. By carrying out the PSpice simulations and the circuit experiments, it was shown that the analytical predictions agreed with the simulated and the experimental results quantitatively, which validates accuracy of our analytical expressions. Additionally, the switching-pattern distribution maps have been also shown, which can be obtained from the waveform equations.

In Chapter 4, a numerical locking-range prediction for the injection-locked class-E oscillator using the phase reduction theory (PRT) has been presented. This high power-conversion efficiency oscillator can be utilized in WPT systems. By applying this PRT to the injection-locked class-E oscillator designs, the locking ranges of the oscillator on any injection-signal waveform can be efficiently obtained. The locking ranges obtained from the proposed method quantitatively agreed with those obtained from the simulations and circuit experiments, showing the validity and effectiveness of the locking-range derivation method based on PRT.

In Chapter 5, an analytical design procedure and an efficiency-enhancement theory for the loosely inductive coupling (LIC) WPT system with class-E^2 dc-dc converter, which consists of the class-E inverter and the class-E rectifier, have been presented. By using the analytical expressions, it is possible to obtain component values of the class-E^2 WPT system for achieving the class-E ZVS/ZDS conditions. Additionally, the analytical expressions suggest designers how to determine the component values for power-delivery efficiency enhancement. I proposed that the component values of the rectifier are used for the power-delivery efficiency enhancement and the output power is adjusted by the inverter component values. The analytical predictions agreed with the PSpice-simulation and experimental results quantitatively, which showed the validities of the analytical expressions and the design procedure. In the laboratory experiment, the WPT system for 10 cm coil distance achieved 77.1 % power-delivery efficiency with 10 W (50 Ω/22.4 V) output power at 1 MHz operating frequency.

In Chapter 6, analytical expressions of the class-E^2 WPT system at any system parameter have been presented. By considering non-nominal operations of the class-E inverter, system behavior at any system-parameter set can be expressed accurately. For example, the output power and the power-delivery efficiency as functions of coupling coefficient and load resistance have been given. It was clarified from the analytical expressions that the ZVS condition is always satisfied when the coupling coefficient decreases or the load resistance increases from the nominal value. Additionally, the switching-pattern distribution map of the class-E^2 WPT system in a parameter space has been illustrated from the analytical expressions. By using the distribution map, the WPT system achieving the ZVS at any load resistance conditions can be designed, which is one of the applications of the analytical expressions. The analytical predictions agreed with the PSpice-simulation and experimental results quantitatively, which showed the validities of the analytical expressions.

These results enhance the power-delivery efficiency of the WPT systems and give designers the comprehension of system performances. It is expected that the results in this thesis contribute to efficient-energy usage and comprehensive understanding in WPT systems.

7.2 Future Problems

There are continuous research topics, which should be addressed in the future. The following topics are suggested for future works.

1. Output power control for class-E^2 WPT system

One of the main objectives of this thesis is the design of the class-E^2 WPT system for enhancing the power-delivery efficiency. It is, however, necessary to implement output-power control circuits for the practical usage of the WPT system. There are several output-power control techniques for the class-E inverter and the class-E rectifier. By using the analytical expressions in Chapter 6, system behaviors of the class-E^2 WPT system with output controls may be expressed analytically. Further research and investigation of the implementation is required for the practical usage of the class-E^2 WPT system.

2. Optimal design including coupling part

This thesis focuses on the optimal designs of the power converters. The parameters of the inductive coupled coils were given as the design specifications in this thesis. In the WPT systems, however, the design of the inductive coupling part is also important for enhancing the power-delivery efficiency. There has been few researches about the optimization of the whole system. Optimal design of the class-E^2 WPT system including coupling part is one of challenging researches.

3. Implementation of high-frequency WPT systems

In this thesis, the 1 MHz class-E^2 WPT system were implemented and demonstrated. The efficiency of the coupling part increases as the operating frequency increases. At higher frequencies, however, it is necessary to design a complex MOSFET driver circuit for high power WPT systems. This is a challenging problem. In addition, silicon carbide (SiC) and gallium-nitride (GaN) high-electron-mobility transistor (HEMT) devices may be suitable for higher frequency WPT systems instead of MOSFETs. Using these devices leads to a low power-loss property of the switching devices at high frequencies. The implementation of these devices for WPT systems is also one of the challenging researches. Of course, it is also necessary the comparison of the characteristics between the WPT system with class-E inverter and that with the injection-locked class-E oscillator.

I would like to keep carrying out researches and contribute to accelerating the practical uses of WPT systems.

List of Related Papers by The Author

Journal Papers

[1] Tomoharu Nagashima, Xiuqin Wei, Takuji Kousaka, and Hiroo Sekiya, "Bifurcation analysis of the class-E inverter for switching-pattern derivations," *IEICE Communications Express (ComEX),* vol. 1, No. 1, pp. 33–39, Jun. 2012.

[2] Tomoharu Nagashima and Hiroo Sekiya, "Steady-state behavior of class-E amplifier outside nominal operation taking into account MOSFET-body-diode effect," *Journal of Signal Processing,* vol. 16, No. 4, pp. 287–290, Jul. 2012.

[3] Xiuqin Wei, Shingo Kuroiwa, Tomoharu Nagashima, Marian K. Kazimierczuk, and Hiroo Sekiya, "Push-Pull class-E_M power amplifier for low harmonic-contents and high output-power applications," *IEEE Transactions on Circuits and Systems Part I: Regular Papers,* vol. 59, no. 9, pp. 2137–2146, Sept. 2012,

[4] Ryosuke Miyahara, Xiuqin Wei, Tomoharu Nagashima, Takuji Kousaka, and Hiroo Sekiya, "Design of class-E_M oscillator with second harmonic injection," *IEEE Transactions on Circuits and Systems Part I: Regular Papers,* vol. 59, no. 10, pp. 2456–2467, Oct. 2012.

[5] Tomoharu Nagashima, Xiuqin Wei, Hisa-Aki Tanaka, and Hiroo Sekiya, "Locking range derivations for injection-locked class-E oscillator applying phase reduction the-

ory," *IEEE Transactions on Circuits and Systems Part I: Regular Papers,* vol. 61, no. 10, pp. 2904–2911, Oct. 2014.

[6] Tomoharu Nagashima, Xiuqin Wei, Tadashi Suetsugu, Marian K. Kazimierczuk, and Hiroo Sekiya, "Waveform equations, output power, and power conversion efficiency for class-E inverter outside nominal operation," *IEEE Transactions on Industrial Electronics,* vol. 61, no. 4, pp. 1799–1810, Apr. 2014.

[7] Xiuqin Wei, Tomoharu Nagashima, Marian K. Kazimierczuk, Hiroo Sekiya, and Tadashi Suetsugu, "Analysis and design of class-E_M power amplifier," *IEEE Transactions on Circuits and Systems Part I: Regular Papers,* vol. 61, no. 4, pp. 976–986, Apr. 2014.

[8] Hiroo Sekiya, Xiuqin Wei, Tomoharu Nagashima, and Marian K. Kazimierczuk, "Steady-state analysis and design of class-DE inverter at any duty ratio," *IEEE Transactions on Power Electronics,* (Accepted)

International Conferences

[1] Tomoharu Nagashima, Xiuqin Wei, Hiroo Sekiya, and Marian K. Kazimierczuk, “Power conversion efficiency of class-E power amplifier outside nominal operations,” *2011 IEEE International Symposium on Circuits and Systems (ISCAS2011),* pp. 749–752, May 2011.

[2] Xiuqin Wei, Tomoharu Nagashima, Shingo Kuroiwa, and Hiroo Sekiya, “Design of symmetrical class-E_M power amplifier” *The 37th Annual Conference of the IEEE Industrial Electronics Society (IECON’11),* pp. 1235–1240, Nov. 2011.

[3] Tomoharu Nagashima and Hiroo Sekiya, “Steady-state behavior of class-E amplifier outside nominal operation taking into account MOSFET-body-diode effect,” *2012 RISP International Workshop on Nonlinear Circuits, Communications, and Signal Processing (NCSP’12),* pp. 313–316, Mar. 2012.

[4] Xiuqin Wei, Tomoharu Nagashima, Tadashi Suetsugu, Shingo Kuroiwa, and Hiroo Sekiya, “Analytical expressions for class-E_M power amplifier,” *2012 RISP International Workshop on Nonlinear Circuits, Communications, and Signal Processing (NCSP’12),* pp.150–153, Mar. 2012.

[5] Taro Kakimoto, Tomoharu Nagashima, Xiuqin Wei, and Hiroo Sekiya, “Approximate analysis for class-E_M amplifier taking into account harmonic frequency components” *2012 RISP International Workshop on Nonlinear Circuits, Communications, and Signal Processing (NCSP’12),* pp.154-157, Mar. 2012.

[6] Tomoharu Nagashima, Xiuqin Wei, Tadashi Suetsugu, and Hiroo Sekiya, “Inductively coupled wireless power transfer with class-DE power amplifier,” *2012 IEEE Asia Pacific Conference on Circuits and Systems (APCCAS2012),* , pp. 73–76, Dec. 2012.

[7] Youhei Noguchi, Xiuqin Wei, Tomoharu Nagashima, Hiroo Sekiya, and Tadashi Suetsugu, “Negative-bias driving voltage for class-E GaN HEMT oscillator using a diode,” *2013 International Workshop on Nonlinear Circuits, Communications and Signal Processing (NCSP2013),* pp. 201–204, Mar. 2013.

[8] Tomoharu Nagashima, Xiuqin Wei, Hisa-Aki Tanaka, and Hiroo Sekiya, Numerical derivations of locking ranges for injection-locked class-E oscillator, *The 10th IEEE International Conference on Power Electronics and Drive Systems (PEDS2013),* pp. 1021–1024, Apr. 2013.

[9] Xiuqin Wei, Tomoharu Nagashima, Hiroo Sekiya, and Tadashi Suetsugu “Effect of MOSFET Parasitic Capacitances on EER Transmitter with Class-E Amplifier,” *2013 IEEE International Symposium on Circuits and Systems (ISCAS2013),* pp. 913–916, May 2013.

[10] Hiroo Sekiya, Xiuqin Wei, and Tomoharu Nagashima “High-frequency high-efficiency resonant converter with class-E_M inverter and class-E rectifier,” *IEEE 56th Intl Midwest Symposium on Circuits and Systems (MWSCAS2013),* pp. 33–36, Aug. 2013.

[11] Tomoharu Nagashima, Kazuhide Inoue, Xiuqin Wei, Elisenda Bou, Eduard Alarcon, and Hiroo Sekiya, “Inductively coupled wireless power transfer with class-E^2 DC-DC converter,” *The 21th European Conference of Circuits Technology and Devices(ECCTD2013),* Sept. 2013.

[12] Zhicai Zhang, Xiuqin Wei, Hiroo Sekiya, Naoki Oyama, Tadashi Suetsugu, and Tomoharu Nagashima, “Analysis of class E_M amplifier with considering non-zero current fall time of drain current,” *International Future Energy Electronics Conference 2013 (IFEEC2013),* pp. 338–343, Nov. 2013.

[13] Kazuhide Inoue, Tomoharu Nagashima, Xiuqin Wei, and Hiroo Sekiya, "Design of high-efficiency inductive-coupled wireless power transfer system with class-DE transmitter and class-E rectifier," *The 39th Annual Conference of the IEEE Industrial Electronics Society (IECON2013),* pp. 611–616, Nov. 2013.

[14] Hiroo Sekiya, Xiuqin Wei, and Tomoharu Nagashima, "MOSFET Parasitic Capacitance Effects to Class-DE Power Amplifier," *2013 IEEE Electrical Design of Advanced Packaging and System Symposium (EDAPS2013),* pp. 245–248, Dec. 2013.

[15] Elisenda Bou,Tomoharu Nagashima, Hiroo Sekiya, and Eduard Alarcon, "Class E^2 resonant non-radiative wireless power transfer link: a design-oriented joint circuit-system co-characterization approach," *2014 IEEE International Multi-Conference on Systems, Signals and Devices (SSD2014),* Feb. 2014.

[16] Tomoharu Nagashima, Kazuhide Inoue, Xiuqin Wei, Elisenda Bou, Eduard Alarcon, Marian K. Kazimierczuk, and Hiroo Sekiya, "Analytical design procedure for resonant inductively coupled wireless power transfer with class-E^2 DC-DC converter," *2014 IEEE International Symposium on Circuits and Systems (ISCAS2014),* pp. 113–116, June 2014.

[17] Tomoharu Nagashima, Xiuqin Wei, and Hiroo Sekiya, "Operation of class-E^2 DC-DC converter outside nominal conditions," *2014 International Symposium on Nonlinear Theory and its Applications (NOLTA2014),* pp. 478–481, Sept. 2014.

[18] Hiroo Sekiya, Kazuhide Inoue, Tomoharu Nagashima, Tadashi Suetsugu, Shotaro Kuga, Xiuqin Wei, Kenichi Shirota, Hironobu Hatamoto, and Satoru Shimizu, "A loosely coupled inductive wireless power transfer systems with class-E transmitter and multiple receivers," *2014 IEEE Energy Conversion Congress and Exposition (ECCE2014),* pp. 675–680, Sept. 2014.

[19] Tomoharu Nagashima, Xiuqin Wei, and Hiroo Sekiya, “Analytical design procedure for resonant inductively coupled wireless power transfer system with class-DE inverter and class-E rectifier,” *2014 IEEE Asia Pacific Conference on Circuits and Systems (APCCAS2014),* pp. 288–291, Nov. 2014.

[20] Yuta Yamada, Tomoharu Nagashima, Yoshifumi Ibuki, Yoshiki Fukumoto, and Hiroo Sekiya, “Numerical algorithm for distribution-map derivations of switching converters,” *The 40th Annual Conference of the IEEE Industrial Electronics Society (IECON2014),* pp. 4338–4344, Nov. 2014.

[21] Tomoharu Nagashima, Xiuqin Wei, Elisenda Bou, Eduard Alarcon, and Hiroo Sekiya, “Analytical design for resonant inductive coupling wireless power transfer system with class-E inverter and class-DE rectifier,” *2015 IEEE International Symposium on Circuits and Systems (ISCAS2015),* May 2015. (Accepted)

Technical Reports and Other Presentations

[1] Tomoharu Nagashima, Xiuqin Wei, and Hiroo Sekiya, "Power conversion efficiency of class-E power amplifier outside nominal operation," *IEICE Technical Report,* vol.111, no.106, pp.171–175, July 2011. (in Japanese)

[2] Xiuqin Wei, Tomoharu Nagashima, Shingo Kuroiwa, and Hiroo Sekiya, "Symmetrical class-E power amplifier for very low harmonic-content applications," *IEICE Technical Report,* vol. NLP2011-54, pp.165–170, July 2011. (in Japanese)

[3] Tomoharu Nagashima and Hiroo Sekiya, "Operation of class E amplifier outside nominal conditions," *24th Workshop on Circuit and Systems,* pp. 242–247, Aug. 2011. (in Japanese)

[4] Tomoharu Nagashima, Xiuqin Wei, Takuji Kousaka, and Hiroo Sekiya, "Analytical derivation of switching-pattern distribution for class-E amplifier using bifurcation theory," *IEICE Technical Report,* vol. NLP2011-100, pp.49–54, Nov. 2011.

[5] Tomoharu Nagashima, Xiuqin Wei, Takuji Kousaka, and Hiroo Sekiya, "Analytical derivation of power conversion efficiency for class-E amplifier with any Q," *IEICE Technical Report,* vol. NLP2012-23, pp.115–120, Apr. 2012.

[6] Tadashi Suetsugu, Xiuqin Wei, Kazunari Shimazaki, Tomoharu Nagashima, and Hiroo Sekiya, "Resonant class E rectifier for wireless power transfer in contactless IC card reader/writer," *2012 Korea-Japan Joint Technical Workshop on Semiconductor Power Converter,* pp. 58–61, Nov. 2012.

[7] Zhicai Zhang, Tomoharu Nagashima, Xiuqin Wei, and Hiroo Sekiya, "Analysis of class-E_M amplifier taking into acount drain current fall time," *IEICE Technical Committee on Nonlinear Problems,* vol. 112, no. 487, pp. 37–42, Mar. 2013. (in Japanese)

[8] Tadashi Suetsugu, Xiuqin Wei, Tomoharu Nagashima, and Hiroo Sekiya, "Parallel connected class D amplifiers for RF power source applications," *IEICE Technical Committee on Nonlinear Problems,* vol. 112, no. 487, pp. 33–36, Mar. 2013.

[9] Tomoharu Nagashima, Xiuqin Wei, Tadashi Suetsugu, and Hiroo Sekiya, "Design of class-E inverter with inductive impedance inverter for achieving zero voltage switching at any load resistance," *IEICE Technical Committee on Nonlinear Problems,* vol. 113, no. 69, pp. 71–75, May 2013. (in Japanese)

[10] Hiroo Sekiya, Xiuqin Wei, and Tomoharu Nagashima, "High-frequency high-efficiency resonant converter with class-E_M inverter and class-E rectifier," *The 26th Workshop On Circuits and Systems,* pp. 273–278, July 2013. (in Japanese)

[11] Xiuqin Wei, Tomoharu Nagashima, Hiroo Sekiya, and Tadashi Suetsugu, "Behaviors of EER transmitter with class-E amplifier due to MOSFET parasitic capacitances," *The 26th Workshop on Circuits and Systems,* pp. 380–384, July 2013.

[12] Kazuhide Inoue, Tomoharu Nagashima, Hiroo Sekiya, Hironobu Hatamoto, and Satoru Shimizu, "Design of wireless power transfer system through electromagnetic induction with class-DE transmitter and class-E rectifier," *IEEJ Technical Meeting on Semiconductor Power Converte,* July 2013. (in Japanese)

[13] Hiroo Sekiya, Tomoharu Nagashima, and Xiuqin Wei, "Resonant Converter with Class E_M Inverter," *IEICE Technical Committee on Nonlinear Problems,* vol. 113, pp. 35–40, Oct. 2013. (in Japanese)

[14] Tomoharu Nagashima, Xiuqin Wei, Tadashi Suetsugu, and Hiroo Sekiya, "Design of class-E inverter with inductive impedance inverter for achieving ZVS at any load resistance," *2013 Japan-Korea Joint Technical Workshop on Semiconductor Power Converter,* Oct. 2013.

[15] Tomoharu Nagashima, Kazuhide Inoue, Xiuqin Wei, and Hiroo Sekiya, "Analytical design for resonant inductively coupled wireless power transfer with class-E^2 DC-DC converter," *IEICE Technical Committee on Wireless Power Transmission,* pp. 23–27, Jan. 2014. (in Japanese)

[16] Xiuqin Wei, Tomoharu Nagashima, Hiroo Sekiya, and Tadashi Suetsugu, "MOSFET nonlinear capacitance effect on EER transmitter with class-E amplifier," *IEICE Technical Committee on Nonlinear Problems,* May 2014. (in Japanese)

[17] Tomoharu Nagashima, Xiuqin Wei, and Hiroo Sekiya, "Steady-state analysis of class-E^2 DC-DC converter outside nominal condition," *The 27th Workshop on Circuits and Systems,* pp.7-12, Aug. 2014. (in Japanese)

[18] Tomoharu Nagashima, Xiuqin Wei, and Hiroo Sekiya, "Analytical design of resonant inductively coupled wireless power transfer system with class-E^2 DC-DC converter," *The 1st Symposium on Semiconductor Power Conversion (S2PC),* Oct. 2014.

[19] Kazuhide Inoue, Tomoharu Nagashima, and Hiroo Sekiya, "A loosely coupled wireless power transfer system with class-DE transmitter and multiple receivers," *The 1st Symposium on Semiconductor Power Conversion (S2PC),* Oct. 2014.